BISMUTH-DOPED FIBRE AMPLIFIERS FOR MULTI-BAND OPTICAL NETWORKS

ALEKSANDR DONODIN

Doctor of Philosophy

ASTON UNIVERSITY

September 2022

Aston University

Bismuth-doped fibre amplifiers for multi-band optical networks

Aleksandr Donodin

Doctor of Philosophy, September 2022

Fibre-optic networks are the backbone of the global communications infrastructure that made possible modern Internet, providing a multitude of online services and a digital economy. The development of novel approaches for further increasing capacity of optical communication systems is in the focus of research around the world due to the constantly growing data traffic and the corresponding bandwidth demand. Arguably, the most practical technique is multi-band transmission which utilises a huge spectral bandwidth of the existing fibre base that has not previously been used. Unlike spatial division multiplexing, multi-band transmission does not require a new fibre deployment. However, it involves a significant upgrade of current networks with novel amplifiers in the O-, E-, S-, and U- optical bands that are yet to be developed and optimised.

In this thesis, E- and S-band bismuth-doped fibre amplifiers (BDFAs) are demonstrated. The following record characteristics of BDFAs are achieved: 40 dB gain, 4.5 dB noise figure, and 38% power conversion efficiency. In total, three BDFAs have been developed, characterised and optimised using pump laser diodes at different wavelengths. Two modelling techniques of BDFAs are proposed: one based on conventional rate equations, and another one based on a neural network "black box" approach. Both of these methods are analysed and their challenges are discussed. A big part of the thesis is devoted to data transmission demonstrations supported by developed BDFAs in E- and S-bands. The experiments include both IM/DD and coherent signal transmissions through various lengths of single mode fibre including record E-band transmission through 160 km of single mode fibre. In addition, a multi-band transmission experiment in E-, S-, C-, and L-band is performed with an in-line amplifier based on combined bismuth-doped fibre and discrete Raman amplification. The total signal bandwidth is 195 nm and the total number of transmitted channels is 143. The obtained results pave the way towards commercial implementation of multi-band transmission enabled by BDFAs in E- and S- optical communication bands.

Keywords: Optical communications, Bismuth-doped fibre, Bismuth-doped fibre amplifiers, Multi-band transmission, Ultra-wideband network,

To my parents - Ljudmila Donodina and Igor Donodin, whose unquenchable strive for a better life induced with creativity and open-mindedness inspire me every day.

Acknowledgements

First of all, I would like to thank my supervisor Prof Sergei K. Turitsyn for inviting me to join the amazing AiPT community and guiding me through thorny paths of my PhD. I have learned a lot from his wisdom, broad expertise and deep knowledge. I would specifically thank him for generating a lot of brilliant ideas and teaching me to be open to unusual combinations of techniques and concepts.

I would like to thank my associate supervisor Prof Wladek Forysiak for dedicating his time and effort to teaching me strategic thinking in conducting and presenting my research and sharing a lot of insights into how the academic and industrial worlds are turning. Moreover, I highly appreciate his continuous efforts to make me take appropriate breaks which, I hope, I will take more willingly in the future.

I would like to thank Dr Vladislav Dvoyrin for in-depth and colourful discussions of not only crucial details of bismuth-doped fibre amplifiers but also the history of Photonics. I have learnt a lot from his deep knowledge and meticulous approach.

I would like to thank Dr Egor Manuylovich for countless discussions, close collaborations and for teaching me so many elements of experimental and theoretical physics that are sometimes so easily evaded. It is a great pleasure to collaborate with him because of his broad experience and ability to take things on the chin. I want to thank him for our tea breaks and being a wonderful friend.

I would like to thank Dr Ian Phillips, Dr Mingming Tan, and Dr Paul Harper for teaching me the basics of conducting experiments on direct detection and coherent optical transmission. I have gained a lot of experience from these great experts.

I would like to thank Dr Valery Mashinsky and Dr Mikhail Melkumov for the provision of the bismuth-doped fibre. Without their kind help, this thesis would not be possible in the way it worked out.

I would like to thank Mr Pratim Hazarika for a lot of help with experimental work that we conducted together. It is a great joy for me to know that we will continue our journey at Aston University together as Research Associates.

I would like to thank Ms Tatiana Kilina for being the best project manager imaginable. My PhD journey would not have been the same without her constant support. I would

like to thank my colleagues Dr Morteza Kamalian Kopae, Mr Pedro J. Freire, Mr Vladislav Neskorniuk for numerous discussions and hints on machine learning, digital signal processing and general optical communications. I would like to thank my colleagues Dr Dmitrii Stoliarov and Dr Vladimir Gordienko for fruitful discussions on optical methods and nonlinear optics. I would like to thank them all for being excellent friends.

I would like to thank Dr Kirill Tokmakov and Ms Swaroopa Mucheli-Sudhakar for providing an exceptional technical support when it was needed the most.

I would like to address special thanks to European Commission for funding my work in the frames of the European Training Network "Wideband Optical Networks" and giving me an opportunity to live in the UK and travel to so many venues worldwide.

I would like to thank Dr Igor Kudelin for being the best flatmate and for his support during all stages of my PhD and life in the UK. Hopefully, our paths will cross again one day.

I would like to thank all other colleagues from Aston University, DTU, PoliTo, Orange Labs, and Infinera who I had great pleasure to collaborate with.

I would like to thank my friends all over the globe who were always beside me despite all the challenges.

I would like to thank my parents for always being supportive and believing in me. They taught me that the darkest hour is always before dawn.

I would like to thank Barkley for being brave and strong until the very end.

I would like to thank Holly for being a role model for my retirement.

Finally, I would like to thank Ms Daniela Schneevogt for being an amazing and loving partner. I value her constant support and patience during our journey together. I want to specifically thank her for proofreading my thesis and reminding me to include articles that are so often missing.

Table of contents

Nomenclature

Acronyms / Abbreviations

ADC	Analog to digital converter
ASE	Amplified spontaneous emission
BAC	Bismuth active centre
BDF	Bismuth-doped fibre
BDFA	Bismuth-doped fibre amplifier
BER	Bit error rate
Bi	Bismuth
DAC	Digital to analog converter
DCF	Dispersion compensating fibre
DP	Dual polarisation
DSF	Dispersion sifted fibre
DSP	Digital signal processing
EDFA	Erbium-doped fibre amplifier
Er	Erbium
EVM	Error vector magnitude
FEC	Forward error correction
FOPA	Fibre optic parametric amplifier

Ge	Germanium
IM/DD	Intensity modulated/direct detection
LD	Laser diode
LO	Local oscillator
MCF	Multi-core fibre
MF	Multi-fibre
MIMO	multiple input multiple output
MMF	Multi-mode fibre
Nd	Neodymium
OBPF	Optical bandpass filter
OSNR	Optical signal to noise ratio
PDF	Probability density function
Pr	Praseodymium
QAM	Auadrature amplitude modulation
QPSK	Quadrature phase shift keying
RF	Radio frequency
SDM	Space-division multiplexing
SMF	Single-mode fibre
SNR	Signal to noise ratio
SOA	Semiconductor optical amplifier
SRS	Stimulated Raman scattering
TEC	Thermoelectric cooler
TFF	Thin film filter
TL	Tuneable laser

Tm	Thulium
VOA	Variable optical attenuator
WDM	Wavelength-division multiplexed

List of figures

List of tables

Chapter 1

Introduction

1.1 Novel challenges of fibre-optic communications

While talking about the history of optical communications the scientific community usually divides it into different periods by commemorating significant technological advances that determined and dominated the way optical communications work in that specific stretch of time. Agrawal in his influential book "Fiber-optic communication systems" [1] splits the history of optical communications into five major generations. The first generation (1980-1985) utilised graded-index fibres in combination with radiation at 0.8 μm. The second generation (1985-1990) was based on the first single mode fibres and signal transmission in vicinity of 1.3 μm. The third generation (1990-1996) used almost identical fibres but the signal wavelength was shifted toward 1.5 μm where silica single-mode fibre (SMF) has the loss minimum. All three of these generations used repeaters, devices that converted the optical signal into electrical, amplified the electrical signal, and then converted it back to the optical domain. The main drawback of repeaters was that each carrier wavelength in the wavelength division multiplexing (WDM) system required its own repeater. Moreover, repeaters introduce significant delay to the transmitted signal due to the speed limitations of electrical components. However, the fourth generation (1996-present) made use of the first telecommunication optical amplifiers, erbium-doped fibre amplifiers (EDFAs), developed in the late 80s, early 90s by the group of Payne [2]. The development of EDFAs revolutionised optical communications by allowing simultaneous amplification of multiple single wavelengths around 1.55 μm in one all-optical device. Moreover, the fourth generation is remarkable by ubiquitous employment of coherent optical communication systems that allow higher data rates to be transmitted in comparison to intensity modulation/ direct detection (IM/DD) systems. The final, fifth generation (research since 2002) focuses on extending wavelength range over which a WDM system can operate. Currently, optical

Table 1.1 Optical communication bands defined by ITU-T

Band	O-band	E-band	S-band	C-band	L-band	U-band
λ_s, nm	1260-1360	1360-1460	1460-1530	1530-1565	1565-1625	1625-1675

communication systems are mostly using only conventional C-band. The wavelengths range for each of the optical communication bands are presented in Table 1.1. Recently, some commercial systems started to utilise L-band EDFAs for expanding the capacity of the optical networks.

In contrast, Winzer in paper [3] and Chraplyvy in paper [4] highlight four main eras of optical communications:

1. the era of regeneration (1977-1995),
2. the era of amplified dispersion-managed systems (1995-2008),
3. the era of amplified coherent systems (2008-present),
4. the era of space division multiplexing (research since 2008).

One can see that the first era consists of the three first generations highlighted by Agrawal, and era two and era three are the parts of the generation four of Agrawal. Both of these approaches of dividing the history of optical communications agree that optical networks will require significant upgrade of the systems very soon due to relentless traffic demand growth.

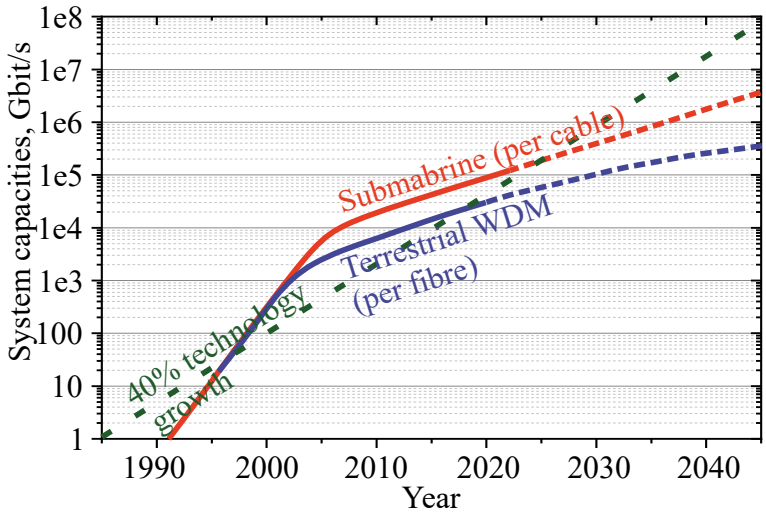

Fig. 1.1 Evolution of commercial optical telecommunication systems over the past 30 years and extrapolations for the next 20 years.

The evolution of commercial optical telecommunication systems over the last 30 years and extrapolated prediction of its growth in the next 20 years (from paper [3]) are presented in Figure 1.1. It shows a comparison between technology system rate capacities of submarine and terrestrial WDM systems. The interpolation with a 20% yearly increase (historic trend) will require more than 1 Pb/s per fibre for Submarine systems, and 200 Tb/s for terrestrial WDM systems by 2032 (10 years from now). Today, commercial long-haul C+L-band optical communication systems carry up to 192 channels at up to 250 Gb/s, supporting a total long-haul capacity of ∼48 Tb/s[5], and for short-reach applications up to 400 Gb/s for a total capacity of up to 76 Tb/s[6]. All these data rates became possible due to implementation of advanced modulation formats (higher than 16 QAM) [7]. Currently many works are being presented with impressive modulation formats like 1024 QAM transmission [8] or transmission of 4096 QAM through 200 km [9] or even transmission of 16384 QAM transmission over 25 km [10].

To explain capacity limitations of optical networks, the well-known Shannon limit can be introduced for optical communication systems [11]:

$$C = B \cdot 2 \cdot M \cdot log_2(1 + \frac{S}{N}) \tag{1.1}$$

where C is the total channel capacity limit, B is the signal bandwidth, S is the average power of signal, N is the noise spectral density, M is the number of channels, and 2 stands for two polarisation signals in dual-polarisation (DP) systems. The fraction under the logarithm is intrinsically signal-to-noise (SNR), thus to be able to detect a signal with higher channel capacity the higher SNR at the receiver should be achieved. In linear systems, the SNR degrades with the transmission in optical fibre, and additional noise is introduced by the receiver. However, if the signal power is significantly increased, the signal begins to propagate in a nonlinear regime, leading to an accumulation of noise related to nonlinear effects and thus, the signal power cannot be increased infinitely. Periodically-amplified optical communications systems are characterised by distributed nonlinear effects in the fibre. The most predominant nonlinear effect arises from the intensity dependent refractive index (Kerr effect) and results in a number of phenomena such as self-phase modulation, cross-phase modulation and four wave mixing [12]. The information capacity limits due to fibre nonlinearity were first addressed in 2001 [13] and are described by the Nonlinear Shannon limit [14]. The capacity limit of a nonlinear system depends not only on the SNR of the received signal, but also on nonlinearity of the fibre used for a transmission and its length. Thus, the Nonlinear Shannon limit for SMF can be graphically represented as a line in Figure 1.2 along with experimentally achieved spectral efficiencies (SEs). The figure is

obtained from [3]. It is clear from equation 1.1 that to transmit higher signal rate over longer distances more channels with the same SE are required.

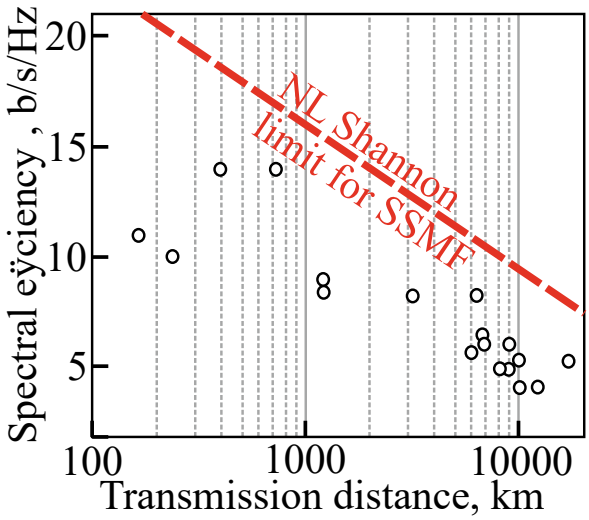

Fig. 1.2 Experimentally achieved record SEs (in two polarizations) for WDM experiments versus transmission distance (circles), shown with the Shannon limit estimate on standard SMF (SSMF) (dashed).

Thus, novel approaches of introducing more signal channels in the transmission lines should be proposed. Two main solutions are usually highlighted: multi band transmission (MBT) by Agrawal [1] and spatial division multiplexing (SDM) by Winzer and Chraplyvy [3, 4]. SDM technique is generally divided into two approaches: multi-fibre (MF) approach and multi-mode/core fibre (MMF/MCF) approach. Thus, SDM can be implemented through two main strategies: 1) by using dark fibres (only applied for MF approach [15]) or 2) by much more costly deployment of novel fibres [3, 16]. It was estimated that around $20,000 are required to lay one kilometre of fibre [3]. The SDM through MF approach is the most popular approach as there is still some dark fibre infrastructure that can be used for capacity increase. However, this approach will lead to high costs when the dark fibres infrastructure is exhausted. In contrast, the MMF/MCF approach leads to a potential capacity in 1 Pbit/s/fibre which is an important milestone, especially for submarine networks [17]. However, the required technology for commercial utilisation of SDM techniques is still not mature, and the costs related to the developing of the novel fibre infrastructure seems too high for a short-term or mid-term solution.

In contrast, the MBT technique is an attractive next-step solution that allows maximum return-on-investment from the existing infrastructure [18] by extending the transmission beyond widely utilised C-band. Commercial MBT systems are already targeting C+L-band with additional 60 nm bandwidth provided by L-band EDFAs. As the next step, other spectral

bands can be considered, for example S-band, and E-band. If the whole bandwidth from Table 1.1 is utilised for optical communication, it will allow to achieve more than a 10-fold increase in the data capacity in comparison to currently deployed C-band systems. However, MBT also requires development of novel in-line and transreceiver components for data transmission in unconventional bands, especially optical amplifiers.

There have been numerous demonstrations of various doped-fibre amplifiers [19, 20], Raman amplifiers [21], fibre optical parametric amplifiers [22], and semiconductor optical amplifiers [23] operating in different telecommunication bands from O- to U-bands. However, one of the most promising solutions for MBT are bismuth-doped fibre amplifiers (BDFAs), due to their significant spectral flexibility enabled by different co-dopants that can be used to fabricate fibres with different amplification bands. The optical network capacity can be increased by the matter of 10 comparing to C-band EDFA by only using BDF-based amplification systems. However, different types of Bi-doped fibres should be used to enable amplification in all telecommunication bands.

Thus, this thesis focuses on utilising BDFA systems for MBT networks, in particular development and use of germanosilicate-based BDFAs in E-band. E-band BDFAs have been studied and showed a great potential in terms of expanding the bandwidth of the conventional optical links due to decreased stimulated Raman scattering (SRS) impact on C-band and L-bands from the transmitted channels in E-band [24]. This allows to expand already deployed C+L-band telecommunication networks with minimal effort and impact on already deployed bands. A more detailed comparison of the solutions for MBT is presented in the next chapter along with recent advances in BDFAs.

1.2 Organisation of the thesis

This thesis is organised as follows.

Chapter 1. Introduction

The chapter presents the current challenges of optical communication networks and gives an overview of the possible solutions for coping with "capacity crunch". Special attention is paid to the current challenges of multi-band transmission.

Chapter 2. Optical amplifiers for optical communications

In this chapter, the diversity of optical amplifiers that are deployed or can potentially be deployed for amplification of a signal in telecommunication bands are presented. The chapter presents the main advantages and challenges of the amplifiers operating from the O-band to the U-band. The most recent state-of-the-art advances in the development and utilisation of the aforementioned amplifiers are highlighted.

Chapter 3. Bismuth-doped fibres

An overview of typical types of Bi-doped fibres is presented in this chapter. The methods of the fabrication of Bi-doped fibres are presented. The detailed overview includes the energy levels for each type of the fibre and corresponding luminescence spectra. The analysis of the recent advances in Bi-doped fibre amplifiers operating in a variety of telecommunication bands are presented. In the second part of the chapter, the numerical modelling of the E-band Bi-doped fibre amplifier is presented. The modelling methods include solving of the conventional energy level rate equations and a "black-box" machine learning approach. The main challenges of numerical modelling of Bi-doped systems are analysed.

Chapter 4. Development of Bi-doped fibre amplifiers

In this chapter, the development of three E-S-band Bi-doped fibre amplifiers is described. The main parameters of optical amplifiers are presented and the methods of their measurements are considered including manual and automatic methods. The developed amplifiers are compared with different pumping schemes. Further, the performance of the two amplifiers (BDFA-1 and BDFA-2) are compared with different pumping wavelengths combinations. The optimal amplifiers pump configurations are presented for minimisation of the NF and maximisation of the gain and the power conversion efficiency.

Chapter 5. Data transmission experiments enabled by BDFAs

In this section two types of data transmission in E-band are considered: intensity modulation/ direct detection and coherent transmission. Both transmissions are fully supported by only developed E-S-band bismuth-doped fibre amplifiers. The main specifics of the IM/DD and coherent transmission setups are considered along with the main metrics that are commonly used for these transmission formats. In addition to the pure E-S-band transmission, the multi-band transmission case of dual polarisation 30 GBaud 16 QAM channels in 195 nm bandwidth is considered. The experiment extends in E-S-C-L-bands where E-band is supported by the developed BDFAs, and the S-C-L-bands are supported by a discrete Raman amplifier.

Chapter 6. Discussion, future works and conclusion

This chapter concludes the thesis, provides an insight on the challenges with E-band Bi-doped fibre amplifiers and multi-band transmission, and proposes possible next steps for making E-band Bi-doped fibre amplifiers a stable and solid platform for the future optical bandwidth expansion.

1.3 Collaboration acknowledgement

The thesis focuses on the development and characterisation of BDFAs. Moreover, a big part of the work is devoted to realisation of E-band and wide-band data transmission enabled by BDFAs and other amplifiers. As BDFAs structure and data transmission experiments involve complex elements that were developed or involved effort of others I present a summary contributions in the table below:

Chapter	Activity	Collaborator
3	BDFA physical parameters optimisation using conventional rate equations	Dr Egor Manuylovich
3	NN modelling of the BDFA as a "black box"	Dr Uiara Celine De Moura, Dr Ann Margareth Rosa Brusin, Dr Francesco Da Ros, Prof Andrea Carena, and Prof Darko Zibar
4	Bismuth-doped fibre fabrication and provision	Dr Vladislav Dvoyrin, Dr Mikhail Melkumov, Dr Valery Machinsky
5	Direct detection setup development	Dr Ian Phillips, Dr Paul Harper
5	Coherent transmission setup development	Dr Ian Phillips, Dr Paul Harper, Dr Pavel Skvortcov
5	Digital signal processing for coherent signal	Dr Pavel Skvortcov, Dr Paul Harper
5	Development and characterisation of SCL-band discrete Raman amplifier	Mr Pratim Hazarika, Dr Mingming Tan

1.4 Contributions of the thesis

The contribution of this thesis targeting development and utilisation of E-band BDFAs for MBT can be summarised as follows:

Chapter 2

- The author provides an extensive review of the main amplifiers that can be used for optical communication networks including the ones that can be used for MBT: Raman amplifiers, SOAs, FOPAs, EDFAs, PDFAs, NDFAs, TDFAs, and BDFAs.
- Main methods of modelling of the doped fibre amplifiers are provided along with the main fibre characteristics and energy level diagrams.

Chapter 3

- The thesis describes the method of fabrication of BDFs and the main types of BDFS: aluminosilicate fibres, phosphosilicate fibres, low-germanosilicate fibres and high-germanosilicate fibres along with the methods of modeling of the BDFs. Energy level diagrams for BDFs are provided and the main challenges of the modelling of BDFs are discussed.

- Main parameters of the active doped-fibre are presented. Two methods of modelling of BDFs are proposed for E-band BDFA based on low-germanosilicate fibre. The E-band BDFA is modelled using conventional method and neural-network model. Challenges with both models are discussed and future improvements of BDF modelling are proposed.

Chapter 4

- The thesis provides a description of the main parameters of optical amplifiers along with the methodology for their manual and automated measurements. The setup of automatic measurement of gain, NF and PCE was developed at Aston University that can be used for characterisation of any optical amplifiers operation in E-, S-, C-, and L-bands.

- Three optical amplifiers operating in E- and S- bands with record performance for E-band amplifiers were developed. The best performance is achieved with the BDFA-2 which features record 39.8 dB gain, 4.5 NF for -25 dBm input signal power and 38% PCE for 5 dBm input signal power.

- Different pumping schemes were compared including various combination of pumping wavelengths. Based on the achieved experimental results, a conclusion about the pump wavelength optimisation of BDFAs is made.

Chapter 5

- The thesis provides the description of the main quality metrics for both IM/DD and coherent signals. The setup descriptions of both IM/DD and coherent systems are provided along with the procedure for their setting up.

- The developed BDFAs were used to demonstrate 4 channel IM/DD transmission through 160 km of 10 GBit/s OOK NRZ signal which is the record transmission distance for IM/DD system in E-band.

- An in-depth study of the coherent transmission systems enabled by developed BDFAs was performed. It included a 60 km long transmission of 50 GBaud SP QPSK supported by 2 BDFAs and a 4 channel E-band 30 GBaud 16 QAM transmission over 160 km supported by 3 BDFAs. The transmission quality was characterised and the performance degradation factors were appropriately discussed.

- The thesis demonstrates the record bandwidth transmission of the coherent signal in E-S,C-L bands which was supported by developed BDFAs and DRA discussed in details in the PhD thesis of Dr Pratim Hazarika. The signal consists of DP 143 30 Gbaud 16 QAM channels and is transmitted through 70 km of SMF.

Chapter 6

- The author briefly discusses future research directions in the area of MBT and BDFAs.

Publications

The following publications are the results of the presented research and directly or indirectly relate to different chapters of this thesis:

- **Aleksandr Donodin**, Vladislav Dvoyrin, Egor Manuylovich, Lukasz Krzczanowicz, Wladek Forysiak, Mikhail Melkumov, Valery Mashinsky, and Sergei Turitsyn. "Bismuth doped fibre amplifier operating in E-and S-optical bands." Optical Materials Express 11, no. 1 (2021): 127-135.

- **Aleksandr Donodin** , Mingming Tan, Pratim Hazarika, Vladislav Dvoyrin, Ian Phillips, Paul Harper, Sergei Turitsyn, and Wladek Forysiak. "30 GBaud DP 16-QAM Transmission in E-band Enabled by Bismuth-doped Fiber Amplifiers." Optics Letters 47, no. 19 (2022): 5152-5155.

- **Aleksandr Donodin**, Uiara Celine de Moura, Ann Margareth Rosa Brusin, Egor Manuylovich, Vladislav Dvoyrin1, Francesco Da Ros, Andrea Carena, Wladek Forysiak, Darko Zibar, Sergei K. Turitsyn "Neural network modeling of bismuth-doped fiber amplifier", Journal of the European Optical Society-Rapid Publications 19, no. 1 (2023): 4.

- Pratim Hazarika, Mingming Tan, **Aleksandr Donodin**, Mohammad Patel, Ian Phillips, Paul Harper, Wladek Forysiak "Ultra-wideband discrete Raman amplifier optimisation for single-span S-C-L-band coherent transmission systems" Optics Letters 47, no. 24 (2022): 6472-6475.

- Pratim Hazarika, Mingming Tan, **Aleksandr Donodin**, Shabnam Noor, Ian Phillips, Paul Harper, Jeffery S. Stone, Ming Jun Li, Wladek Forysiak "E-, S-, C- and L- band coherent transmission with multistage discrete Raman amplifier" Optics Express 30, no. 24 (2022): 43118-43126.

- Egor Manuylovich, **Aleksandr Donodin**, and Sergei Turitsyn. "Intensity-only-measurement mode decomposition in few-mode fibers." Optics Express 29, no. 22 (2021): 36769-36783.

- Dmitrii Vlasov , Gleb Konovalov, Igor Andreev, Yury Yakovlev, Vasilii Voropaev, **Aleksandr Donodin**, Mikhail Tarabrin, Daniil Batov, Ekaterina Kunitsyna, and Vladimir Lazarev. "Speed characterization of pin photodiode based on GaSb/GaInAsSb/GaAlAsSb heterostructure with frontal bridge contact at 1.9 μm." Applied Optics 60, no. 8 (2021): 2263-2268.

- **Aleksandr Donodin**, Vladislav Dvoyrin, Egor Manuylovich, Mikhail Melkumov, Valery Mashinsky, and Sergei Turitsyn, "38 dB Gain E-band Bismuth-doped Fiber Amplifier " 2022 European Conference on Optical Communication (ECOC), Tu5.5, 2022, pp. 1-4.

- **Aleksandr Donodin**, Pratim Hazarika, Mingming Tan, Vladislav Dvoyrin, Mohammed Patel,Ian Phillips, Paul Harper, Sergei Turitsyn, Wladek Forysiak, "195-nm Multi-Band Amplifier Enabled by Bismuth-doped Fiber and Discrete Raman Amplification", 2022 European Conference on Optical Communication (ECOC),Th2A.1, 2022, pp. 1-4.

- **Aleksandr Donodin**, Vladislav Dvoyrin, Egor Manuylovich, Ian Phillips, Wladek Forysiak, Mikhail Melkumov, Valery Mashinsky, and Sergei Turitsyn. "4-channel E-band data transmission over 160 km of SMF-28 using a bismuth-doped fibre amplifier." In Optical Fiber Communication Conference, pp. Tu1E-3. Optica Publishing Group, 2021.

- **Aleksandr Donodin** , Mingming Tan, Ian Phillips, Abdallah AI Ali, Pratim Hazarika, Mohammed Patel, Paul Harper, Vladislav Dvoyrin, Wladek Forysiak, and Sergei Turitsyn. "50 Gbaud QPSK E-band Transmission Using Bismuth Doped Fiber Amplifiers." In Optical Fiber Communication Conference, pp. W3J-5. Optica Publishing Group, 2022.

- Pratim Hazarika, Mingming Tan, **Aleksandr Donodin**, Ian Phillips, Paul Harper, Ming-Jun Li, and Wladek Forysiak. "210 nm E, S, C and L Band Multistage Discrete

Raman Amplifier." In Optical Fiber Communication Conference, pp. Tu3E-2. Optica Publishing Group, 2022.

- Bruno Correia, **Aleksandr Donodin**, Rasoul Sadeghi, Vladislav Dvoyrin, Antonio Napoli, Joao Pedro, Nelson Costa, Wladek Forysiak, Sergei K. Turitsyn, and Vittorio Curri. "QoT Evaluation of Optical Line System Transmission with Bismuth-Doped Fiber Amplifiers in the E-Band." In Asia Communications and Photonics Conference, pp. M4I-5. Optica Publishing Group, 2021.

Chapter 2

Optical amplifiers for optical communications

In this chapter, an overview of the optical amplifiers operating in ITU-T telecommunication bands is presented.

2.1 Raman amplifiers

Raman amplifiers are based on the effect of stimulated Raman scattering (SRS) occurring in optical fibres [12]. They are so far the most studied type of the amplifiers along with EDFAs. To discuss the disadvantages and benefits of Raman amplifiers, it is important to introduce the physical principles that it makes use of. SRS is an important nonlinear process, that can not only allow a useful Raman amplification from pumps to signal, but also lead to undesirable transfer of energy from low wavelength channels to higher wavelength channels.

In any molecular medium, spontaneous Raman scattering can transfer a fraction of power from one optical field to a new one, whose frequency is less by an amount determined by the vibrational modes of the medium. This effect was discovered by Raman in 1928 [25] and later in 1962 the effect of SRS was observed [26]. The main difference between spontaneous Raman scattering and SRS is that SRS enables more efficient transfer of the pump (higher frequency) to the signals (lower frequency). The effectiveness of the energy transfer of SRS and its spectrum depends on the media where signal and pump are being transmitted. A comparison between Raman gain efficiency for three typical fibres used in optical communication is presented in Figure 2.1[1, 27].

One can see that the maximum gain of each fibre is shifted approximately by 12 THz from the pump wavelength. That means, that, for instance, to achieve amplification in

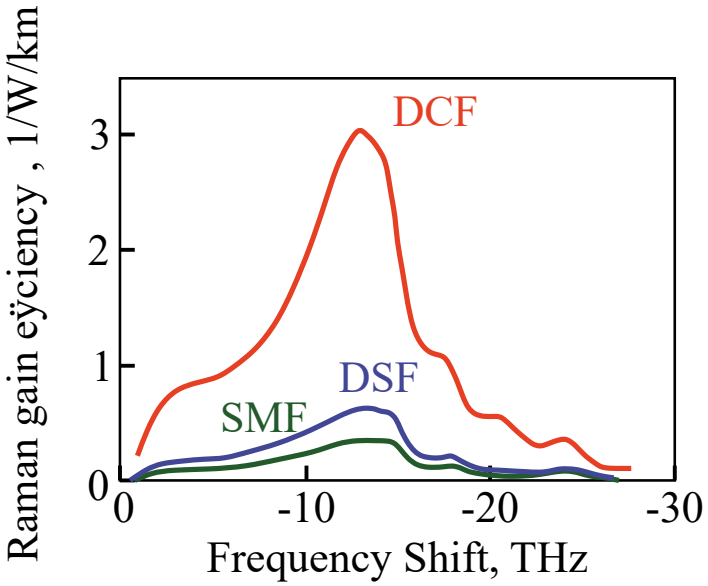

Fig. 2.1 Raman gain spectra for SMF, DSF, and DCF pumped at 1510 nm.

C-band one requires to use pump laser diodes (LDs) with radiation wavelengths in S-band. The significant difference of the amplitude of gain for all three presented fibres is mostly explained by geometrical and composition difference of the fibres. The Raman gain depends on nonlinear coefficient comprising from both nonlinear refractive index and effective mode area [12]. Both dispersion shifted fibre (DSF) and dispersion compensating fibre (DCF) have lower core diameter and different concentration of Ge. Thus, this leads to the differences to nonlinear coefficient of the fibre. Based on the fibre and its length that is used in the Raman amplifier, the Raman amplifier design can either be discrete or distributed [28]. Distributed Raman amplifiers are commonly based on SMF and, basically, use the transmission fibre as the amplification medium [29]. In contrast, discrete Raman amplifiers use 5-20 km-long segments of fibre that is used as amplification medium [30]. Currently, a significant progress has been made to use multiple Raman pumps for developing not only wideband Raman amplifiers [31], but also Raman amplifiers with flat or tilted gain spectra (to compensate tilt of SMF loss) using conventional and machine learning (ML) techniques [31–33].

The main advantage of Raman amplifiers is that they can be designed to amplify any necessary optical band if the required pump lasers are available. Moreover, ultra-wideband designs (more than 200 nm gain bandwidth) of amplifiers purely based on SRS have been recently presented [31]. Distributed Raman amplifiers usually can provide low NF (around 5 dB), and sufficiently compensate the loss of the transmission fibre. However, they require a high level pump powers and numerous pump LDs to achieve flattop and high gain. In contrast, discrete Raman amplifiers can achieve a higher gain coefficient of up to 27 dB [32],

but still suffer from relatively high NF (more than 6 dB). One of the main disadvantages of the Raman amplifiers, both discrete and distributed, is the requirement of numerous pump LDs at different wavelengths that are DFB stabilised and in total have high optical power. This often leads to low power conversion efficiency (PCE) of Raman amplifiers.

2.2 Semiconductor optical amplifiers

Semiconductor optical amplifiers (SOA) are based on the stimulated emission on the electron transition from a conduction band to a valence band of a semiconductor [34]. However, to achieve gain, the emission should exceed the material loss and excess loss caused by stimulated absorption. Sufficient population of the conduction band can be achieved directly by electrical current injection. Confinement of the optical wave in the active zone of SOA is achieved by surrounding the gain medium in a cladding material with lower refractive index, thus, forming an optical waveguide.

SOAs can be designed to cover any desired wavelength range and bandwidth up to 100 nm. They are usually quite compact and can be pigtailed which increases their compatibility with telecommunication standards [23]. However, there are multiple drawbacks that limit the applicability of SOAs. The typical output powers of SOAs are below 20 dBm, and the NF exceed 7 dB. Moreover, amplification in a single chip is polarisation-sensitive, thus, to achieve low polarisation dependent gain, a combination of two chips should be used which increases cost and complexity of the amplifier. Furthermore, the usable output power range of conventional SOAs is strongly limited due to gain saturation generating interchannel crosstalk [35]. Despite recent progress, SOAs are still not widely used for WDM applications due to high NF and smaller output powers compared to doped-fibre amplifiers.

2.3 Fibre optical parametric amplifiers

Fibre optical parametric amplifiers (FOPAs) are based on the third-order Kerr nonlinearity of optical fibres. Parametric amplification in fibres can be achieved in two or single pumping schemes. If one considers one of the pumps' optical frequency to be ω_{p1} and the optical frequency of the second one to be ω_{p2}, and if a signal at ω_s co-propagates with pumps, then it generates a new wave at ω_i which grows while propagating with signal and pumps. The spectrum of idler is a mirror image of that of the signal in respect to the central frequency that can be defined as $\omega_c = (\omega_{p1} + \omega_{p2})/2$. When only a single pump exists, centre frequency equals pump frequency. The spectrum of idler is inverted and is complex-conjugated to the signal and is shown in Figure 2.2 [36]. Generally FOPA operates in a regime when both

signal and idler are present at the input to the amplifier. For a more detailed explanation of the FOPA operation refer to [12, 36].

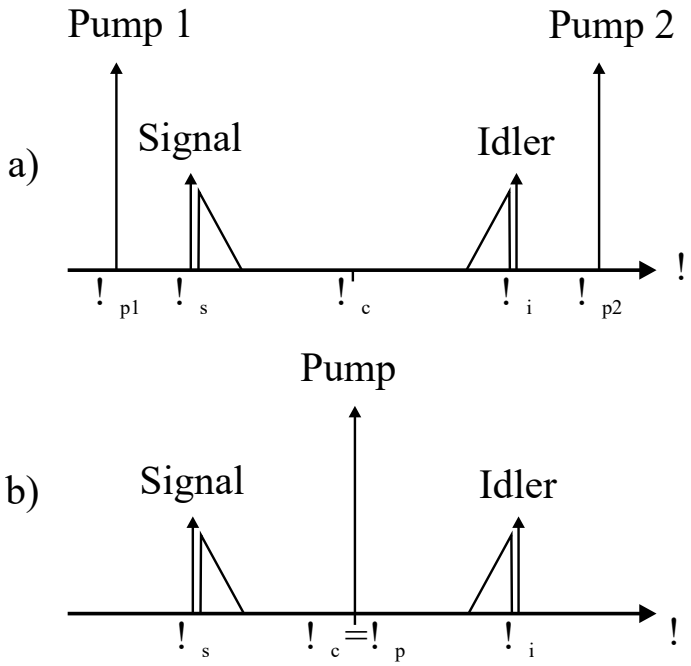

Fig. 2.2 Output spectra of FOPA for two pumps (a) and one pump (b).

Generally, several advantages of FOPAs are highlighted in the literature: potential large gain of 70 dB [37], a broad gain spectrum (more than 100 nm) [38], and phase sensitive gain that allows to potentially achieve NF less than 3 dB [39]. Moreover, as the FOPA is based on Kerr nonlinearity, the design can be used at any desired amplification bandwidth with suitable passive components and LDs provided [40]. Previously, one of the main drawbacks of FOPA was its polarisation sensitivity, however, utilisation of different designs like looped polarisation insensitive FOPA allowed to minimise polarisation sensitivity of FOPA [41].

However, one of the main drawbacks of FOPAs is a requirement to deal with high pump powers (higher than 1 W) that can sometimes exceed even 10 W. Despite its possibility to achieve high gain, low NF and wide bandwidth, FOPAs usually suffer from low PCE of several % or less [42]. Another significant drawback is the complexity of the setup that requires polarisation beam splitter (PBS), circulators and multiple WDMs to allow polarisation insensitive amplification. Moreover, when developing such an amplifier for unconventional bands, each of the components should be specifically designed to be compatible with the required transmission band. In comparison, typical doped-fibre amplifiers are based only on two WDMs if bi-directional pumping is required and a set of isolators, that are usually available for wide spectral bands.

2.4 Doped-fibre amplifiers

As the next step, the diversity of doped-fibre amplifiers operating in telecommunication bands is considered. The comparison of the main parameters of doped-fibre amplifiers is presented. The energy levels of all doped-fibre amplifiers are shown in this Section except Bi-doped fibres (BDFs). Because of the rich diversity of BDFs, they are discussed in the next Chapter 3 with utmost detail. The main distinctive feature of all doped-fibre amplifiers is that they are only developed as discrete amplifiers with much shorter length than the transmission line.

2.4.1 Er-doped fibre amplifiers

Among all rare-earth doped elements, erbium is the most widely used element that is used in the majority of optical amplifiers around the world. It operates in the vicinity of 1.54 μm. The EDFAs have been extensively studied since the late 1980s, however, a significant advance has been made in early 1990s that allowed a wide commercial use of EDFAs. This significant change (before EDFAs, repeaters were used for compensation of optical loss in transmission fibres) allowed to massively implement WDM systems and, thus, substantially increase the capacity of optical networks. For the last 30 years EDFAs have proved themselves as a reliable tool for amplification in C-band. The energy level diagram for erbium is presented in Figure [43, 44]. According to the energy diagram, EDFA can be pumped at both 980 nm ($^4I_{15} - ^4I_{11}$) and at 1480 ($^4I_{15} - ^4I_{13}$) to achieve generation in vicinity of 1540 nm.

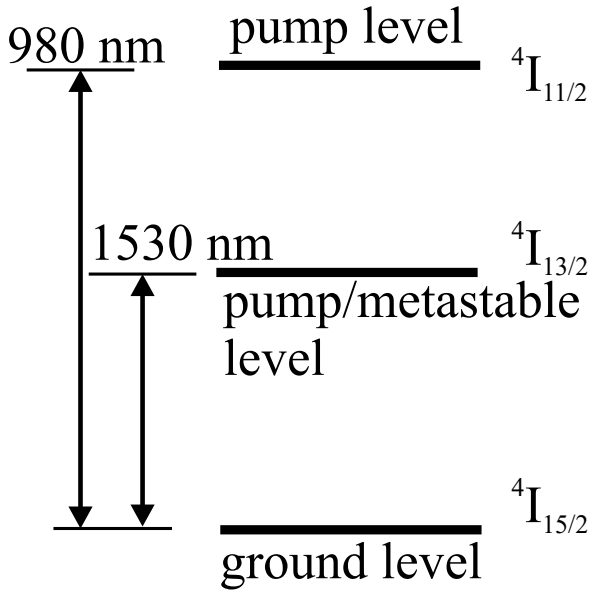

Fig. 2.3 Energy level diagram of erbium.

The EDFA has been substantially studied in terms of modelling using conventional rate equations in [43, 45]. The amplifier operating at a pump wavelength of 980 nm can be modelled using the three level system (Described in Appendix A) and the amplifier with a pump wavelength of 1480 can be described using the quasi-three level system, which can be simplified to the two level system (Appendix B). The absorption and emission cross sections of a C-band EDFA are presented in Figure 2.4 [46]. One can see that the absorption and emission cross sections significantly overlap. However, if the EDFA is pumped at 1480 the transition is happening at the tail of the transition, as the maximum of the absorption cross section is near 1530 nm. The emission cross section has a similar shape as the absorption cross section. It has a well pronounced peak in vicinity of 1530 nm and sometimes gain flattening filters are used to allow flatter amplification in C-band EDFAs. Current state of the art of C-band EDFAs allow to achieve gain as high as 40 dB, PCE of 33% for 980 nm pump and PCE of 50% for 1480 nm pump wavelength [47]. Commercially available EDFAs are close to the theoretical limit of 3 dB for NF and achieve NF as low as 3.5 dB.

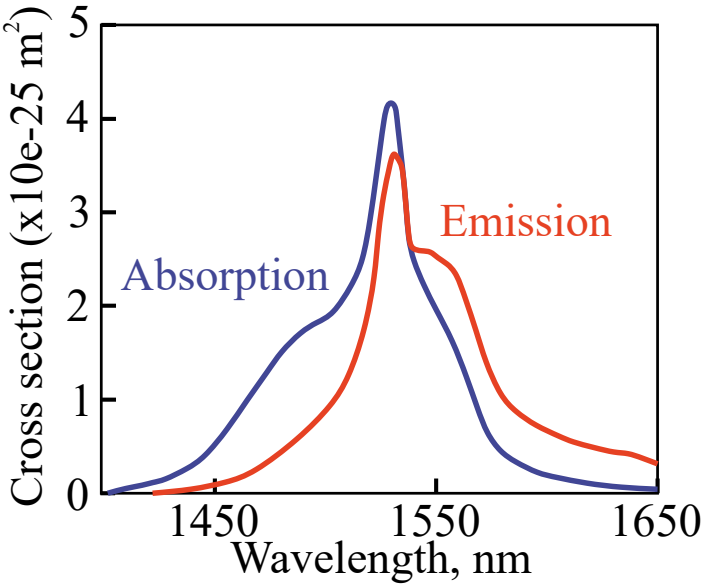

Fig. 2.4 Emission and absorption cross sections of Erbium.

In addition to C-band amplification, EDFAs can also be designed to provide gain in L-band. They are based on the same transition as C-band amplifiers and use the right-hand side tail of the emission cross section. However, L-band amplifiers most commonly use only 1480 nm pumps to support a better transition of the energy towards L-band. The PCE of L-band amplifiers is typically around 20% [48]. However, recent studies proposed to use 980 nm pump for L-band EDFAs based on phosposilicate erbium-doped fibre [49]. They

also provide gain higher than 35 dB, however, their 5-6 dB NF is higher compared to C-band EDFAs.

2.4.2 Pr-doped fibre amplifiers

Praseodymium fibres were extensively studied in the 1990s [50]. However, due to various factors they were not found as reliable as Er-doped fibres [35]. These factors are addressed in the next paragraph. Praseodymium-doped fibre amplifiers (PDFAs) can potentially provide gain in O-band, more specifically in the spectral range from 1280 nm to 1330 nm. However, one of the main drawbacks of PDFAs is that Pr-doped fibre can only be realised based on fluoride or chalcogenide fibre that have low compatibility with SMF-fibre. The energy diagram of the levels corresponding to the operation of Pr in vicinity of 1300 nm is shown in Figure 2.5 [51].

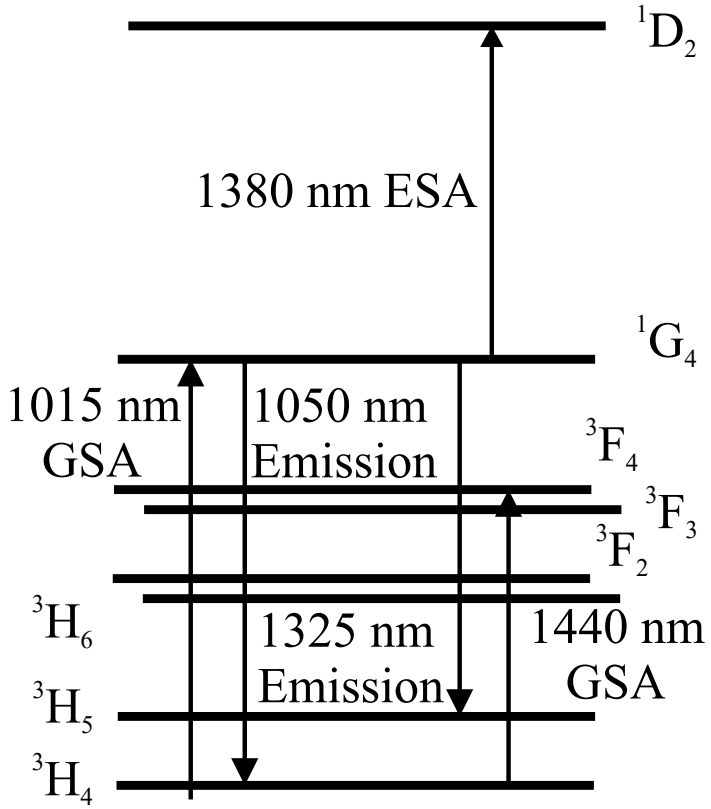

Fig. 2.5 Energy level diagram of praseodymium.

The transition $^3H_4 - ^1G_4$ can be used as a pump transition at 1015 nm. The radiation transition exists between energy levels $^1G_4$ and $^3H_5$. However, a rapid non-radiative transition between G_4 and $^3F_4$ levels (small non-radiative lifetime) contributes to the poorer (as

compared to EDFAs) performance of the Pr-doped fluoride fibre amplifiers [51] and prevents creation of Pr-doped silica fibre amplifiers that would be fully compatible with standard telecommunication fibres. Another problem with praseodymium is excited state absorption that can lead to undesirable transfer of some of the already excited electrons from $^1G_4$ to higher level $^1D_2$. PDFA can be modelled using 4 level system described in Appendix C.1. However, it should in addition consider excited state absorption, and ground state absorption described in [51]. These two effects significantly contribute to the population of the upper emission transition level along with its non-radiative lifetime. As the cross section of pump absorption is by a factor of ten smaller than the cross section of single emission, the fraction of the pump power absorbed during propagation in the doped fibre is small. Due to the low PCE, high power LD have to be used for pumping, which leads to short LD lifetimes. This is one reason why PDFAs are known for high failure rates [35]. The PDFA can achieve 25 dB gain, and 7 dB NF [52], mostly due to usually high loss between silica fibre components and fluoride active fibre and existence of undesirable transitions in the active fibre. Currently, very limited work is being conducted on the development of PDFAs.

2.4.3 Nd-doped fibre amplifiers

The neodymium-doped fibre has been proposed as a possible solution for amplification in E-band in the same time frame as Pr-doped fibre [53]. Neodymium-doped fibre amplifier (NDFA) can provide gain in both O- and E-bands in the spectral range from 1310 nm to 1370 nm [53] for the O-band, and in the E-band operation wavelength range is 1400-1450 nm [19]. For discussion of several current challenges with NDFAs the energy level diagram of neodymium is presented in Figure 2.6.

Pump transition between the ground level $^4I_{9/2}$ and the upper level $^4F_{5/2}$ can interact with the pump wavelength in vicinity of 800 nm. One can see that fast transition between $^4F_{5/2}$ and $^4F_{3/2}$ allows to achieve the population inversion between $^4F_{3/2}$ and lower levels. The stimulated emission and amplified spontaneous emission (ASE) can occur on all transitions from $^4F_{3/2}$ and lower levels like $^4I_{9/2}$, $^4I_{11/2}$, $^4I_{13/2}$. Commonly, the following transition can compete with each other: $^4F_{3/2} - ^4I_{9/2}$, $^4F_{3/2} - ^4I_{11/2}$, and $^4F_{3/2} - ^4I_{13/2}$ [19, 53, 54]. The broad $^4F_{3/2} - ^4I_{13/2}$ transition supports amplification in O-band and E-band. The magnitude of the optical gain observed in the E- and O- bands in the result of the $^4F_{3/2} - ^4I_{13/2}$ transition is substantially limited by the ASE originating from other transitions. However, to achieve sufficient amplification on the single transition, ASE on the other competitive transitions should be minimised. To allow higher efficiency of E-band amplification achieved with NDFA, the Nd-doped micro-structured fibre was proposed. Such fibre is designed specifically to attenuate unwanted ASE on transition $^4F_{3/2} - ^4I_{11/2}$ [19]. Even though a

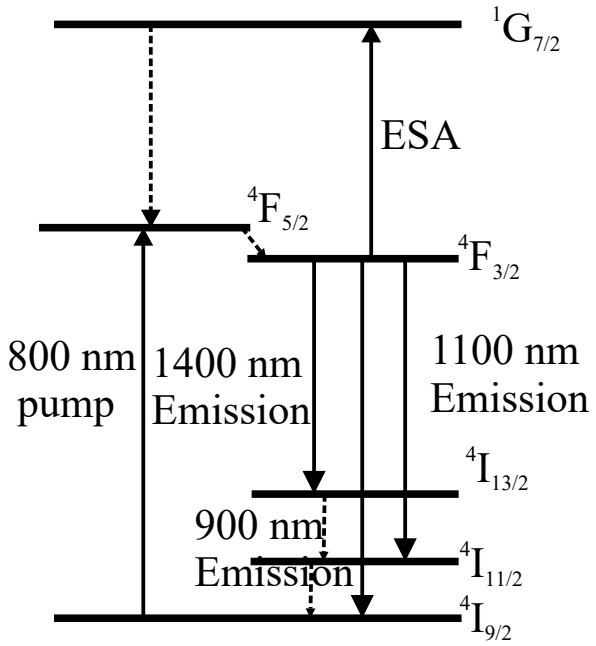

Fig. 2.6 Energy level diagram of neodymium.

significant progress has been made recently, such fibres still require further development in order to match the performance of Er-doped fibres. NDFAs now can achieve 24 dB gain and 6-7 dB NF with up to 18% PCE [19]. The modelling of NDFAs is described in details in [54] and can be generally described using a four-level system described in details in Appendix C. The modelling of NDFA should include most of stimulation emissions from $^4F_{3/2}$ as well as exited state absorption from level $^4F_{3/2}$ to the level $^4G_{7/2}$.

2.4.4 Tm-doped fibre amplifiers

The thulium-doped fibre allows broad amplification bands in S-band and at longer wavelength in vicinity of 1850 nm. A comprehensive numerical model of a thulium-doped silica-based fibre amplifier was presented in paper [55]. The energy diagram of thulium is presented in Figure 2.7. The laser transition that is associated with the signal amplification in vicinity of 1500 nm is $^3H_4 - ^3F_4$. As this transition exists between sub-level of the upper level and the second level, the signal amplification at 1500 nm in Tm-doped fibre can be characterised by 4-level energy system.

Two main problems complicate the use of this transition for an efficient optical amplification. Firstly, the thulium behaves as a four-level laser system where the lifetime of the lower level is longer than that of the higher level. Therefore, the population inversion can be hardly achieved with direct pumping to the upper laser level. The second problem with the

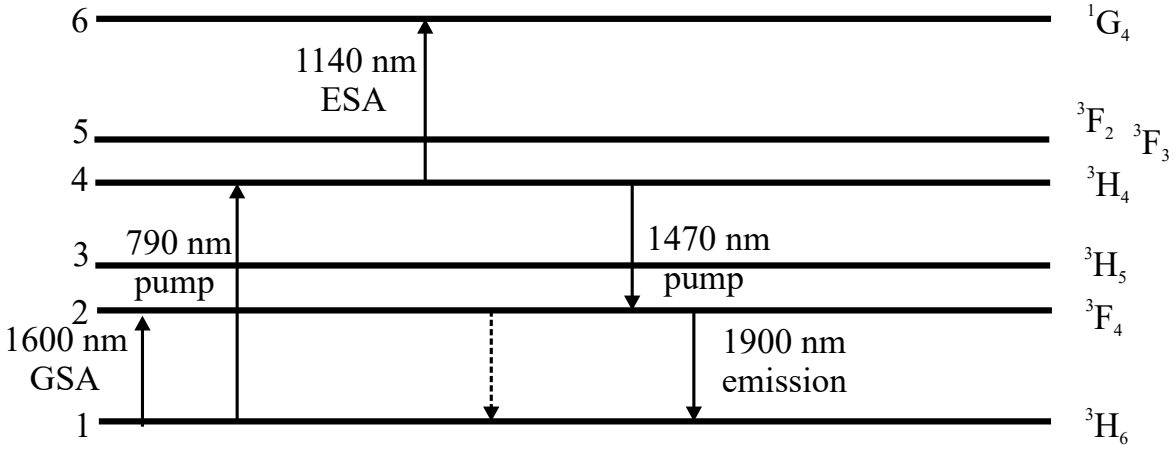

Fig. 2.7 Energy level diagram of thulium.

$^3H_4 - ^3F_4$ transition is the possibility of nonradiative decay via the intermediate level $^3H_5$. While modelling Tm-doped fibres, it is important to carefully consider up-conversions and cross-relaxations which can occur between various energy levels. Those effects are described in detail in the paper [55].

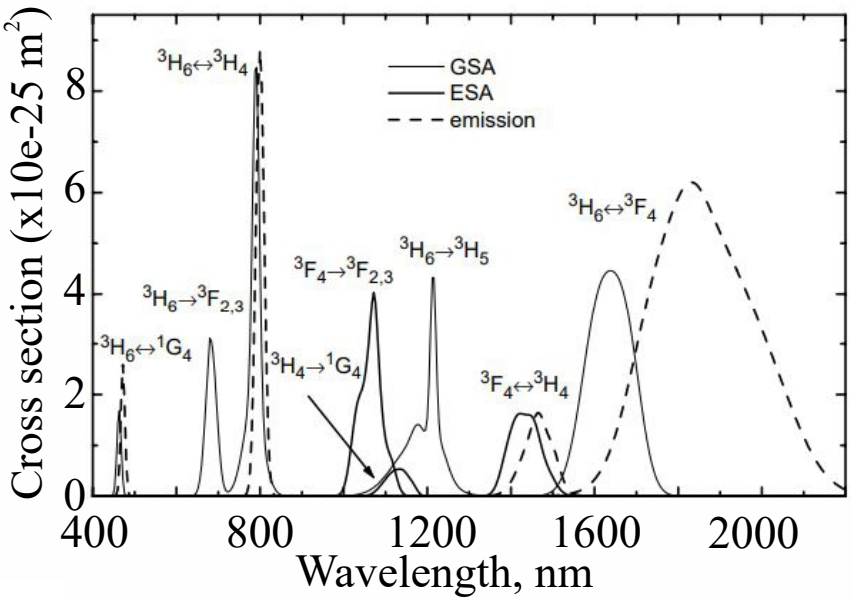

Fig. 2.8 Emission and absorption cross sections of Tm-doped fibre.

If these effects are considered, this problem can be resolved with up-conversion pumping schemes involving pump absorption from the ground level and from the second energy level using one or two pump wavelengths. Combining such a pumping scheme with suppressed

pump excited state absorption, thulium behaves like a three–level amplifier and PCEs of 50% can be achieved [56, 57]. Since such pumping schemes are less efficient in glass hosts exhibiting higher phonon energy, the use of low phonon energy glasses is beneficial. However, signal amplification can be obtained in multi–oxide silicate glass, although with reduced gain efficiency as compared to fluoride glass [35]. Figure 2.8 shows emission and absorption cross sections of Tm-doped fibre.

With respect to spectral hole burning, thulium performs better than erbium, since TDFAs exhibit hole depths that are by a factor of four smaller than those of C–band EDFAs [58]. Depending on the host material [59], TDFAs offer gain bandwidths between 30 nm and 60 nm with varying centre wavelength for amplification in WDM systems. Typical TDFAs are designed either for the bandwidth–limited S–band (1480 nm–1530 nm) or the S+–band (1450 nm–1480 nm). Thus, only the combination of two TDFAs is able to open up the complete S–band for data communication [35].

2.4.5 Bi-doped fibre amplifiers

The first Bi-doped fibre and a laser based on that fibre were developed and demonstrated in 2005 by the group of Dianov [60]. The laser generated optical radiation in the spectral range of 1120-1220 nm. Since 2005, BDFAs have been extensively but not yet completely studied and showed a great potential for ultra-wideband optical communication networks. Bi-doped fibre is a unique material with broad emission and amplification bands covering in total an impressive bandwidth of 1.1-1.8 μm that are presented in Figure 2.9. Such spectral flexibility of BDF is achieved by co-doping of the core of the BDF with different additional elements. Amplification with BDFA can be achieved in all telecommunication bands: aluminosilicate fibres allow to achieve amplification in vicinity of 1100 nm [61], O-band can be covered by phosposilicate fibres [62] (1200-1300 nm), E- and S-bands can be amplified with germanosilicate fibres with low concentration of germanium (Si-Bi-related centre allows to achieve generation between 1390-1510nm) [63], and amplification in L-band and U-band is observed in germanosilicate fibres with high germanium concentration (Ge-Bi-related centre allows to amplify the region of 1600-1800 nm) [64].

Recent advances in development of BDFAs have shown a significant progress in development and utilisation of BDFAs in all aforementioned regions, but the most attention has been paid to O- and E-band amplifiers due to their potential to be next in line for expanding commercial telecommunication networks. First of all, the first stabilisation of both phosphorous and silica related centres was presented in paper [65] which showed a combined amplification bandwidth of 116 nm. The record 40 dB gain BDFA in O-band was reported in

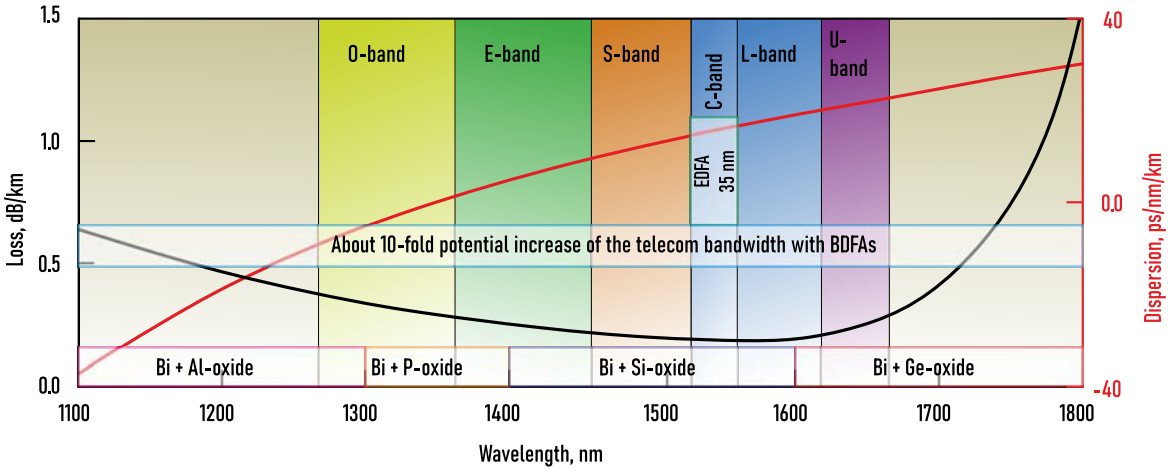

Fig. 2.9 Optical bands that BDFAs can provide gain. in

the paper [66]. The first attempts of data transmission have been reported in O-band [67, 68] and E-band supported by BDFAs [69].

Despite the aforementioned progress, several problems of BDFA have been addressed but not resolved. The clusterisation process that occurs in the Bi-doped fibres significantly limits the maximal concentration of bismuth in the core of the fibre. The occurring clusters significantly increase passive loss of the fibre, thus all the fibres are produced below the threshold of clusterisation. This way, the fibre length required to achieve a substantial gain is a magnitude higher than that used for commercial EDFAs and is typically more than 100 m. Another problem that is caused by the low bismuth concentration in the fibre is unavailability to measure the concentration of Bi-related centres in the core. The problem is significantly complicated due to the fact that bismuth can form different Bi-related centres in the fibre and it is unknown what are the real ratios between, for instance, silica Bi-related centres and germanium Bi-related centres. Moreover, uniformity of the concentration of Bi along the length of the fibre is unclear. As conventional rate equations require knowledge of the concentration of active ions, it is complicated to solve rate equations for Bi-doped systems.

The work in this thesis focuses on the development of BDFAs in E- and S-bands [63], as these amplifiers are less investigated and BDFA seems the most promising candidate for the expanding of current network bandwidth through utilising MBT in O- and E-bands. The different methods of modelling of BDFAs are proposed and tested along with the details of different fibres in Chapter 3. Moreover, a great deal of attention is paid to the development of a test bed for IM/DD and coherent transmission in E-band and incorporation of BDFAs in ulta-wideband transmission networks [70]. As the next step, differences between most common types of Bi-doped fibres are considered, including energy diagrams and methods of modelling.

Chapter 3

Bismuth-doped fibres

3.1 Fabrication of bismuth-doped fibres

Fabrication of almost any types of fibres is usually divided into two fundamental steps: preform formation and fibre drawing. Modified chemical vapour deposition (MCVD) is the most commonly used method for fabrication of fibre preform, and in particular BDF preforms. To produce a preform volatile liquid halide, precursors (i.e $GeCl_4, POCl_3, BBr_3, SiCl_4$, and SF_6) that have high vapour pressure at a temperature slightly higher than the room one ($30°C$) are sent into a rotating reference silica tube while heating it up using an oxyhydrogen burner. The core composition depends on various factors like atmospheric pressure and temperature of the burner. Moreover, the core thickness can be controlled by the number of deposited layers. After that, the preform with a hole in the centre is collapsed and follows sealing of the glass tube to get a solid preform. The advantage of the MCVD solution is that it is robust and convenient to experiment with to develop different preforms with various characteristics.

The process of rare earth doped preforms fabrication involves two steps. The first step predominantly targets minimisation of contaminants in the core by passing a SF_6 gas mixture and oxygen through the reference tube while the tube is being heated up by a burner. After that, vitrified silica or silica with phosphorous and germanium is deposited at a low temperature in the core. This layer is essential for rare earth deposition into the core. In the second step the reference tube with deposited layers is solution doped by keeping it in an alcoholic solution of the required rare earth dopant for a specified time. This process forms a porous layer with the desired rare-earth dopants. After the porous layer is deposited, the tube is dehydrated with the help of O_2 or N_2 flow. Next, the dried tube is heated in the presence of oxygen for conversion of rare earth dopants into corresponding oxides. In the final stage, the tube containing the rare earth-doped core is collapsed to produce the preform. Typically Bi

is incorporated into the core through solution doping while forming the porous layer [71]. Different other co-dopants can be introduced at various stages of the preform fabrication.

When the preform is ready it can be used for drawing. The typical drawing process is presented in Figure 3.1. The process of drawing Bi-doped fibres is similar to the same process for conventional rare earth preforms. The drawing is usually performed with the speed that is calculated from the preform core and preform cladding diameters, and feed speed.

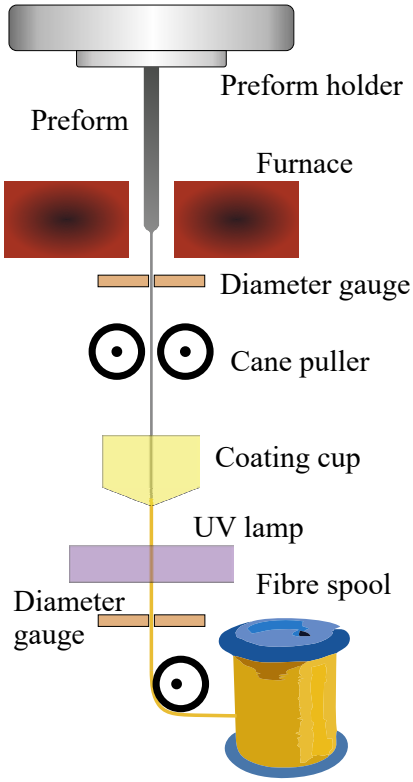

Fig. 3.1 Fibre drawing setup.

The preform holder is used to hold the preform attached to it. The preform is located at the centre of the furnace and moved into the heating area of the furnace. After the preform is heated up, a drop is formed from the output of the furnace and this drop is falling down by the force of gravity. When the drop followed by thin fibre comes out of the furnace, it is cut off the fibre. Additionally, fibre can be taken through a diameter gauge for a precise control of the fibre diameter. Then the fibre is fed into a cane puller. Once the required diameter is reached, the fibre can be fed into a coating cup where the coating is applied. Immediately after the coating, the fibre passes through an ultraviolet lamp where the coating is cured. Then, the fibre is eventually collected on a spool.

3.2 Types of bismuth-doped fibres

Bismuth is a polyvalent element with four oxidation states: Bi^{5+}, Bi^{3+}, Bi^{2+} and Bi^{+}. Two processes take place in molten polyvalent element-doped glass: oxidation (as it has been mentioned in the previous Chapter, Bi-doped fibres can be developed with inclusion of different co-dopants in the core of the fibre along with bismuth to enable amplification in various spectral bands at higher valence state) and reduction (at a lower valence state) [72]. This happens due to the fact that inner subshells of Bi are completely filled and the outer 6s and 6p electrons significantly interact with the host material, thus, bismuth shows substantial host-dependent absorption and emission cross-sections. In the subsections below, Bi-doped fibres based on different host materials are considered.

3.2.1 Aluminosilicate fibres

The first Bi-doped glass was presented by Fujimo and Nakatsuka in 2001 [73]. In that paper, an aluminosilicate glass doped with bismuth had luminiscence in spectral region from 1100-1500 nm. In 2005, the first Bi-doped fibre fabricated using the MCVD-solution doping technique was presented in paper [74]. This fibre was also based on aluminosilicate host glass and had luminescence from 1000 to 1300 nm.

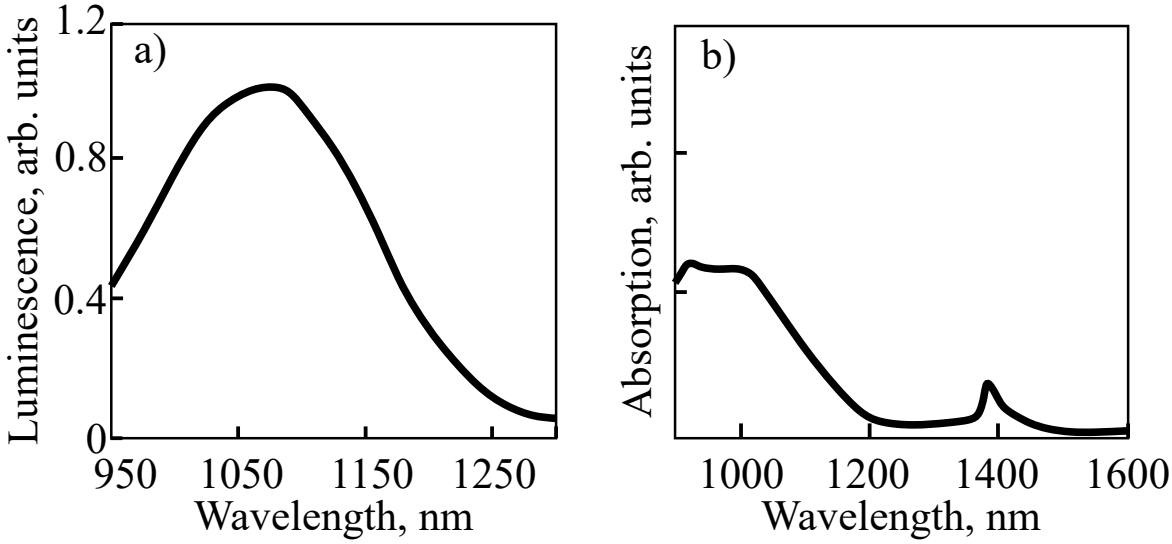

Fig. 3.2 a) Luminescence and b) absorption spectra of aluminosilicate Bi-doped fibre.

The bismuth active centres (BACs) related to aluminium interact with radiation at 500 nm, 700 nm, 800 nm, and 1000 nm and significantly absorb it. Bi-doped fibres with aluminosilicate host have the maximum of the emission around 1100 nm. The luminescence spectra of aluminosilicate Bi-doped fibre is presented in Figure 3.2 [75],a. Absorption of

the aluminosilicate Bi-dope is presented in Figure 3.2,b[76]. The composition of the host material and pump power can significantly shift the spectra of luminescence and spectra of gain of Bi-doped fibres.

Figure 3.3 shows the energy level diagram proposed in paper [77]. Based on the energy diagram to achieve effective amplification of optical radiation in vicinity of 1100 nm, the transition from the triplet state 1 (T_1) to the ground singlet state S_0 should be used. The most efficient pump transition is S_0 to S_1 (ground singlet state to upper singlet state). The transition between levels S_1 and T_1 is predominantly non-radiative. Thus, amplification of the signal in aluminosilicate fibre can be described by 3-level system presented in Appendix A.

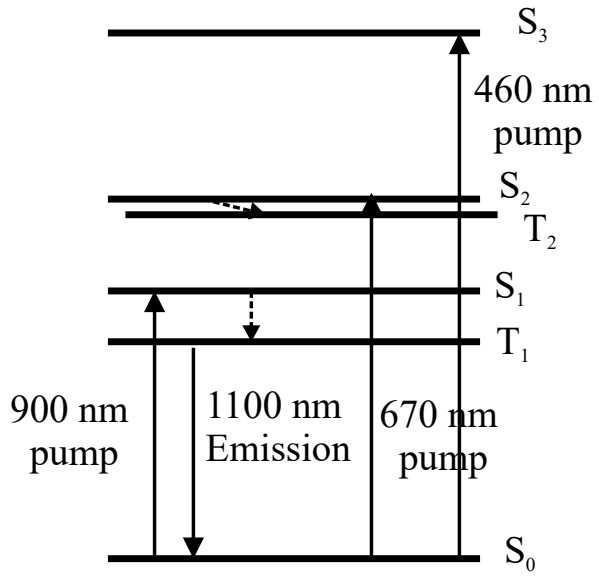

Fig. 3.3 Energy diagram of Al-BAC. Solid lines indicate transitions of absorption and emission, and dotted lines indicate nonradiative transitions; the transition wavelengths are given in nm.

After demonstration of the first aluminosilicate Bi-doped fibre, a great deal of attention was paid to development of Bi-doped fibre lasers [60, 78]. Although efforts were made to develop aluminosilicate Bi-doped fibre lasers in the past, there was much less progress in developing amplifiers around 1100 nm in comparison to other Bi-doped fibre amplifiers.

3.2.2 Phosphosilicate fibres

After successful demonstration of the first aluminosilicate Bi-doped fibres, it was discovered that by using different co-dopants of the glass instead of Al, spectral band of the amplification can be substantially shifted. The first demonstration of the Bi-doped fibre with phosphorous co-doping was made by authors in paper [79], who investigated P_2O_5-GeO_2-SiO_2-Bi_2O_3

core preforms and fibres and reported on the red-shifted broadband fluorescence with peak at 1300 nm observed in glass of such composition under 488 nm laser excitation. Luminescence of the BAC-P is presented in Figure 3.4,a [80]. Absorption of the phosposilicate Bi-dope is presented in Figure 3.4,b[76]. The phosposilicate fibre features a maximum of gain in vicinity of 1350 nm, and the luminescence tail goes up to almost 1500 nm.

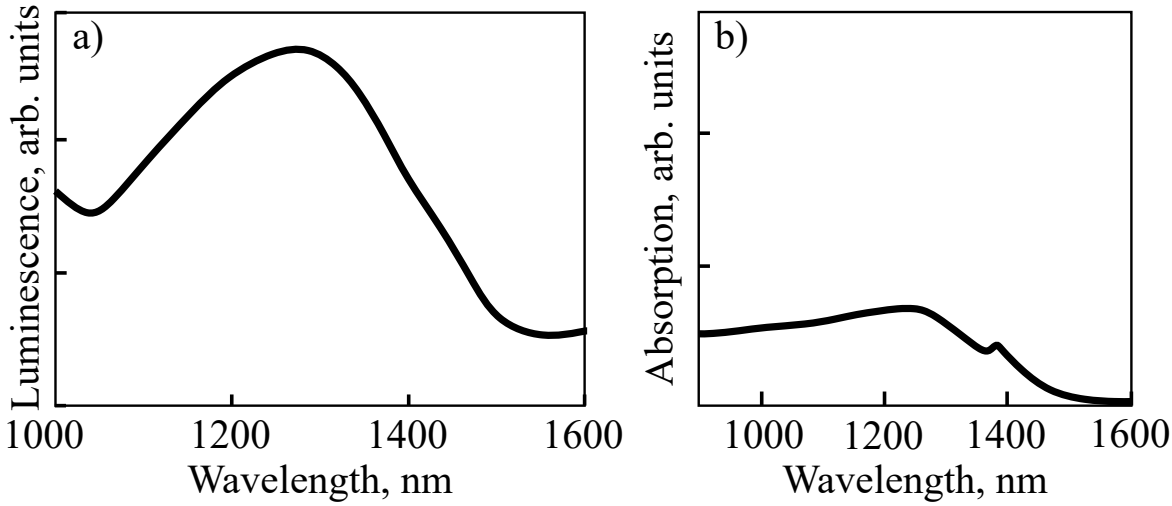

Fig. 3.4 a) Luminescence and b) absorption spectra of phosphosilicate Bi-doped fibre.

Figure 3.5 shows the energy level diagram of the BAC related to phosphorus [81]. The radiation at wavelengths of 220 nm, 350 nm, 390 nm, 780 nm and 1250-1300 can interact with the BACs and be absorbed by them. As the transition between ground level S_0 and S_1 can be used as both pump and emission transitions enabled by Stark effect, the modelling of the phosposilicate fibre can be described by the two level system described in Appendix B.

One of the first demonstrations of an amplifier based on Bi-doped phophosilicate fibre was reported in 2009 [82]. Its operation bandwidth was 1300-1340 nm, the maximum gain was 25 dB, and the NF was 5 dB. The positive gain was observed in a wide range of 1283-1372 nm. The pump was located at 1230 nm and its power was limited by 500 mW. It was later observed that the performance of Bi-doped phosphosilicate fibre was better when introducing a small amount of Ge in the core [83]. The addition of Ge makes the luminescence window broad, covering the entire 1300-1500 nm band. Now most of Bi-doped fibres presented in the literature based on a phosphosilicate host also have a small concentration of germanium. Recently, a number of works reporting successful stabilisation of two BACs related to both phosphorus and silica has been reported [20, 84]. Both of these papers reported similar results in terms of total achieved 3 dB bandwidth exceeding 115 nm in the spectral range of 1300-1450 nm. However, the work by Wang et al. presented a fibre with still some concentration of water in the core, leading to a substantial dip in the gain spectra around 1380

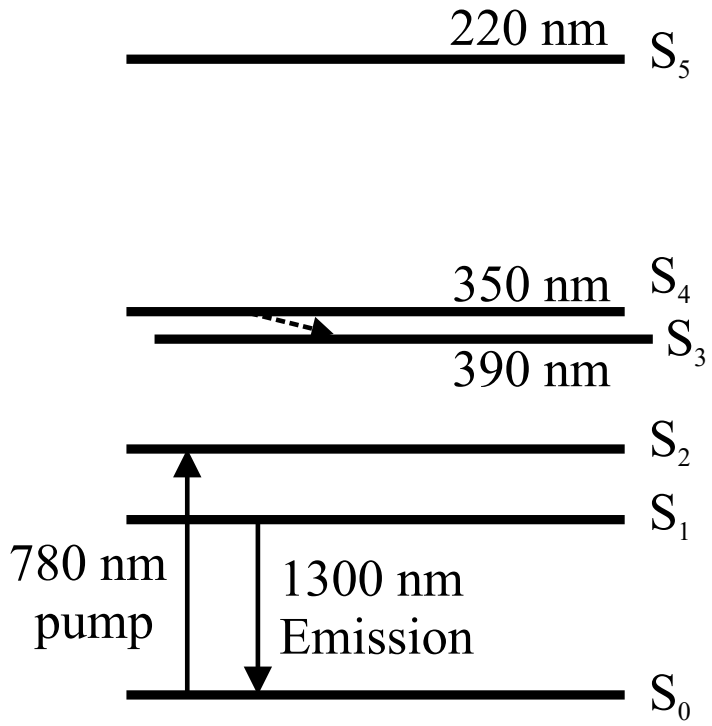

Fig. 3.5 Energy diagram of P-BAC. Solid lines indicate transitions of absorption and emission; the transition wavelengths are given in nm.

nm. The paper by Ososkov lacks this dip in the spectrum and the setup allows to achieve a completely flattop gain spectrum with maximum gain of 30 db, and NF of 6 dB. Along with the development of wideband BDFAs based on simultaneous stabilisation of BAC-P and BAC-Si, an alternative approach has been utilised to develop high-gain amplifiers [66]. To achieve gain as high as 39 dB, a double-pass scheme was used based on two circulators. The NF of the setup was around 5 dB.

There has been a number of works reporting data transmission enabled by BDFAs operation in the O-band. The transmission of 4x53 GBaud PAM4 signals in the spectral range of 1271-1331 nm through total of 10 km SMF enabled by BDFA is presented in paper [85]. Prior to that, a transmission of 8×26.6 Gbaud/s PAM-4 channels through 55 km of G.652 fibre was reported in [68]. A similar performance has been achieved with 4× 50-Gb/s CWDM IM/DD channels transmitted through 100-km long SSMF and amplified by two BDFAs [86]. Simultaneous transmission in O+C band through 50-km-long SMF was reported in paper [87]. Moreover, a multiband E+C transmission through 1 km of hollow core fibre was reported [88]. The modulation format of the signal was again PAM4. Despite a numerous demonstration of IM/DD transmission in O-band, coherent transmission is yet to be demonstrated.

3.2.3 Low-germanosilicate fibres

The first E-band amplification using Bi-doped fibre was demonstrated in 2008 by Dvoyrin [89]. Even though the first paper stated the fibre to be aluminosilicate, it has later been proved that the 1400-1500 nm amplification range is related to reaction of the Bi-doped active centres with silica. The efficiency of this transition can be significantly improved by low concentration of germanium in the core of the fibre [90, 91]. The luminescence spectrum of Si-BAC is presented in Figure 3.6,a [92]. Absorption of the Si-BAC is presented in Figure 3.6,b[76]. A fibre with low concentration of germanium usually has a maximum of luminescence around 1430 nm. The whole luminescence range is from 1300-1500 nm, and it naturally overlaps with phosphosilicate fibre.

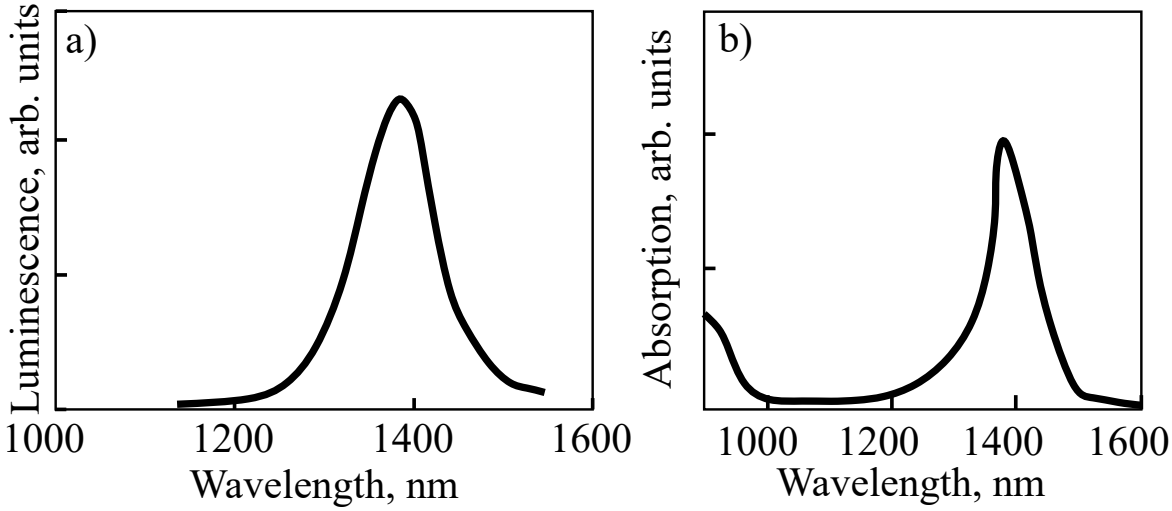

Fig. 3.6 a) Luminescence and b) absorption spectra of low-germanosilicate Bi-doped fibre.

The energy level diagram of the Si-BAC is considered in Figure 3.7 [76]. The transition SE_0 to SE_1 is usually used for pumping with the maximum wavelength around 1360 nm. The opposite transition SE_1 to SE_0 can support signal amplification in the spectral range from 1390-1510 nm enabled by Stark-split energy levels. The principle of work is similar to one of phosposilicate fibre and can be modelled by just the two-level system described in details in Appendix B.

The Bi-doped low-germanosilicate fibre amplifiers have shown significant progress recently. The focus of work described in this thesis is on E-band Bi-doped low-germanosilicate fibre amplifiers due to their excellent performance and as the E-band seems to be a natural next step after utilisation of L-band EDFAs and S-band TDFAs. Moreover, Bi-doped low-germanosilicate fibre amplifiers can provide substantial gain in the part of S-band along with the main amplification covering half of the E-band. Prior to the beginning of the work on

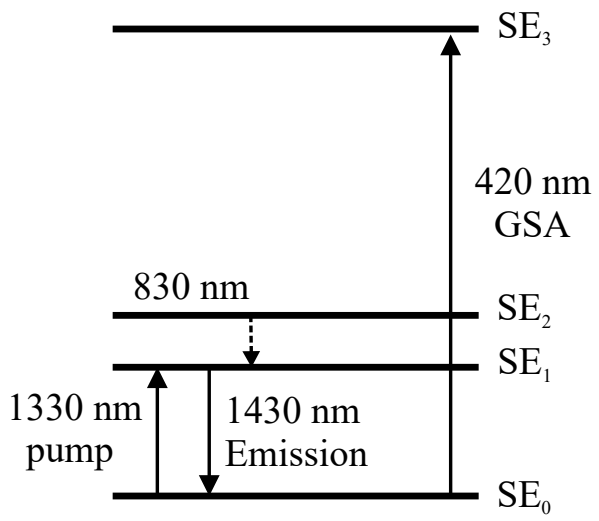

Fig. 3.7 Energy diagram of Si-BAC. Solid lines indicate transitions of absorption and emission, and dotted lines indicate nonradiative transitions; the transition wavelengths are given in nm.

this thesis, there has been a number of BDFAs reported in the literature [69, 93]. The first paper featured simultaneous 4-channel amplification in E-band with a maximum gain of 28 dB and minimal NF of 7.2 dB. The second paper showed an E-band BDFA with 26 dB gain and 7.5 dB NF. Moreover, it also showed the first ever demonstration of data transmission enabled by BDFA. The 80-km long SMF link was supported by a single E-band BDFA to allow 10.6 Gbit/s OOK NRZ channel transmission.

Since the beginning of this work, there has been a number of papers showing significant progress in E-band BDFAs, published by Aston Insitute of Photonic Technologies and other research groups. They include a 38-dB gain germanosilicate BDFA based on a double-pass scheme [94], an E- and S-band amplifier development and characterisation with 31 dB gain and 4.8 dB NF [63], E- and S-band BDFA with 38 dB gain, 4.5 dB NF and 30% PCE [95]. Moreover, several papers reported record transmission length in E-band enabled by a single BDFA [96]. 4 channels of 10Gbit/s NRZ OOK were transmitted through a 160 km-long transmission line supported by a single BDFA with 30 dB gain. Moreover, first demonstration of coherent transmission in E-band enabled by BDFA was reported in paper [70]. 4 channels of SP 50 GBaud QPSK in spectral region of 1410-1450 nm were transmitted through 60 km long transmission line that was enabled by two E-band BDFAs. Later, a combined approach was proposed for multi-band transmission in E-S-C-L bands enabled by an amplifier based on combined bismuth-doped fibre and discrete Raman amplification. The developed amplifier has the maximum gain of 18 dB, the lowest NF of 5.8 dB and covers 195 nm bandwidth. The transmission through 70 km was performed with 143 channels spread across E-S-C-L

bands of DP 30 Gbaud 16 QAM [97]. Finally, the transmission of 4xDP 30 GBaud 16QAM channels through 160 km was performed using three BDFAs operating in E-band [98], which is the record transmission of the coherent signal in E-band. Some of the work mentioned here is described in detail in this thesis.

3.2.4 High-germanosilicate fibres

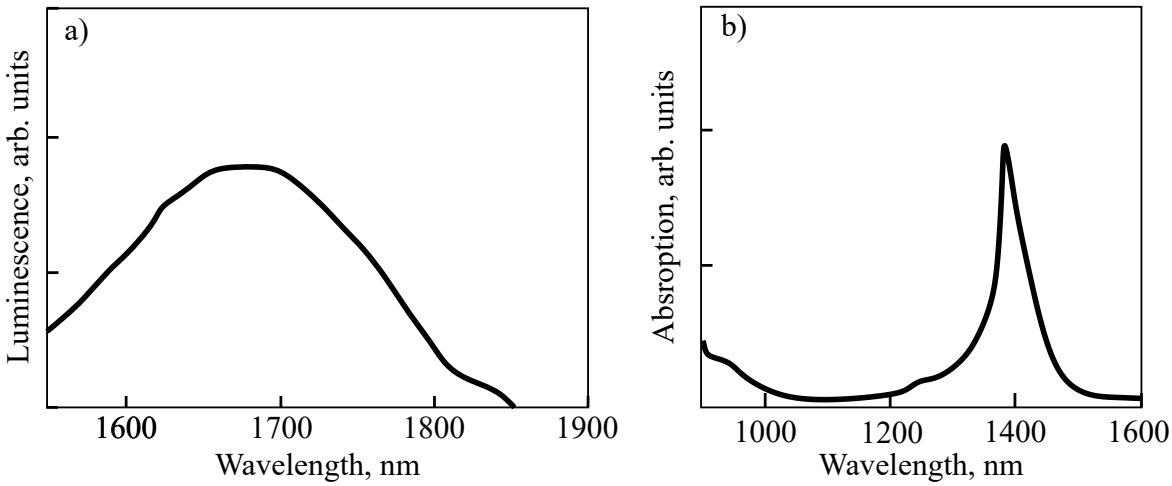

Fig. 3.8 a) Luminescence and b) absorption spectra of germanosilicate Bi-doped fibre.

It has been observed that by increasing the Ge concentration above 50mol% in Bi-doped germanosilicate fibres, the emission spectra of the fibre can be shifted toward longer wavelength range (1600-1800 nm). The luminescence spectra of a Bi-doped germanosilicate fibre with high germanium concentration is presented in Figure 3.8,a [76]. Absorption of the germanosilicate Bi-doped fibre is presented in Figure 3.4,b[92]. The radiation starts roughly at 1500 nm and expands toward longer wavelengths up to 1850 nm. The maximum of the luminescence is in vicinity of 1675 nm. This spectra band is important for expending the optical network capacity through transmission in U-band (1625-1675 nm) where silicate fibres experience slightly higher attenuation to C-band, however, still not as critical in comparison to the wavelengths higher than 1700 nm.

The energy level diagram of Ge-BAC is presented in Figure 3.9 [76]. The radiation with the average wavelength of 463 nm, 925 nm, and 1650 nm can interact with the energy levels presented in the Ge-BAC. To achieve generation at 1650 nm, the transition form upper level S_1 to ground level S_0 can be used. To pump the active media, the radiation with wavelength in vicinity of 1550 nm is commonly used [99]. As it is clear from the energy level diagram, a Bi-doped high-germanosilicate fibre can be described by two-level system enabled by the Stark energy level split. The equations for two-level systems are described in section B.

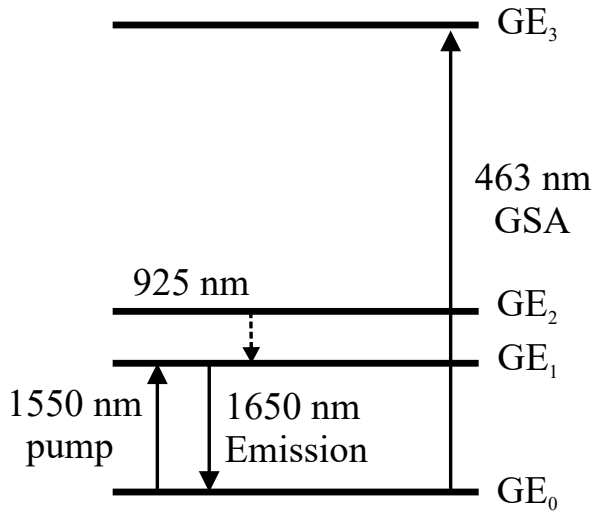

Fig. 3.9 Energy diagram of Ge-BAC. Solid lines indicate transitions of absorption and emission, and dotted lines indicate nonradiative transitions; the transition wavelengths are given in nm.

A number of works have reported a successful development of U-band BDFAs based on high-germanosilicate fibre. The 23 dB gain amplifier with the bandwidth of 40 nm in vicinity of 1710 nm was reported in the paper [99, 100]. The amplifier is based on a short segment of the fibre of just 60 m and pumped by two LDs at 1550 nm with 150 mW output power each. The NF of the developed amplifier is 7 dB. Relatively low gain and high NF can be explained by the shortness of the fibre (for BDFAs) and low pump powers. However, there has been no demonstrations of successful signal transmission enabled by U-band BDFAs.

3.3 Parameters of Bi-doped fibres

In this section, the main parameters of the active Bi-doped fibre are considered. As only E-band BDFAs are considered in this work, only 2-level energy level rate equations should be solved that are presented in Appendix B. As the first step, all unknown model parameters required for solving the rate equations should be defined. The Bi-doped optical fibre used in the first developed amplifier (BDFA-1 described in section 4.2) has similar characteristics to the SMF. S_s and S_p are effective mode areas. These parameters can be defined through the mode field diameter:

$$S = \pi w^2/4, \tag{3.1}$$

where w is the mode field diameter that can be defined from the following equation:

$$w = a(0.65 + \frac{1.619}{V^{3/2}} + \frac{2.879}{V^6}), \tag{3.2}$$

where a is the fibre core radius, and V is a dimensionless parameter which is often used in the context of step-index fibres. It determines the fraction of the optical power in a certain mode which is confined to the fibre core. For single-mode fibres, that fraction is low for low V values (e.g. below 1), and reaches $\approx 90\%$ near the single-mode cut-off at $V \approx 2.405$. V number is defined using the following equation:

$$V = \frac{2\pi}{\lambda} aNA = \frac{2\pi}{\lambda}\sqrt{n_{core}^2 - n_{cladding}^2}, \tag{3.3}$$

where λ is the wavelength, NA is the numerical aperture, n_{core} is the refractive index of fibre core, and $n_{cladding}$ is the refractive index of fibre cladding.

There is a number of unknown parameters in equations required for two-level system presented in Appendix B. Γ_s and Γ_p are the doped core and field mode overlap integrals for both signal and pump wavelength. They are simply defined as core area divided by effective mode areas of signal and pump, respectively. α_s and α_p are the signal and pump losses in the fibre. n_t is the dopant concentration in the fibre core which typically cannot be determined experimentally in Bi-doped fibres due to its low concentration (the concentration of BACs is below the detection level). However, the upper limit can be defined from the preform Bi-doping concentration through the total weight of one mole of composite glass [44]:

$$W = x(SiO_2)Z(SiO_2) + x(GeO_2)Z(GeO_2) + x(Bi_2O_3)Z(Bi_2O_3)), \tag{3.4}$$

where $x(i)$ is the fractional molar concentration (in mol%) and Z is the corresponding molecule mass. The concentration of Bismuth Oxide is negligible. Assuming that D is the glass density and N_A is the Avogadro number, the Bi_2O_3 concentration in molecules per cubic centimetre is given by:

$$n(BAC) = x(BAC)\frac{DN_A}{W}. \tag{3.5}$$

As one of the fibres used in this project has a similar concentration as the fibre reported in [92], we assume that the upper limit of the ion concentration N would be limited by mole concentration of 0.001%. Thereby, there are five more parameters that are unknown: σ_{sa} is the signal absorption cross-section, σ_{se} is the signal emission cross-section, σ_{pa} is the pump absorption cross-section, σ_{pe} is the pump emission cross-section, and τ is the relaxation lifetime. The lifetime can be measured experimentally using a high speed oscilloscope and

receiver. However, the emission and absorption cross sections cannot be determined due to their connection to the concentration of BACs in the fibre.

The number of unknown parameters can be further reduced by the McCumber [101] relation between emission and absorption cross-sections. The theory of McCumber is a versatile tool that allows one of the two cross-sections to be calculated if the other is known from measurements. This theory is a generalisation of the original Einstein A and B coefficients approach [102] and can be applied to the broadband transitions between the Stark manifolds of a rare-earth ion. The relationship between the absorption and the emission cross-sections for transitions between two manifolds is given by the McCumber relation:

$$\sigma_e(\nu) = \sigma_a(\nu) exp(\frac{E - h\nu}{k_B T}), \tag{3.6}$$

where σ_e is the emission cross-section, σ_a is the absorption cross-section, ν is the frequency of radiation, E is an effective energy difference between two manifolds[103], k_B is Boltzmann's constant, and T is the absolute temperature.

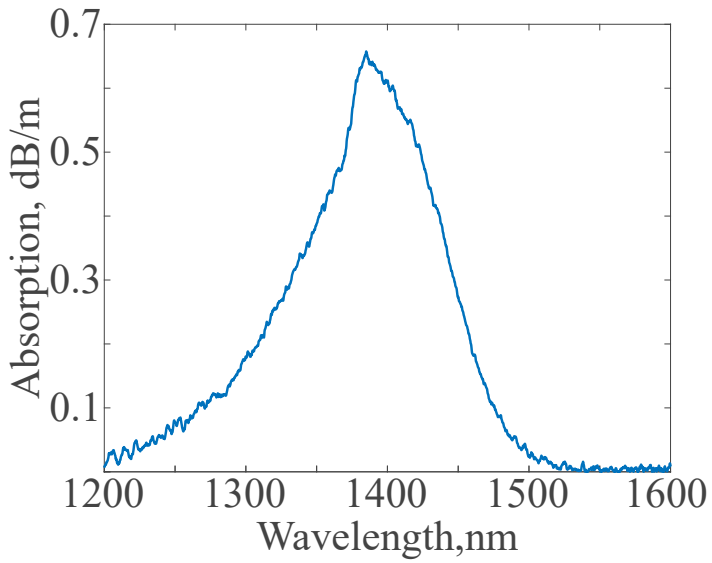

Fig. 3.10 Experimentally measured absorption of the BDF used for the amplifier BDFA-1 described in section 4.2

Finally, optical absorption of the fibre should be determined. This is an important parameter of the fibre that can be experimentally determined, however will not be used in the modelling. For the measurement of optical absorption of BDF a fairly short piece of BDF was used (3 m). The cut-back-method in combination with an infrared lamp coupled into a single-mode fibre was used to determine the spectrum of the BDF absorption. As a first step the radiation of the lamp was transmitted through a 3-m piece of BDF and the spectrum at the

output of the BDF was recorded (Spectrum 1). After that, the piece of BDF was decreased by 0.5 m and the spectrum was measured again (Spectrum 2). Finally, another piece of 0.5 m of BDF was cut out leaving only 2-m BDF piece (Spectrum 3). The consequent spectrum was recorded again. To obtain the loss of the fibre the value of the Spectrum 2 should be deducted from the Spectrum 3 and divided by the length of the fibre taken (0.5 m). The same approach should be repeated for the pair of Spectrum 1 and Spectrum 2. The result of the average absorption spectrum is presented in Figure 3.10. It should be noted that the discrepancy between the first and second measurements were minimal indicating a correctly utilised measurement. Fibre features the maximum absorption of 0.65 dB/m at the wavelength of 1385 nm.

3.4 Modelling of bismuth-doped fibres

3.4.1 Conventional modelling of E-band bismuth-doped fibre amplifier

The work in this subsection was performed in collaboration with Dr Egor Manuylovich from AiPT who kindly agreed to assist with developing the numerical model for the fibre parameters optimisation. By considering equations for two-level system (Appendix B) and the described methodology for boundary value problems solving (Appendix D) we have some known parameters such as fibre length L, Planck's constant h, signal and pump frequencies ν_s and ν_p, attenuation constants at signal and pump wavelengths α_s and α_p. Some parameters can be calculated such as signal and pump mode areas A_s and A_p, signal-core and pump-core overlap integrals Γ_s and Γ_p. Other parameters such as signal emission and absorption cross-sections σ_{sa} and σ_{se}, pump emission and absorption cross-sections σ_{pa} and σ_{pe}, concentration of Bismuth ions n_{Bi} and lifetime of upper level τ should be determined. It is worth noting that the equation boundary-value problem for the two level system (described in Appendix B) remains mathematically the same if we multiply ion concentration and lifetime by some constant and divide emission and absorption cross-sections by the same constant. To prove this concept, the reader can refer to the end of Appendix B.

All unknown constants (cross-sections, lifetime, and concentration) cannot be determined during the optimisation, however, lifetime can be obtained from the measurement that is planned to be conducted in the future. Thus, we choose to fix the lifetime to be equal to $\tau = 1ms$. When the real value of this constant is determined separately, the concentration and cross sections values can be corrected.

Using the calculated solution, the signal gain $G_{calc} = P_s(z = L)/P_s(z = 0)$ can be determined for specific values of pump power and initial signal power. Then it can be compared

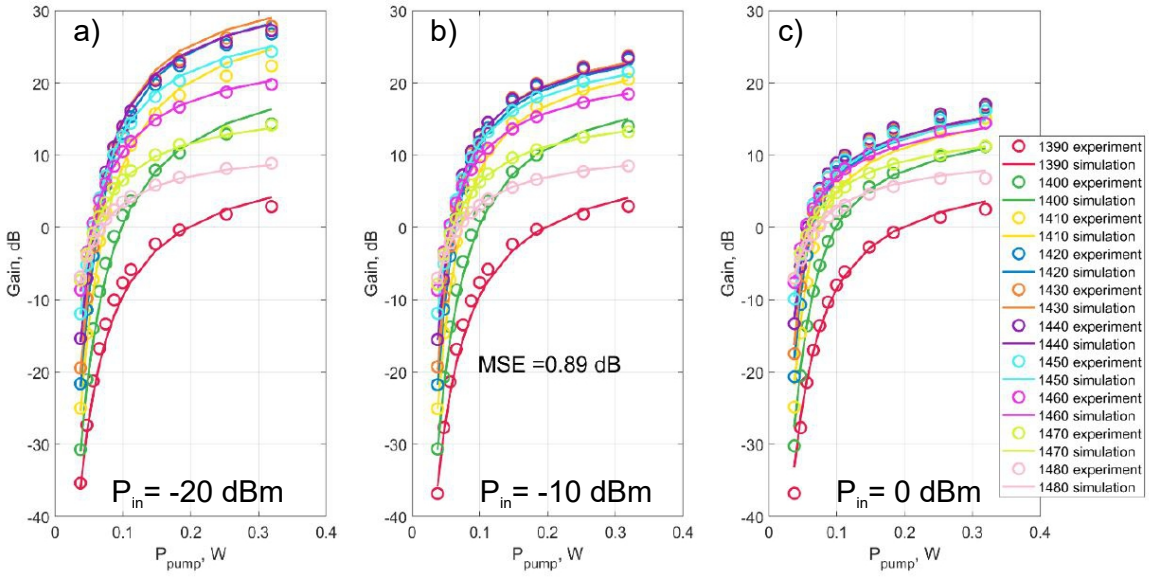

Fig. 3.11 The result of numerical optimisation for -20 dBm, -10 dBm, and 0 dBm input signal powers using experimental data obtained in section 4.2. Circles indicate experimental data, and the solid line indicates the modelling results.

with experimental gain G_{exp}. Then, an optimisation problem on minimising the deference between measured and calculated gain values is solved for various values of pump powers and initial signal powers to determine signal emission and absorption cross sections σ_{sa} and σ_{se}, pump emission and absorption cross sections σ_{pa} and σ_{pe}, and concentration of Bismuth ions n_{Bi}.

$$\{n_{Bi}, \sigma_{se}, \sigma_{pe}, \sigma_{sa}, \sigma_{pa}\} = argmin(||G_{calc} - G_{exp}||) \tag{3.7}$$

The optimisation problem is solved using Nelder-Mead algorithm [104] for the experimental data obtained in Section 4.2 shown in Figure 3.11. The mean square error (MSE) is of 0.89 dB across all wavelengths, all pump powers and all initial signal powers. There is a noticeable feature of the optimisation that can be concluded as following: for lower input signal powers the simulated gain (after optimisation) is generally higher that the experimental one. For higher input signal power the obtained results are opposite: the simulated gain is lower than experimentally measured. This effect can be explained by the fact that the ASE noise was only modelled in a narrow spectral bandwidth surrounding the signal. In reality, ASE noise usually spans over the whole bandwidth of emission cross section. Moreover, in the case of small signal amplification (i.e. -25 dBm) ASE noise power can be comparable or higher than that of the signal. Thus, in the future work the ASE noise calculation in the

whole bandwidth of operation should be included in optimisation. The optimisation for the separate 0 dBm for each initial signal power is also performed separately and the results are presented in Figure 3.12.

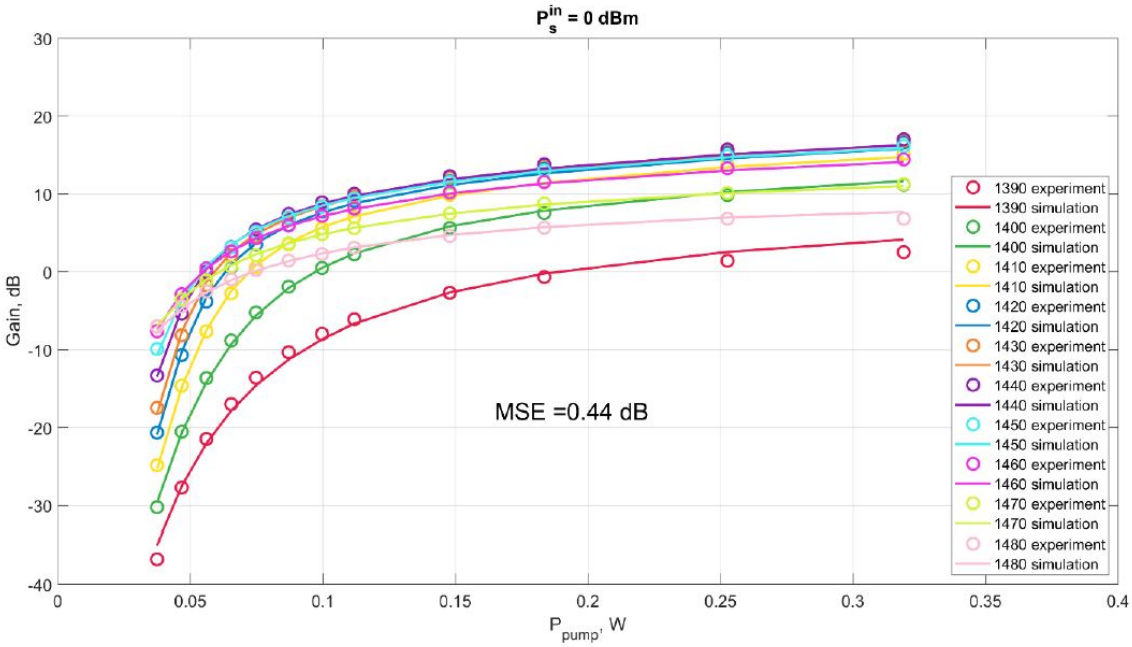

Fig. 3.12 The result of numerical optimisation using experimental data obtained in section 4.2. Circles indicate experimental data, and the solid line - the modelling.

The comparison between the optimised parameters for two different optimisation data sets are presented in Figure 3.13. Even though the discrepancy between the obtained results is low, the testing of the obtained parameters was made with a different data set of backward pumping. Unfortunately, the modelling of the amplifier with backward pump and optimised values gave an unsatisfactory result of correspondence to the experimental data, thus, alternative approaches should be sought (i.e neural-network (NN) approach).

More importantly, other combinations of fibre parameters were found to have a similar alignment with experimental data as provided in Figure 3.11 which depended a lot on the initial guesses of the optimised parameters. This can be explained by the complexity of the solved equations and by the fact that too many parameters of the fibre are unknown, giving too much degree of freedom for the sought parameters. Other methods of indirect modelling can be applied for modelling of the gain and NF performance of BDFAs. For example, a ML "black box" approach can be applied to studying BDFAs, when the amplifier is considered only as a black box that translates multiple inputs to multiple outputs. The next Subsection 3.4.2 is devoted to investigating this approach. Moreover, sparse regression

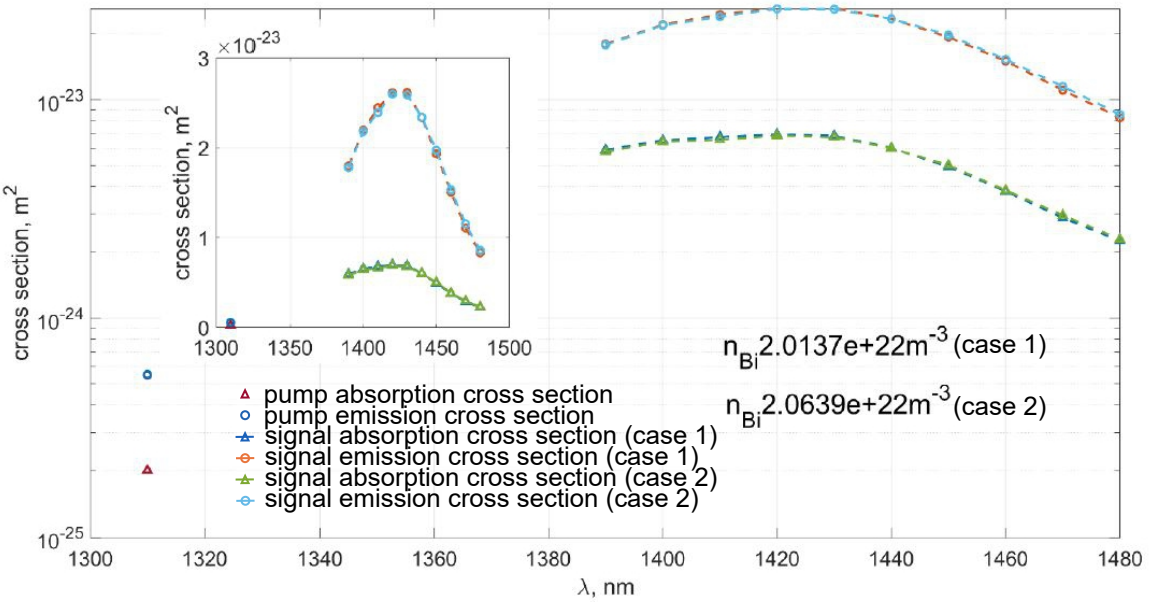

Fig. 3.13 The optimised values of the absorption and emission cross sections obtained from the dataset containing single signal power (Case 2) and three different ones: 0 dBm, -10 dBm, -20 dBm (Case 1).

can be used to find the underlying equations with the smallest possible complexity required to accurately represent the measured data. The resulting nonlinear models can balance complexity with the descriptive ability while avoiding overfitting.

3.4.2 Neural network modelling of a E-band bismuth-doped fibre amplifier

As it has been pointed out in the previous subsection, the conventional numerical modelling (using well-known rate equations) of BDFAs remains highly challenging mostly due to a relatively low concentration of the Bi-doped active centres, which cannot be precisely determined. Thus, it is important to develop an accurate, fast, and simple tool for the modelling of the signal amplification in the BDFA with only known initial pump and signal conditions. As a possible solution, NN-based techniques have already been applied for Er-doped fibre amplifiers [105, 106] and Raman fibre amplifiers [33, 107]. The machine learning approach in aforementioned works proved its accuracy and efficiency for the prediction of the channel amplification in complex systems like BDFAs. Moreover, such differentiable amplifier models used in conjunction with also differentiable optical channel models allow a

power profile optimisation using the gradient descent in reconfigurable optical networks, as also demonstrated in [106].

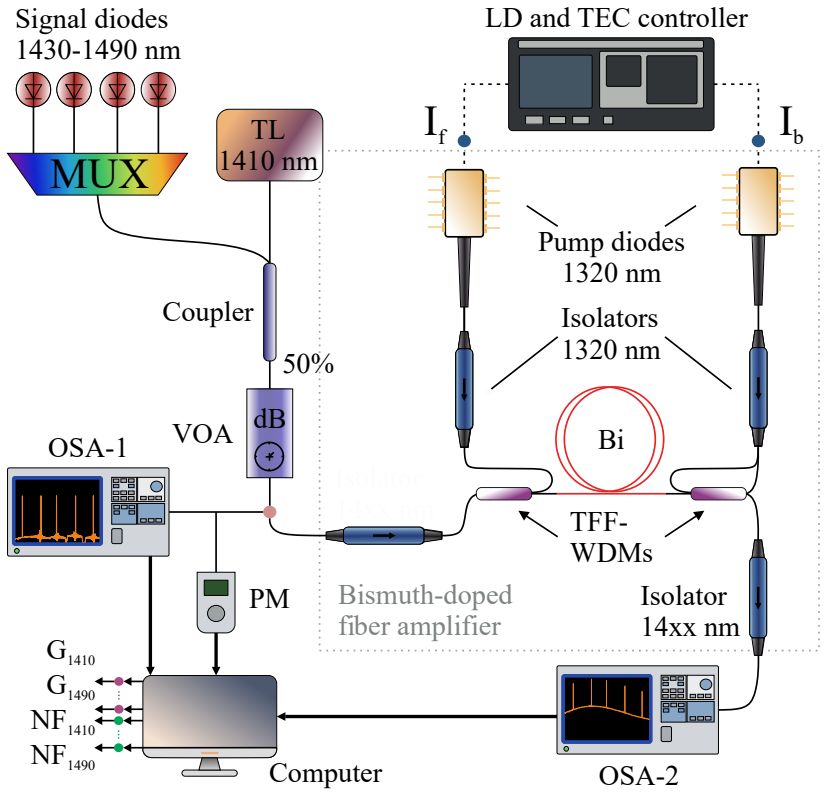

Fig. 3.14 Experimental setup for BDFA characterisation and data sets acquisition.

The work presented in this subsection was performed in tight collaboration with Technical University of Denmark (DTU) and Politecnico di Torino (Polito). The NN developed in this chapter was prepared by Dr Uiara Celine De Moura, Dr Ann Margareth Rosa Brusin, Dr Francesco Da Ros, Prof Andrea Carena, and Prof Darko Zibar. The resulting work was published in the paper [108]. We report the NN-based BDFA gain and NF model trained purely on experimental measurements of the five channel amplification in the spectral band of 1410-1490 nm using the BDFA with the bi-directional pumping scheme. Two different data sets are used for both training and testing: with just seven values, and uniformly distributed values of the total input signal power. The proposed model is then used to predict spectral dependencies of gain and NF for the specific total input signal powers and pump diode currents.

The experimental setup for gain and NF measurements for data sets acquisition is shown in Figure 3.14. The input signal is formed with the radiation of the tunable laser tuned to 1410 nm and coupled with the radiation of four signal diodes at 1430 nm, 1450 nm, 1470 nm, and 1490 nm combined in the multiplexer (MUX). After the 50:50 coupler the signal

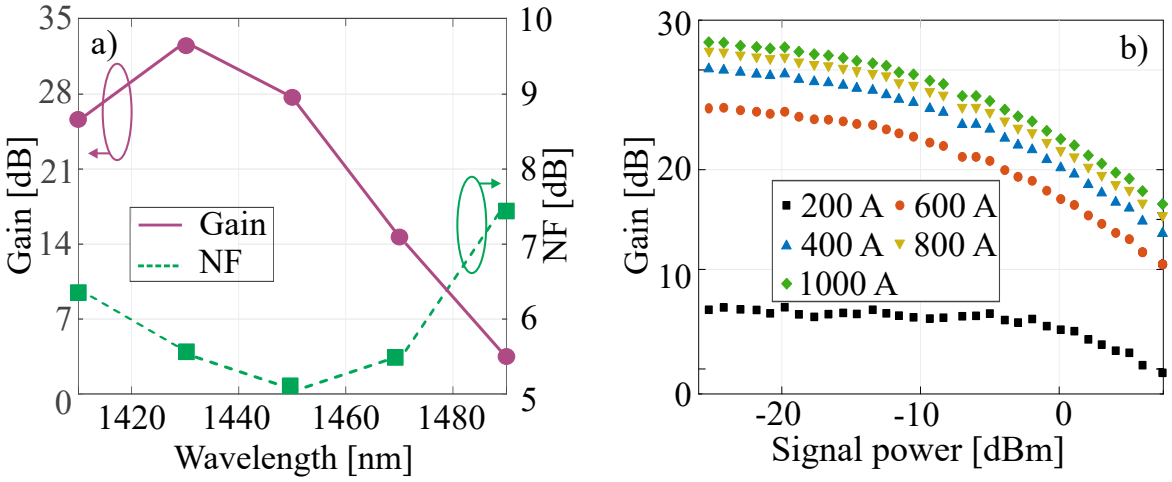

Fig. 3.15 a) Amplifier gain and noise figure as a function of wavelength achieved with 1000 mA pumps currents and -25 dBm signal power; b) Amplifier gain at 1430 nm as a function of total input signal power.

passes a VOA that allows the input power adjustment in the range from -25 dBm to 5 dBm. The radiation spectrum after the VOA is recorded by the optical spectrum analyser (OSA) and the total input signal power is measured by the power meter (PM). Then the signal enters the BDFA with a 320 m long Bi-doped germanosilicate fibre with 9 μm fibre core consisting of 95 mol% SiO_2, 5 mol% GeO_2 and <0.01 mol% of bismuth. Here we use two 1320 nm pump diodes controlled by the laser diode and thermoelectric cooler controller for the bi-directional pumping. The 1320 nm isolators are used for the pump diodes protection from the contra-propagating radiation. The thin film filter wavelength division multiplexers (TFF-WDMs) with very steep reflection and transmission bands allow an efficient coupling of the broadband signal and pump radiation. The signal spectrum at the output is recorded using the OSA.

The recorded spectra for input and output signals are then used for the gain and NF determination in the 1410-1490 nm wavelength range using the source subtraction technique [109]. The procedure of gain and NF measurements are explained in the details in Section 4.1. Gain and NF as functions of wavelength for 1000 mA pumps currents and the -25 dBm total input signal power for five channels are shown in Figure 3.15,a. The maximum achieved gain is 32.9 dB and the minimal NF is 5 dB at 1430 nm and 1450 nm, respectively. Figure 3.15,c shows the dependency of gain at 1430 nm on the total input signal power for different currents of both pump diodes. In the examined range, the gain dependency shows linear (for approximate total input powers <-10 dBm) and saturation behaviour (for approximate total input powers >-10 dBm) with the change of the total input power. Thus, it is highly important that the NN model has a good performance in both linear and saturation

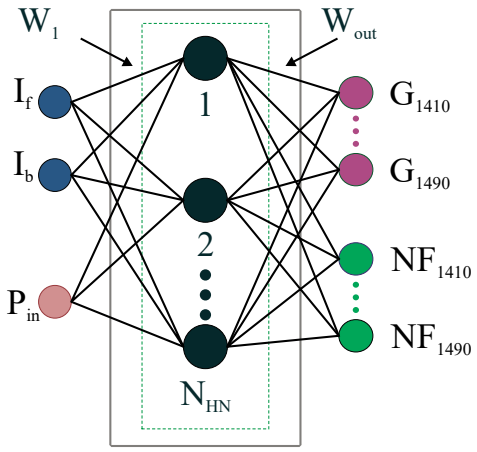

Fig. 3.16 Neural network architecture for learning the mapping between inputs (signal powers and pump currents) and outputs (gain and NF profiles).

regimes of the gain in terms of the total input signal power. The framework should also allow predictions for different values of pump currents, as the increase of the pump currents shows a nonlinear increment of gain.

The single layer NN architecture used to model the BDFA is shown in Figure 3.16. The inputs of the model are the backward pump diode current I_b, the forward pump diode current I_f, and the total input signal power of the 5 channels P_{in}. The outputs of the model are corresponding gains $(G_{1410},...,G_{1490})$, and NFs $(NF_{1410},...,NF_{1490})$ for all five signal wavelengths. The model is trained using the random projection (RP) [110] to learn the mapping between pump currents and the total input signal power to the gain and NF. A k-fold cross validation with k = 10 is applied for the model selection and the hyper-parameter optimisation. This process provides the optimised number of hidden nodes N_{HN}, the activation function f_{act}, the regularisation parameter λ, and the variance σ of the normal distribution. The regularisation parameter λ, and the variance σ are then used to calculate the output weights (W_{out}) and to assign the hidden layer weights (W_1), respectively. To improve the prediction capabilities of the NN, a model averaging twenty independently trained NNs is employed [107]. Therefore, gain and NF predictions are the average of the 20 NNs outputs. 20 independent NNs are achieved by obtaining 20 data sets using method of sampling with replacement.

The experimental data acquisition for the NN training consists of N different current values for the backward (I_b) and forward (I_f) pumps in the range of $[200:1000]$ mA and different values of the total input signal power (P_{in}) in the range of $[-25:5]$ dBm. Each case described by (I_b, I_f, P_{in}) is applied to the experimental setup (Figure 3.14.a) and the corresponding output spectra are measured and processed to obtain gain

Table 3.1 **Parameter values for different NN modelling cases. Values in square brackets separated by colon denote the boundary values of data set with the values randomly distributed between these boundary values. In contrast, values in curly brackets denote the only data set points existing in data set.**

Parameter	Case 1	Case 2	Case 3
Training data set			
I_b or I_f [mA]	[200:1000]	[200:1000]	[200:1000]
P_{in} [dBm]	$\{-25,-20,-15,-10,-5,0,5\}$	$\{-25,-20,-15,-10,-5,0,5\}$	[-25:5]
Testing data set			
I_b or I_f [mA]	[200:1000]	[200:1000]	[200:1000]
P_{in} [dBm]	$\{-25,-20,-15,-10,-5,0,5\}$	[-25:5]	[-25:5]

and NF information of the five signal channels. The final data set is in the form of $\mathscr{D} = \{(I_b^i, I_f^i, P_{in}^i, G_{1410}^i, ..., G_{1490}^i, NF_{1410}^i, ..., NF_{1490}^i) | i = 1, ..., N\}$ and is split into three parts: 63% for NN training, 7% for NN validation, and the remaining 30% for final tests. Data set size N varies for the different cases and is presented in the description of each case.

Firstly, the developed NN framework is trained and tested using a data set with discrete total input signal power levels. The parameter values for the different combinations of testing and training data sets are presented in Table 3.1. For the first case (Case 1 in Table 3.1), the data set is generated for each discrete P_{in} in the set $\{-25, -20, -15, -10, -5,\ 0,\ 5\}$ dBm. The data set for each discrete P_{in} consists of 3000 different I_b and I_f values drawn from uniform distributions in a log scale to provide an also uniform distribution for gain and NF in dB. The currents are converted back to the linear scale before applying them to the experimental setup. This process gives a total of N = 21000 points for all P_{in} cases. The k-fold cross validation results in N_{HN} = 1000, $f_{act} = \sin(x)$, regularisation parameters $\lambda = 10^{-10}$, and $\sigma = 10^{-2}$. The periodicity of sine in this particular case did not cause any issues with convergence, because the only use the central region near zero is used, where it is almost identical to tanh. To optimise the hyper-parameters we trained different NN models for different combinations of hyper-parameters (number of hidden nodes N_{HN}, activation function fact f_{act}, learning rate λ and variance σ for NN weights initialisation) and then we selected the model for which the lowest error, in terms of E_{MAX} , is achieved. The prediction performance is evaluated in terms of the maximum absolute error E_{MAX} between predicted and target profiles (for gain and NF) for the applied channels. The definition of E_{MAX} is the maximum absolute error between the predicted and the measured profiles among the 5 wavelengths. We preferred to consider the E_{MAX} as figure of merit instead of the E_{MEAN} because a low E_{MEAN} does not directly imply that the prediction is good. In fact, some

points can be below and other above the target profile, but they can compensate with their average resulting to be low. On the other hand, the E_{MAX} exactly identifies which is the maximum prediction error for each profile. The probability density functions (PDFs) for E_{MAX} are shown in Figure 3.17,a. They are obtained over 6300 test points (900 each for all 7 input powers). The obtained mean E_{MAX} for gain and NF are 0.16 and 0.15 db, respectively. The standard deviation of E_{MAX} for gain is $\pm$0.09 dB, and that for NF is $\pm$0.07 dB. These values indicate a high accuracy of predictions using just a single NN model, particularly considering the large input power dynamic range of the BDFA and its gain and NF nonlinear behaviour for both pump and input signal powers variations. Figure 3.17,b presents the target and predicted profiles for the worst gain and NF predictions. The overall prediction and target profiles have an excellent match, demonstrating that even the worst cases show a good correspondence with the actual performance.

The developed NN model trained with the discrete data set is also tested using the data set with uniformly distributed input total signal power values (the Case 2 in Table 3.1). In this case the training data set is identical to the data set in the Case 1, and, thus, parameters obtained in the k-fold validation are the same as in the Case 1. The testing data set consists of 2700 points and is based on P_{in}, I_b and I_f values being uniformly distributed in the range of $[-25:5]$ dBm for P_{in} and $[200:1000]$ mA for pump currents (in a log scale). The probability density functions for gain and NF are shown in Figure 3.17,c. The obtained E_{MAX} for gain and NF is equal 0.76 dB and 0.69 dB and error deviations are $\pm$0.39 dB and $\pm$0.32 dB, respectively. The worst predictions of gain and NF are presented in Figure 3.17,d. Even though the achieved results have a worse performance than the model predicting the behaviour of signals with power levels presented in the training data set, it shows an acceptable performance for the numerical obtainment of gain and NF profiles. This performance degradation can be predominantly explained by the presence of the testing data set data points which are located between the data points in the training data set (i.e. -22.32 dBm in testing data set when in training data set only -25 dBm and - 20 dBm point existed).

As the next step, the developed NN model is trained and tested using a data set with uniformly distributed total input signal power values in the range of $[-25:5]$ dBm (Case 3 in Table 3.1). The pump currents I_b and I_f are uniformly distributed (also in a log scale) as well in the range $[200:1000]$ mA. This model considers a total of $N = 9000$ data points. The k-fold cross validation results are $N_{HN} = 600$, $f_{act} = sin(x)$, $\lambda = 10^{-10}$, and $\sigma = 10^{-2.5}$. The probability density functions (PDFs) for E_{MAX} are shown in Figure 3.18,e. The obtained mean E_{MAX} demonstrates a high accuracy of predictions with 0.19 dB for gain and 0.16 dB for NF. The standard deviations are 0.09 dB and 0.07 dB for gain and NF predictions,

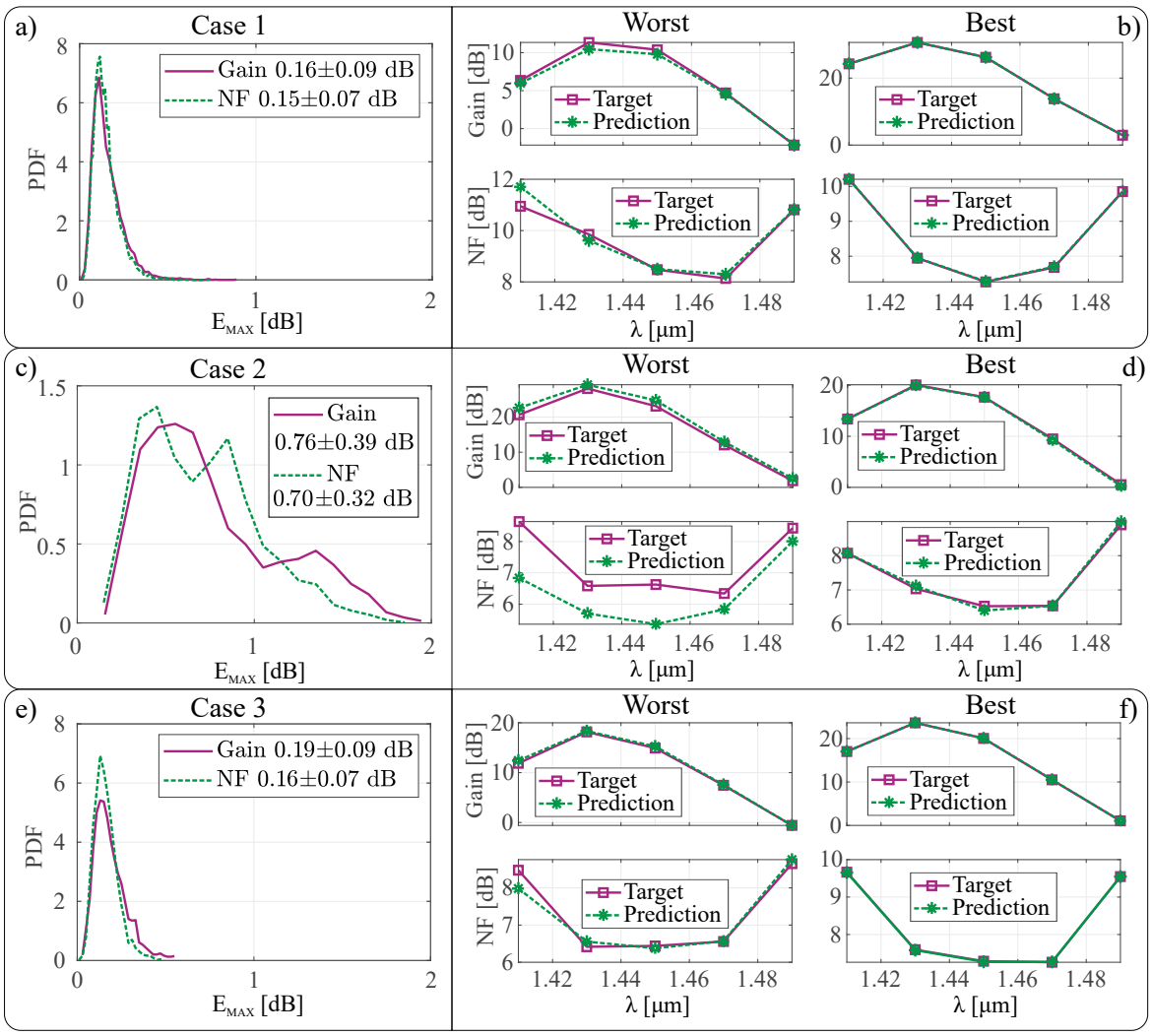

Fig. 3.17 Probability density functions (PDFs) for gain and NF predictions for a) Case 1; c) Case 2; e) Case 3; the worst gain and NF predictions for b) Case 1; d) Case 2; f) Case 3.

respectively. Figure 3.17.e presents the target and predicted profiles for the worst predictions for gain and NF.

Finally, the performance of the proposed framework in all three different cases is tested with different training data set sizes. The dependency of E_{MAX} for gain and NF on the training data set size is presented in Figure 3.18. The discrete model for both testing data sets (the curves 1 and 2 in Figure 3.18) behaves similarly with an almost minimally possible performance around 6500 data set points. In contrast, the smallest data set (around 2000 points) is required to completely train the model with randomly distributed total input signal power values (curve 3 in Figure 3.18). The worst performance of Case 3 achieved with 450 data points is comparable to that achieved in the Case 2 with maximum number of data

points. The achieved results show that a data set size increase for all cases will not improve the performance of the proposed framework gain and NF predictions. Using a data set with randomly distributed total input signal power values for the training significantly increases the accuracy of amplification predictions for any input signal powers in the range of the training data set. It also allows to decrease the size of the data set size required for training. The relatively small data set size of Case 3 required for training can not only decrease the time of the data set acquisition but also allow using such a model in cases when an automatic data acquisition is challenging or impossible.

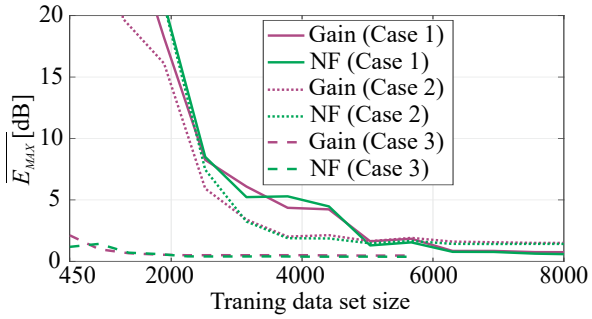

Fig. 3.18 Maximum absolute error E_{MAX} of gain and NF predictions as a function of training data set size for three different modelling cases indicated in brackets.

The demonstrated NN-based framework trained purely with the experimental measurements showed high accuracy for the prediction of both BDFA gain and NF for five signal channels in the 1410-1490 nm wavelength range. The proposed model was trained and tested using two different experimentally acquired data sets based on the grid and randomly distributed signal power values. The results indicate that using a data set with randomly distributed signal power values is preferable for the prediction of the signal amplification with any initial power values in the range of the training data set. Another advantage of such data set is the relatively small number of data points required for the framework training. The predicted BDFA performance shows a good agreement with experimental results of the signal amplification in both linear and saturation regimes, confirming that the proposed NN-based framework can be used for BDFA optimisation. The proposed NN-based model is a versatile and reliable tool that can potentially be used for the BDFA control for both in-line and booster applications and the signal power profile optimisation.

Chapter 4

Development of Bi-doped fibre amplifiers

In this chapter, the methodology of BDFAs main parameters measurements are considered including manual and automatised techniques for gain, NF, and PCE measurements. Three amplifiers based on three different fibres are developed and characterised. The impact of different pumping wavelengths is presented and discussed. The main ways for BDFA design optimisation are discussed.

4.1 Main parameters of optical amplifiers and methods of their measurement

To determine what the main parameters of the optical amplifier are, it is important to determine what is an optical amplifier. An optical amplifier is a device that amplifies light directly without converting it to electrical signal and back. Fibre loss has to be compensated in the communication lines designed to operate over 100 km because optical loss is a cumulative effect that leads to the signal eventually becoming too weak for it to be recovered by the receiver [1]. As the main purpose of the optical amplifier is to recover the optical signal power, the optical gain is one of the main merits of optical amplifiers. If we consider an amplifier as a black box, then if the signal has an incident signal power of P_s^{in}, then the signal power at the output from the optical amplifier is P_s^{out}. The optical gain then can be determined as a relation between the output signal power and the input signal power :

$$g = 10log_{10}(\frac{P_s^{out}}{P_s^{in}}). \tag{4.1}$$

Most commonly, optical gain is represented in decibels, thus, the relation between the output signal power and the input signal power should be under decimal logarithm and the

result should be multiplied by ten. However, the optical gain is not the only merit for the quality of the optical amplifier. Another important parameter is power conversion efficiency (PCE). PCE most commonly describes the efficiency of the pump radiation to be converted into the increase of the signal power. Thus, PCE is an analogue of the commonly known coefficient of performance, or COP, but for optical system. Based on the definition, the equation for PCE can be represented in the following form:

$$PCE = \frac{P_s^{out} - P_s^{in}}{P_p^t}, \tag{4.2}$$

where P_p^t is the total pump power.

In addition to providing optical amplification, optical amplifiers also add undesired optical power fluctuations to the signal. This intensity noise can lead to impossibility of the signal reception by optical receivers. In optical amplifiers, it is common to use noise figure (NF) to quantify the effects of noise. The noise introduced by optical amplifiers can be characterised by the optical spectrum and using an appropriate model to evaluate the intensity noise. The most common cause of optical noise (especially in doped-fibre amplifiers) is amplified spontaneous emission (ASE), however, there are other noise sources that should sometimes be considered [109]. In the case of BDFA, the key noise source is always ASE. In the simplest formulation, NF can be determined as follows [111]:

$$NF = 10log_{10}F = 10log_{10}\frac{inputSNR}{outputSNR}, \tag{4.3}$$

where F is the noise factor determined as the relation between input signal-to-noise ratio (SNR) to the output SNR. NF represents how much additional noise is introduced in the amplifier in comparison to the theoretical limit. There are several methods of NF measurements, however, the most commonly used one is the optical method. This method is also called source substraction technique [109]. In the context of the optical method, NF can be represented as a relation of the minimal theoretical noise level and real noise spectral power density:

$$NF(\lambda) = 10\log_{10}(\frac{\rho_{noise}(\lambda)}{G(\lambda)h\nu} + \frac{1}{G(\lambda)} - \frac{\rho_{sse}}{h\nu}), \tag{4.4}$$

where ρ_{noise} and ρ_{sse} are the unpolarised noise spectral density on the output of the amplifier and unpolarised noise spectral density of the input signal, h is the Planck constant, and ν is the photon frequency at the signal wavelength. As the signal-to-noise ratio of the input signal is usually higher than 50 dB, when the amplifier is characterised with just TL (all measurements presented in this Chapter are performed using a TL with 80 dB SNR), the input noise contribution is negligible. However, it is important to note that, while characterising

the performance of the amplifiers in the optical line, the SNR of the input signal is typically higher than 50 dB, thus, the last term cannot be neglected. At last, usually the gain bandwidth is also distinguished as a separate parameter of the optical amplifier. Most commonly, the bandwidth of the optical gain is determined at the level of -3 dB from maximum value unless stated otherwise. As the next step, the methods of all parameters measurement should be described.

4.1.1 Manual amplifier characterisation technique

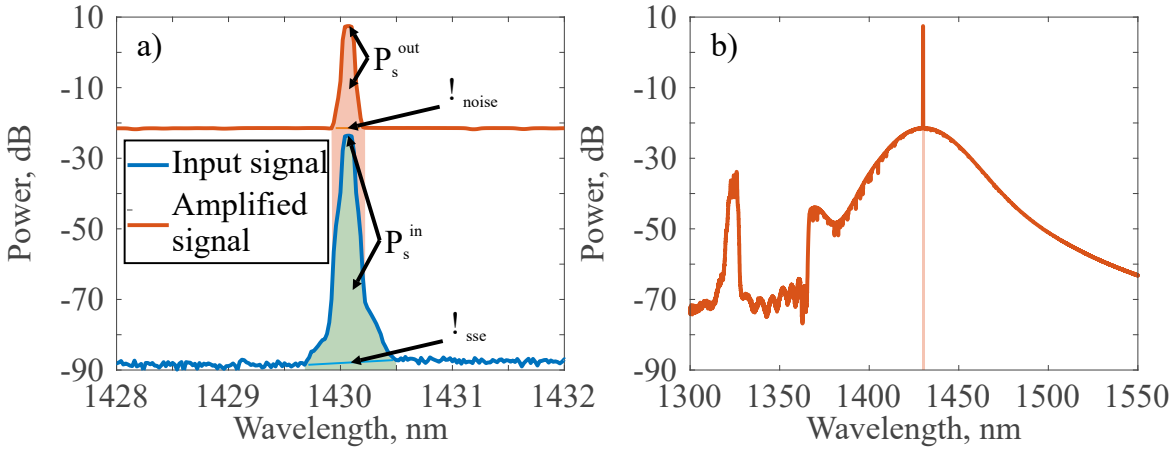

Fig. 4.1 a) The spectra of signal before (blue line) and after (red line) amplifier; b) full spectra of the output signal including unabsorbed pump and ASE

First, the manual characterisation of the optical amplifier is considered and it is the basis for setup automation which is presented in the next subsection. To begin with, two methods of gain measurement should be discussed. The spectra of signal before (blue line) and after (red line) amplifier are presented in Figure 4.1,a. The easiest way to determine gain is the difference between the peak values of the input signal and the amplified signal. These two points are indicated in Figure 4.1,a as P_s^{in} and P_s^{out} and the two arrows of each indicator show the peak value of the signal. However, in some cases a different approach can be applied to determine gain by measuring the power concentrated in the peak of the signal. The area that corresponds to the signal is indicated as red area for the output signal, and green area for the input signal. However, there are two notes that should be made. Firstly, it can be seen that all signal power on the input to the amplifier is predominantly concentrated in the main peak at 1430 nm. However, for the signal at the output of the amplifier the other spectral part should be considered and a fraction of the spectrum associated with the signal to the full optical spectrum should be calculated for the correct evaluation of the output power

of the signal. Importance of this can be seen in Figure 4.1,b. One can see that except the main signal optical spectrum also contains unabsorbed pump power (around 1330 nm) and a significant ASE noise in the spectral band of 1370-1550 nm.

As the next step, a way to determine the spectral density of the noise and spectral density of the input signal should be discussed. Usually, they are determined from the optical spectrum by interpolating the noise in vicinity of the signal to the wavelength of the signal: blue and orange lines below the signal in Figure 4.1,a, respectively. However, determination of this level is not enough for the correct measurement: it should also be derived by the correct value of the measurement bandwidth (usually determined by the slit of the monochromator of OSA). Moreover, the signal power should be corrected in regards to the total power measured by the PM. More details on this correction is presented in the discussion of the measurement techniques of NF and gain. To determine PCE it is enough to measure output power along with input power if the I-W curve for the pump laser diodes has been recorded prior to the measurement.

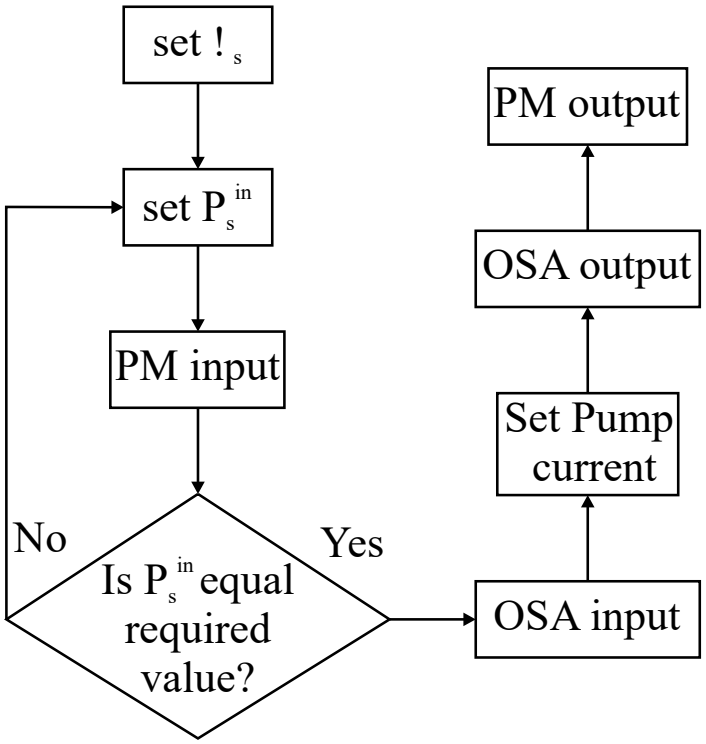

Fig. 4.2 Block diagram of the amplifier performance measurement required for determination of gain, PCE, and NF

Let us consider a simple manual measurement procedure of all the characteristics necessary for determination of gain, NF, and PCE. The block diagram of the measurement is presented in Figure 4.2. As the first step, the wavelength of the signal λ_s should be tuned

by TL. Then, the power of the signal power P_s^{in} should be adjusted with a variable optical attenuator VOA and measured with a PM. In case then that the P_s^{in} is not equal the required value, the VOA should be further adjusted by the difference between the measured value and the required one. If the P_s^{in} is equal the required value, the optical spectrum of the signal should be recorded. After that, the input signal should be connected to the input of the amplifier and the required pump current should be set with regards to the measured I-W curve of the pump laser diode to obtain the desired pump power. After that, the signal at the output of the amplifier should be recorded with OSA and PM to determine the optical spectrum and power of the signal.

After all the data is recorded, it can be analysed to obtain the Gain, NF, and PCE. As the first step, peak-to-peak gain can be easily determined as a difference between peak values of the output and input signal and equation 4.1. PCE is usually also easily determined using equation 4.2 as all necessary values are recorded. In terms of NF, if one refers to equation 4.3, one can see that ρ_{sse} is negligible, and the only unknown parameter is ρ_{noise}. To determine it correctly, the power spectral density of the output signal recorded by OSA should be calibrated in regards to the measured output power. For that the output spectrum recorded in full with unabsorbed pump and all ASE should be integrated. The correction factor is obtained as a relation between this integral and the total output power. The calculated ρ_{noise} should be multiplied by this correction to determine the real value of the noise spectral density.

4.1.2 Automatic amplifier characterisation technique

In this subsection the setup of the automatic measurement of the main amplifier parameters is considered. Figure 4.3 shows the schematic of the experimental setup of an automatic amplifier characterisation. The experimental setup consists of all the components that can be controlled by PC (MATLAB code). The details of the code is not shared in this thesis as it is only compatible with very specific equipment and the setup developed at AiPT. However, parts of the code can be shared upon reasonable request. The first element of the setup is TL, that operates in the wavelength range from 1355-1485 nm. The power of the TL is kept constant with the wavelength sweep, and an external VOA is used to control signal power at the input to the the amplifier. To correctly set the signal power, a PM is used after the 30/70 coupler that in combination with the characterised splitting spectra of the coupler can measure the real value of the signal at the input to the amplifier. The splitting spectra is required as the fused couplers are usually intended to work in quite narrow spectral bandwidth (around 40 nm), and the coupler used in the experiment is intended to be used in vicinity of 1550 nm.

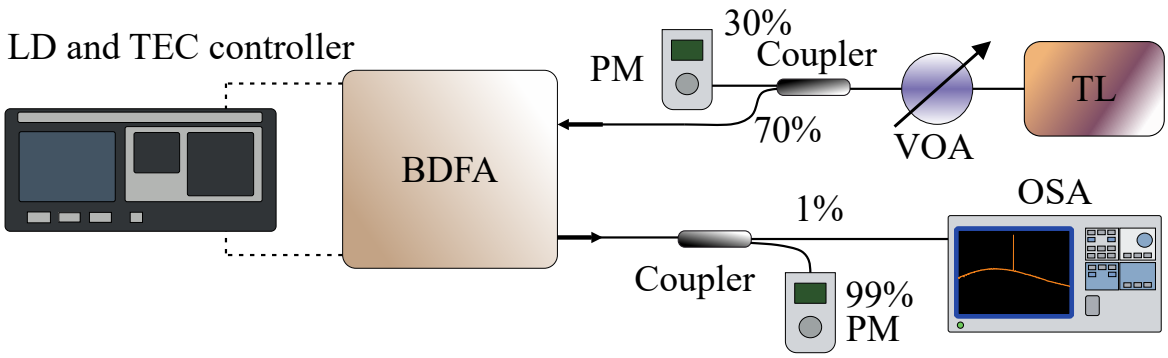

Fig. 4.3 Schematic of the automatic measurement setup for amplifier characterisation

After the input signal power is correctly calibrated, the signal radiation is directed into the BDFA which is controlled by LD and TEC controller. The temperature of the diodes is kept constant at 20°C, and the LD current can be specified in regards to the I-W curves of the LD recorded prior to the experiment. After the signal is amplified, it is split by a 99/1 coupler which ratio is also recorded prior to the experiment. After the signal is split, a 99% portion is recorded by PM, and 1% is received by OSA. After all the necessary data is recorded, it can be used to obtain main amplifier parameters: gain, NF, and PCE. The details of this analysis is presented in the previous section.

Finally the measurement error of the proposed technique should be estimated. It can be assumed that the error induced by the method has a normal distribution for gain in linear scale, and NF in linear scale (more commonly known as noise factor). With that in mind, a set of 100 consecutive measurements containing the data set of parameters required for obtaining main amplifier parameters at six wavelengths, two pump power data points, and three input signal powers was obtained. The data set was carefully observed to exclude the data set with systematic errors (i.e. failure to set the correct input signal power). The resulting number of correctly measured data sets was 88. As the next step standard deviation σ has been obtained over 88 points for each value of wavelength, signal power and pump power. After that the standard deviation for values in dB were obtained using the following equations:

$$\sigma_{pos}^{dB} = 10log_{10}(S_{mean} + \sigma) - 10log_{10}(S_{mean}), \tag{4.5}$$

$$\sigma_{neg}^{dB} = 10log_{10}(S_{mean}) - 10log_{10}(S_{mean} - \sigma), \tag{4.6}$$

where S_{mean} is the mean value of the linear variables (linear gain and noise factor), *sigma* is the standard deviation of the variable, σ_{pos}^{dB} is the standard deviation in decibels for distri-

bution above the mean value, and σ_{neg}^{dB} is the standard deviation in decibels the mean value. It has been noticed that the standard deviation for all wavelengths are different, however, they change negligibly with the variations of pump power and input signal power. Moreover, the difference between the σ_{neg}^{dB} and σ_{pos}^{dB} is negligible, thus the mean standard deviation was used. Figure 4.4 shows the dependence of the two standard deviations (corresponding to the 95% of the values) for gain and NF for all measured wavelengths.

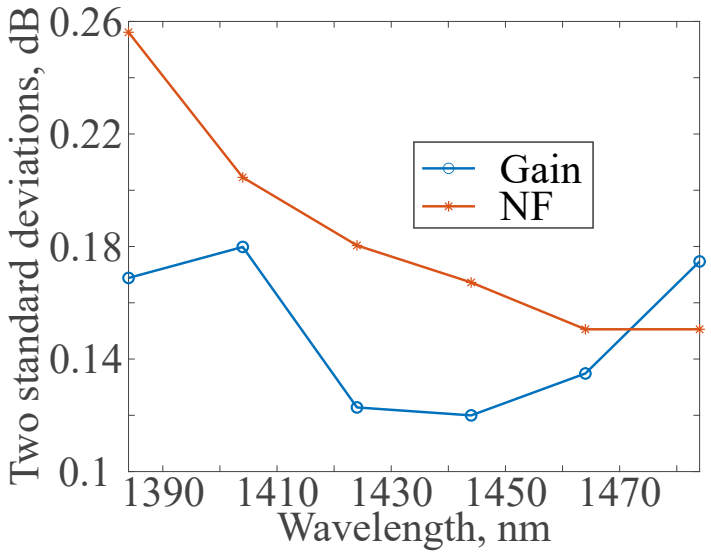

Fig. 4.4 Spectra of the two standard deviations for gain and NF measurements.

It should be noted, that two standard deviations for NF are generally worse than that for Gain, due to a more complex nature of the NF calculation, including more varying parameters. While talking about the maximum gain, the gain in vicinity of 1430-1440 nm is usually assumed, where gain gas two standard deviations of 0.12 dB. Thus, it can be assumed that the real value of the maximum gain can be obtained with an error of ± 0.12 dB. The minima of NF is typically lying in the vicinity of 1460-1470 nm where two standard deviations are around 0.15 dB. Thus, the measurement of the minimal NF can be made with ± 0.15 dB precision. The precision of gain and NF presented in this thesis can be verified using Figure 4.4.

4.1.3 Amplifier components measurements

Active fibre is no doubt the most crucial part of doped-fibre amplifiers. However, passive components also play a crucial role in the overal performance of the amplifier. Thus, in this subsection the main passive components characteristics are be presented. All three amplifiers were made using the set of similar components with almost equal characteristics. Thus, only

the parameters for the passive components of the BDFA-1 are presented in this subsection. To begin with, the signal line consists of two TFF-WDMs and two signal isolators. The measured insertion loss of isolators is presented in Figure 4.5.

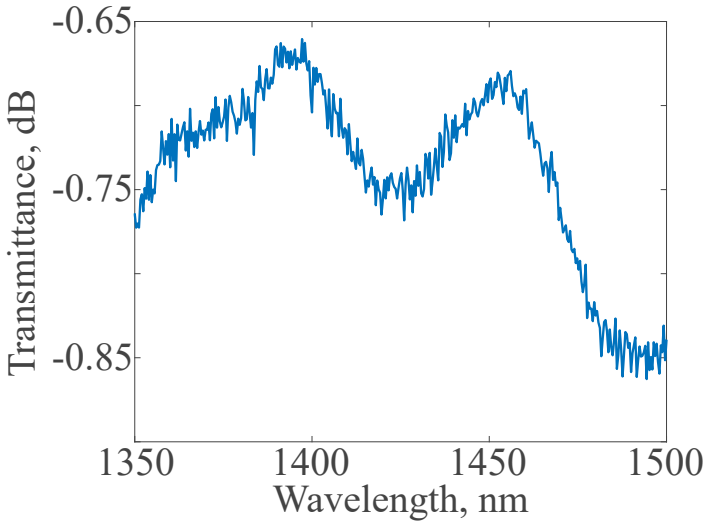

Fig. 4.5 Experimentally measured transmittance of the signal isolator.

The isolator features very low variations of the insertion loss almost in the whole operation band. The average insertion loss are 0.7 dB. after about 1470 nm the insertion loss increase rapidly up to 0.85 dB. At the next step the transmittance and reflectance of the TFF-WDM are presented in Figure 4.6.

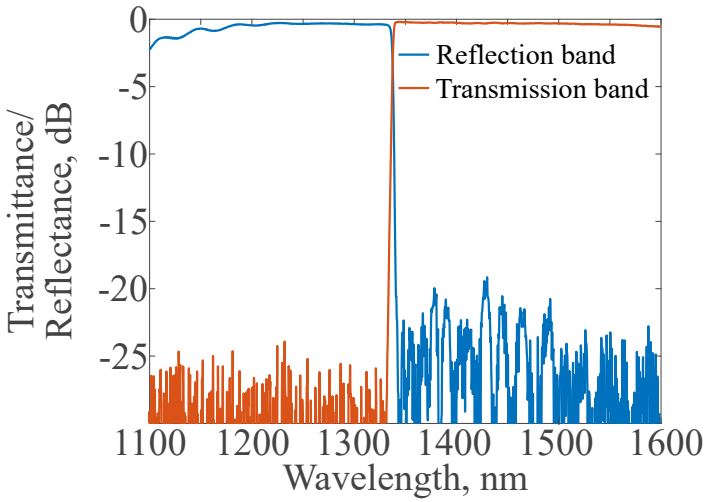

Fig. 4.6 Experimentally measured transmittance and reflectance of the TFF-WDM.

The TFF-WDM features very flat transmission and reflection bands. The transmission band is utilised by the signal and the reflection band is used for the pump radiation. The

maximum loss of the pump is 0.38 dB in the utilised bandwidth and the maximum loss of the signal in utilised band is 0.32 dB. In addition to the passive component measurements, the splice loss between SMF and BDF was measured to be 0.1 dB. As the power of the pump lasers was measured after the isolators, their characteristics are not presented here. Thus, the pump radiation is only affected by a single TFF-WDM for both forward and backward pump lasers.

4.2 BDFA based on 9μm core diameter fibre

As the first step, a BDFA based on low-germanosilicate fibre with 9 μm core diameter and 125 μm cladding diameter was developed. The choice of 9 μm core diameter was predominantly determined by the geometry of SMF. Similar geometry of active fibre and fibre of passive components allows to minimise potential splice loss. The fibre was fabricated in the Dianov Fiber Optics Research Center using the MCVD-solution[76]. The composition of the fibre core is as follows: 95 mol% SiO2, 5 mol% GeO2 and <0.01 mol% of bismuth. The NA of the fibre is 0.14, and the cutoff wavelength is around 1.2 μm. The spectral properties of the fibre are similar to the one reported in [69, 76]

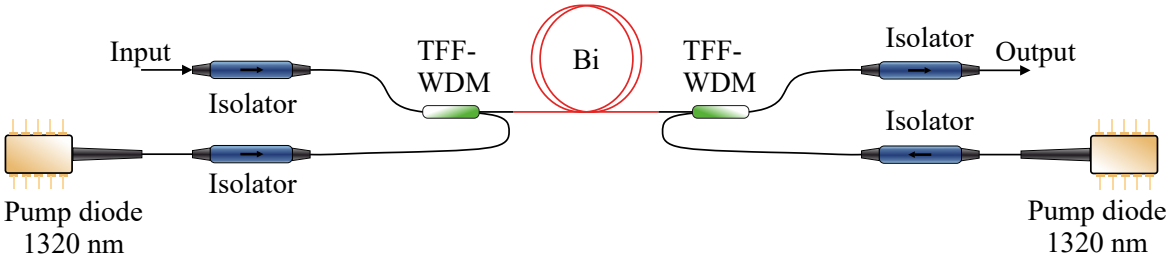

Fig. 4.7 Scheme of the bismuth-doped fibre amplifier based on 9 μm core diameter. TFF-WDM: thin film filter wavelength division multiplexer; Bi: Bi-doped fibre.

The developed Bi-doped fibre amplifier is based on a 320 m long piece of active fibre and its experimental setup is presented in Figure 4.7. The signal passes the optical isolator with minimum isolation of 32 dB and internal loss less than 3 dB operating in spectral band of 1390-1490 nm. After the isolator, the signal is coupled into Bi-doped fibre through TFF-WDM. The radiation of the forward pump laser diode operating at the wavelength of 1320 nm passes 1320 nm optical isolators and is coupled into the active fibre through TFF-WDMs. After a subsequent amplification in the Bi-doped fibre, signal radiation passes another TFF-WDM and another 1390-1490 nm optical isolator. Another 1320 nm pump laser diode used for backward pumping is coupled into the amplifier using the output TFF-WDM.

The developed BDFA was previously presented in our paper published in Optics Materials Express [63] and here we will present similar results achieved in this amplifier. All three pumping schemes are presented below, however, as a first step, the forward pumping scheme is described. The developed BDFA is also characterised with three different input signal levels of -20 dBm, -10 dBm, and 0 dBm. The gain and NF for the forward pumping scheme and three different signal levels are presented in Figure 4.8. The spectra are measured with an increment of 5 nm.

The gain significantly rises with the pump power increase and saturates at high pump powers (after 324 mW) for all signal power levels that can be seen in Figure 4.8 (a,c,e). The maximum gain is 30.4 dB and achieved at the wavelength of 1430 nm, 470 mW pump power and -20 dBm signal power. The gain spectrum significantly flattens with the increase of signal power, leading to an almost double increase in 3dB gain bandwidth from 27.3 for -20 dBm input signal power to 52.1 nm for 0 dBm input signal power. Moreover, an increase of the input signal power leads to consistent maximum gain reduction from 30.4 dB to 18.6 dB for -20 dBm and 0 dBm input signal power, respectively. This dynamic also causes a significant increase of the minimal NF value from 4.8 dB to 5.6 dB.

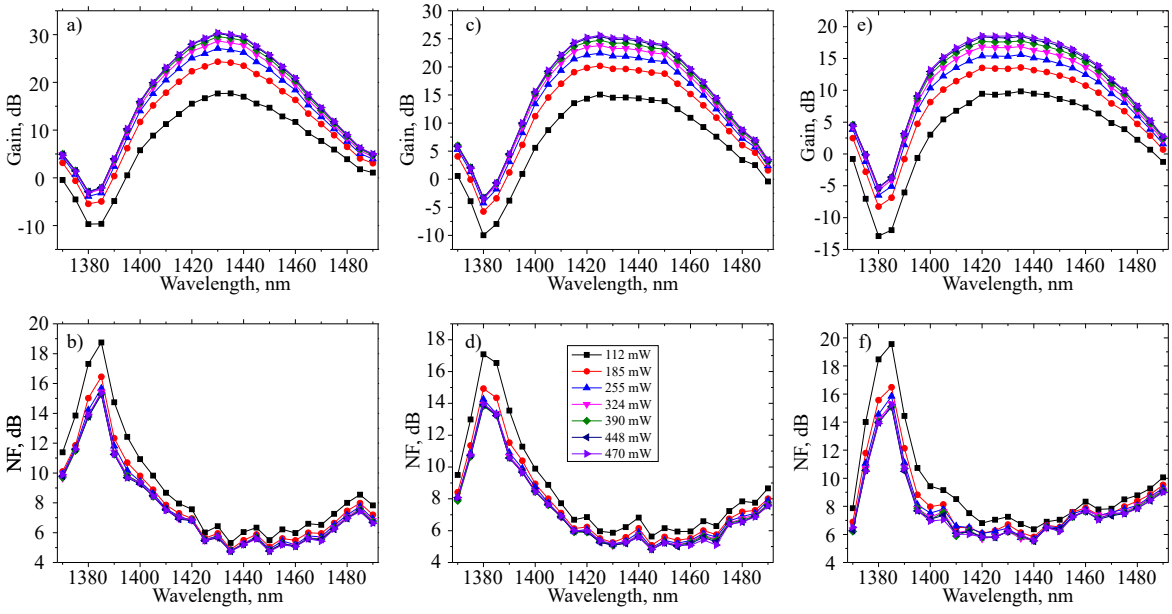

Fig. 4.8 Spectral dependencies of the measured gain (upper row) and the noise figure (bottom row) for different pump powers in a forward pumping scheme: a,b) gain, NF for -20 dBm input signal power; c,d) gain, NF for -10 dBm input signal power; e,f) gain, NF for 0 dBm input signal power.

The measured NF spectra for all three input signal powers and pump powers are shown in Figure 4.8 (b,d,e). The NF decreases with the increase of the pump power and saturates even more dramatically than the gain. The significant increase of NF closer to 1390 nm corresponds to the amplification at the edge of the gain band and the water absorption peak located around 1380 nm. This region also features increased loss of the optical isolators. The amplification at the 1370 nm occurs due to stimulated emission from the pump level and leads to improved NF and gain performance in comparison to the signal amplification between 1370 and 1390 nm. The amplification beyond the presented spectral band was not possible due to the limitations of the TFF-WDM reflection band starting from 1370 nm. The minimal achieved NF is 4.8 dB for - 20 dBm signal at the 1435 nm wavelength and 470 mW of the pump power. The comparison between the gain, the 3 dB gain bandwidth, and the NF for all pumping schemes are presented in Table 4.1.

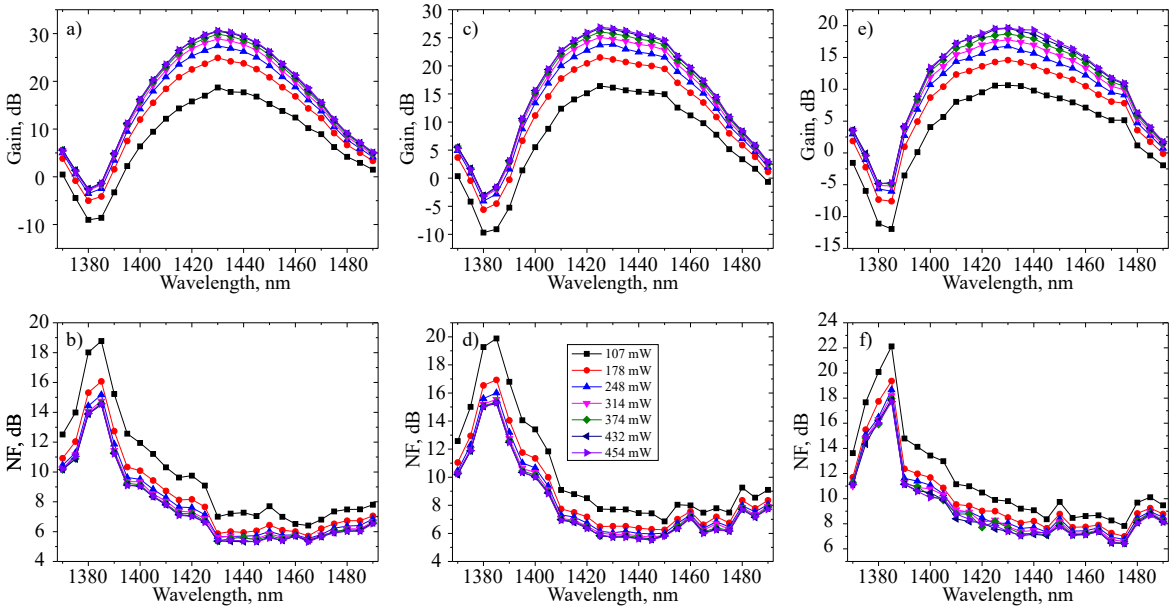

Fig. 4.9 Spectral dependencies of the measured gain (upper row) and the noise figure (bottom row) for different pump powers in a backward pumping scheme: a,b) gain, NF for -20 dBm input signal power; c,d) gain, NF for -10 dBm input signal power; e,f) gain, NF for 0 dBm input signal power.

As the next step, the backward pumping scheme is investigated with all three signal powers and similar pump powers. It is important to note that the measurements presented in this section feature different pump powers for different pumping schemes as the pump laser diodes were initially controlled to have the same controller current, but not the same output power. This problem will be addressed later in this section and in section 4.4. The

gain and NF spectra behave similarly to the backward pumping scheme, with the overall slightly higher gain and lower NF (Figure 4.9).

The maximum gain is equal 30.6 dB and located at 1430 nm at pump power of 454 mW and -20 dBm input signal power. The maximum gain bandwidth for -20 dBm is wider than that of the forward pumping scheme and features 29 nm. However, its value for 0 dBm input signal power is also narrower than that of the backward pumping scheme and is equal to 44.9 nm. The minimal NF is the highest of all pumping schemes and is 5.3 dB for -20 dBm input signal power at the wavelength of 1430 nm and the pump power of 454 mW. The observed higher NF level in comparison to the forward pumping scheme is expected for the non-uniformly pumped active fibre [112]. This happens due to predominant amplification of the signal rather than spontaneous emission leading to the lower levels of ASE for the forward pumping scheme.

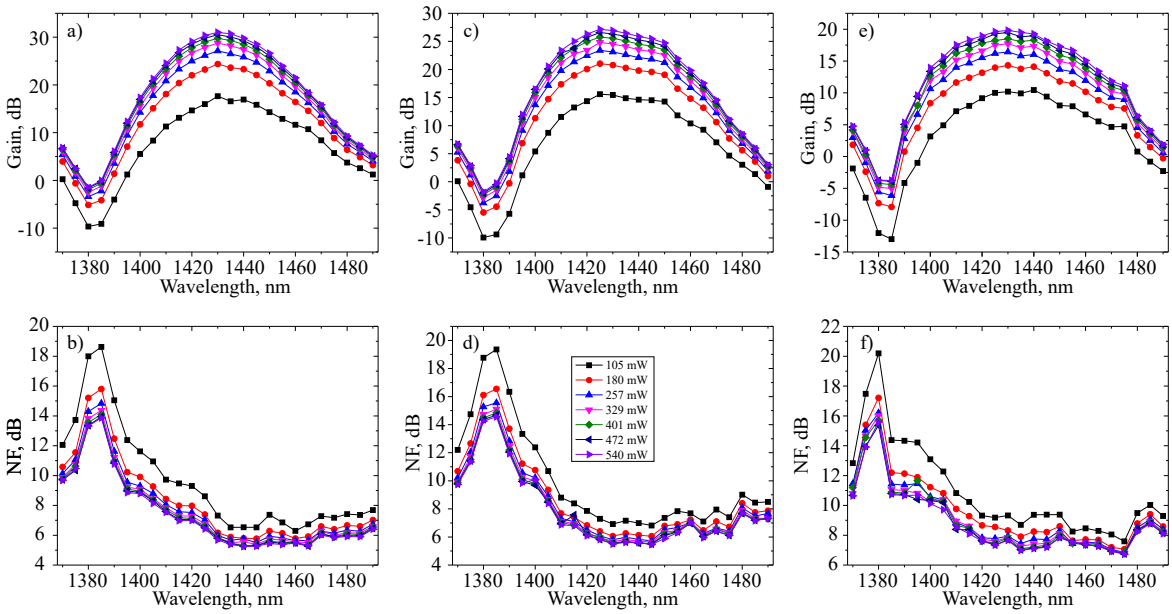

Fig. 4.10 Spectral dependencies of the measured gain (upper row) and the noise figure (bottom row) for different pump powers in a bi-directional pumping scheme: a,b) gain, NF for -20 dBm input signal power; c,d) gain, NF for -10 dBm input signal power; e,f) gain, NF for 0 dBm input signal power.

As the last step, similar results are presented for the bi-directional pumping scheme i.e., spectral dependencies of the gain and NF for various signal and pump powers (Figure 4.10). The total pump power of the diodes with equal power in both directions is indicated in Figure 4.10. As the maximum pump power of the bi-directional pumping scheme is significantly

higher than those of other pumping schemes, the maximum value of gain and gain bandwidth, and minimum value of NF are compared at similar power of 472 mW (dark blue line with arrows in Figure 4.10).

The maximum gain for the -20 dBm signal power is equal 30.5 dB for the pump power of 472 mW and the gain peak is again at 1430 nm. The maximum gain bandwidth of 29.1 for -20 dBm is the widest compared to those of other pumping schemes. However, in the case of 0 dBm signal it is also narrower than that of the backward pumping scheme and is equal 42.9 nm. The minimal achieved NF is 5.3 dB for -20 dBm signal power at a total pump power of 472 mW, which is a slightly better value than that of the backward pumping scheme.

Table 4.1 Parameters of the amplifier with different pumping schemes and signal powers. For forward pumping scheme the pump power is 470 mW, for backward pumping scheme - 454 mW , and for bi-directional pumping scheme - 472 mW.

Signal power	Pumping scheme	Gain, db	Bandwidth, nm	NF, db
-20 dBm	forward	30.4	27.3	4.8
	backward	30.6	29	5.3
	bi-directional	30.5	29.1	5.3
-10 dBm	forward	25.6	42.4	4.8
	backward	26.9	38.2	5.5
	bi-directional	26.6	37.1	5.5
0 dBm	forward	18.6	52.1	5.6
	backward	19.6	44.9	6.4
	bi-directional	19.5	42.9	7

As mentioned previously, the performance of the developed amplifier is recorded for different pumping schemes with slightly different pump powers. Thus, here it is important to compare the power dependencies of gain and NF. As both optical gain and NF have also a spectral dependence, we averaged the values of these parameters in the range of 1400-1480 nm for - 20 dB input signal power in order to compare an average performance of the pumping schemes. Such dependencies for forward, backward and bi-directional pumping scheme are presented in Figure 4.11.

The graphs show that, for almost all pump powers, the highest gain is achieved in the backward pumping scheme. The bi-directional pumping scheme shows intermediate gain (between forward and backward pumping schemes). The forward pumping scheme demonstrates slightly lower optical gain as compared to other pumping schemes. However, the forward pumping scheme allows to achieve the best NF in the whole operating region. The NF curves for bi-directional and backward pumping schemes are almost the same with slightly better performance of the bi-directional scheme for pump powers less than 200 mW. Thus, the pumping uniformity plays a crucial role for the amplifier performance in terms of

the NF. It is worth noting that the NF for the forward pumping shows a noticeable saturation with the pump power as compared to the bi-directional and backward pumping schemes. This indicates that even a slight increase of pump power (100mW) for the bi-directional and backward pumping schemes will lead to comparable NF performance to that of the forward pumping scheme. Similar performance but in terms of gain saturation is observed in the backward pumping scheme. Therefore, it is preferable to use the forward pumping scheme in order to achieve a moderate gain and an excellent NF with a relatively low pump power. Obviously, NF and gain should be nearly the same for all pumping schemes when the gain medium is well and uniformly pumped.

The measured PCEs for the three different pumping schemes are as follows: 15.3% for the forward pumping scheme, 16.3% for the bi-directional pumping scheme, and 19.8% for the backward pumping scheme. The PCE of around 20% is the typical value for L-band EDFAs[113], and is lower than that of C-band EDFAs with more than 33% PCE. The further increase of the PCE can be performed by using fibre Bragg gratings [114], double pass configuration [115], or by shifting the pump wavelength closer to the absorption maximum. The maximum output signal power exceeds 100 mW. Although the developed amplifier characteristics are already sufficient for application in practice, further scalability is anticipated, since >50% lasing efficiency with >10-W output power have already been reported [116].

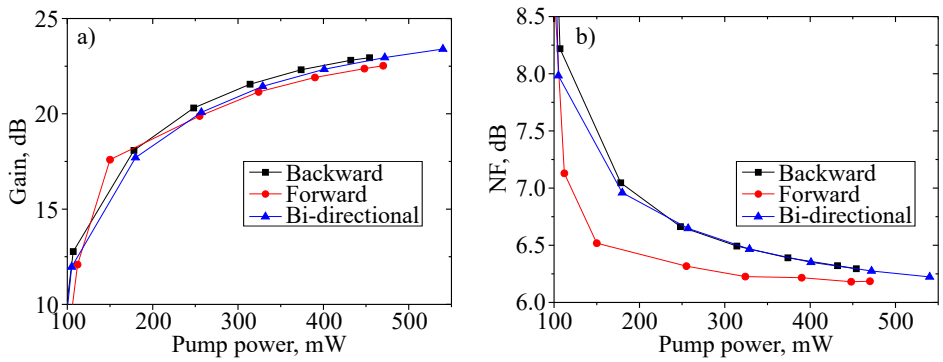

Fig. 4.11 Dependencies of the gain (a) and NF (b) on the pump power for three different pumping schemes averaged over the spectral band of 1400-1480 nm for - 20 dB input signal power

The current results presented here show a certain overall increase in the performance of BDFA, i.e. the increase of the maximum gain (or the minimum NF) in comparison to the previous works published at Aston with 27.8 dB gain and 7.4 dB NF [93], and 27.9 dB gain and 5 dB NF [117]. The key change that allowed to achieve better performance is the use of TFF-WDM in comparison to the fused WDMs used in both works. Moreover, the

NF measurement was optimised between the work [93] and the work [117] that allowed to find a mistake in NF calculation in the work [93]. In this section, the left part of the gain spectrum showed a continuous growth; however, a detailed study of this part will be presented in section 4.4 where different bismuth doped-fibres will be tested in the same passive components setup with wider TFF-WDM transmission bandwidth and different pump wavelengths.

4.3 BDFA based on 6μm core diameter fibre

In this section, two different BDFAs based on geometrically similar fibres are considered. Even though the passive components of the setup are almost identical, and the geometry of the developed fibres is the same, the preforms in both cases are different. Thus, it is important to consider both fibres and highlight the differences.

4.3.1 Fibre from preform 1

Let us consider the first amplifier. The schematic of the bismuth-doped fibre amplifier is presented in Figure 4.12. The developed amplifier consists of TFF-WDMs used for multiplexing and demultiplexing of radiation at pump (1250-1320 nm) and signal (1330-1500 nm) wavelengths. The TFF-WDMs have very steep and flat transmission and reflection bands that allow to achieve consistent loss over the whole operation bandwidth. Two isolators centred at 1320 nm were used to avoid back reflection of radiation to the pump diodes, and two 1440 nm isolators were used for unidirectional transmission of the signal. Two LD and TEC controllers were used to control temperature and output power of the pump laser diodes. The Bi-doped germanosicilcate fibre used in this work is fabricated in-house using the conventional MCVD-solution doping technique and has the length of 173 m in FORC. The fibre has a 6 μm core diameter and 125 μm cladding diameter. The refractive index difference (Δn) between the core and cladding is around 0.004. The fibre core consists of 95 mol% SiO_2, 5 mol% GeO_2 and <0.01 mol% of bismuth. The cutoff wavelength (λ_c) of the fibre is measured to be around 1000 nm.

As the first step, the performance of the developed BDFA for bi-directional pumping scheme and seven different signal powers in the range from -25 to 5 dBm with a step of 5 dB is characterised. Figure 4.3.1 shows recorded spectra of the gain for all seven input signal powers and 1 W total pump power equally split between forward and backward pump lasers. The amplifier features maximum gain of 39.8 dB for -25 dBm input signal power. The maximum gain substantially decreases to 20.8 dB with the increase of the input signal to

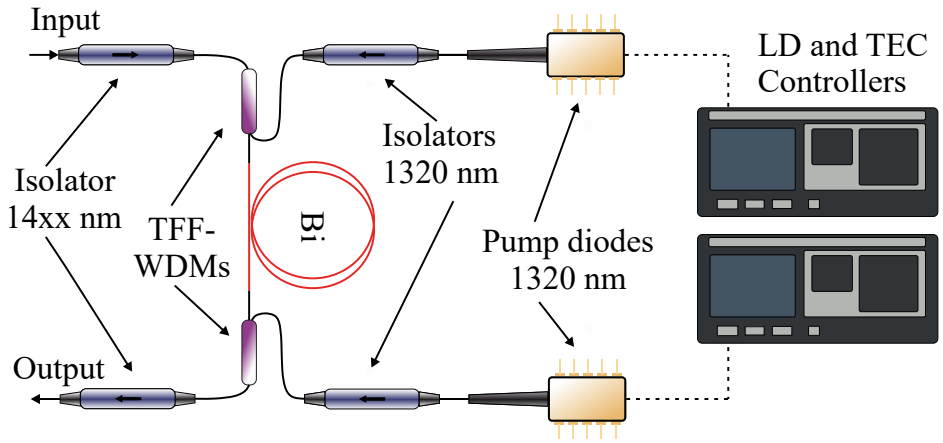

Fig. 4.12 a) Schematic of BDFA based on 6 μm core diameter fibre fabricated from preform 1 and preform 2.

5 dBm. On the other hand, the 3 dB bandwidth of the gain rises with the increase of the input signal from 30.9 nm to 73.6 nm for -25 dBm and 5 dBm input signal powers, respectively. The main recorded characteristics of the bi-directional scheme for different input signal powers are presented in Table 4.2. Figure 4.3.1,b shows the spectra of NF for seven different input power signals. The minimal NF of 4.6 dB is achieved with -25 dBm pump at 1468 nm. The NF rises up to 5.3 dB with the increase of the input signal power to 5 dBm. The NF has a predominantly linear trend with the wavelength, substantially decreasing from the left hand side to the right hand side. However, the NF dependency flattens by reaching 1470 nm. This effect can be observed in the previous work [63], especially for backward and bi-directional pumping, and in previous section 4.2. The mismatch of the NF minima and the gain maxima is commonly explained by the excess noise factor [43] that can be estimated from relative emission and absorption cross-sections and has the theoretical minimum around 1460-1470 nm for germanosilicate bismuth-doped fibres.

The dependence of both gain and NF on the pump power are also recorded and shown in Figure 4.3.1,c,d, respectively. These dependencies are measured for all seven input signal powers and wavelengths, however, the dependencies at only 1430 nm are presented as they all follow the same pattern. A predictable performance of the amplifier is observed: rise of the gain and reduction of the NF with an increase of pump power. The gain curves follow a well pronounced logarithmic trend, and NF ones, on the other hand, are inverse logarithmic. The minimal pump power of 50 mW allowed to already achieve 5 dB gain for 5 dBm signal and 20 dB gain for -25 dBm signal; NF in this case was substantially higher with 10 dB and 7.5 dB for for 5 dBm signal and -25 dBm signal, respectively.

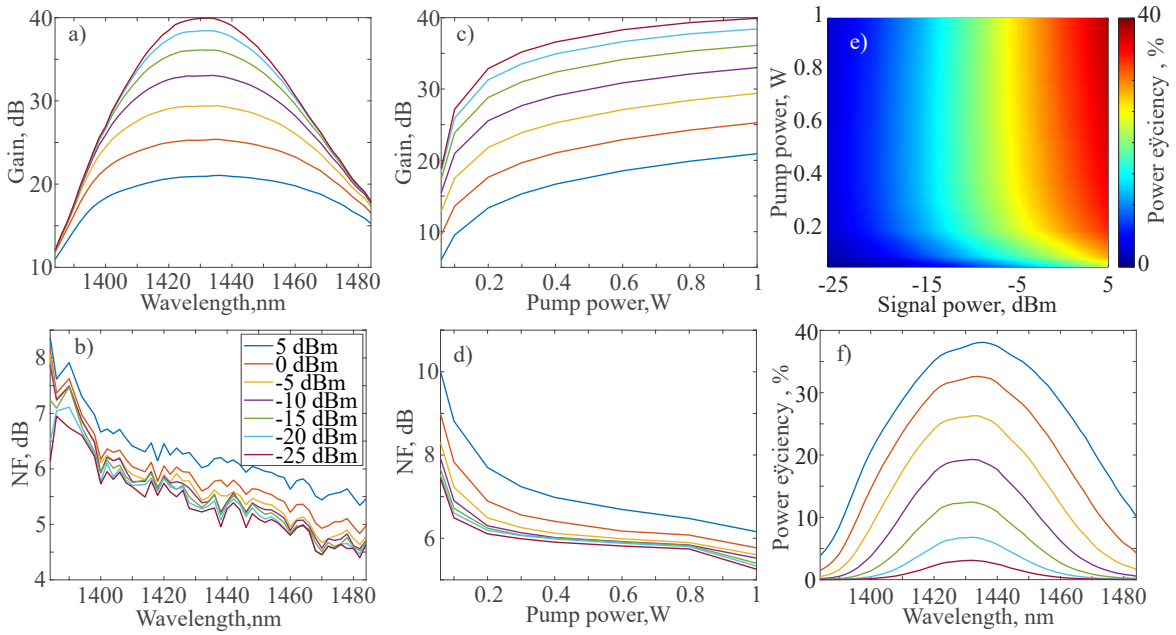

Fig. 4.13 Spectral dependencies of BDFA gain (a) and NF (b) for seven input signal powers and pump power of 1 W; gain (c) and NF (d) dependencies on the pump power for seven input signal powers at 1430 nm; e) colour map of the PCE for depending from both input signal and pump powers; f) spectra of power efficiencies for seven input signal powers.

Another important characteristic of an optical amplifier is optical PCE. The measured PCE dependence on both total pump power and input signal power at the 1430 nm is represented as a colour map in Figure 4.3.1,e. The maximum PCE is 38% which is the record value for Bi-doped fibre amplifiers. This value is observed at a maximum signal power of 5 dBm. The PCE saturates significantly with the increase of pump power after a pump power of around 250 mW. The spectral dependence of PCE for different input power signals is presented in Figure 4.3.1,f. The decrease of input signal power significantly worsens the PCE up to just 3.6% for -25 dBm signal due to lower interactions between the radiation of the signal with Bi-related active centres in the core of the fibre and predominant amplification of spontaneous emission. However, it is important to note that generally amplifiers utilised for DWDM systems work at high total input signal powers (0-10 dBm) due to high number of channels, and thus, the amplifier should maintain high PCE even if individual channels have low power. An additional experiment was performed with 6 channels in E-band (1410, 1430, 1440, 1450, 1470, and 1490 nm) with a total input power of 5 dBm. The PCE of the amplifier was calculated and was the same 38%.

As the next step, the performance of different pumping schemes is investigated. As the general performance of gain and NF with the variations of pump power and signal power have similar behaviour as the bi-directional case, we present the measurements only for

Table 4.2 Comparison of the main amplifier characteristics for 1 W bi-directional pumping scheme and various signal powers

P_{in}, dBm	Gain, dB	Bandwidth, nm	Minimal NF, dB	PCE, %
-25	39.8	30.9	4.6	3.6
-20	38.3	34.5	4.7	7.6
-15	35.9	39.2	4.7	13.2
-10	32.9	45.2	4.8	19.6
-5	29.2	53.3	4.9	26.3
0	25.7	27.7	5	32.6
5	20.8	73.6	5.3	38

three input signal powers of -25 dBm, -10 dBm and 5 dBm. The pump power for all three pumping schemes (bi-directional, forward and backward) are fixed to be 500 mW. In the case of bi-directional pumping, the forward and backward laser diodes operate at the same pump power of 250 mW. The comparison of different pumping schemes in terms of gain and NF for 5 dBm input signal power is presented in Figure 4.14,a,b. The gain spectra for all pumping schemes have almost the same shape, except bi-directional pumping which has a more pronounced gain on the left-hand-side of the spectrum. Even though the provided gain is quite similar for different pumping schemes, the main parameters are highlighted in table 4.2. The backward pumping scheme features the highest gain of 17.8 dB. On the other hand, the bi-directional pumping scheme shows the highest 3 dB gain bandwidth of 80.2 dB.

The NF spectral dependencies vary significantly with pumping scheme choice. Even though the backward pumping scheme features global minimal NF of 5.21 dB at 1480 nm, the main part of the spectra (1384-1460 nm) is higher than the same graphs area of other pumping schemes. The 1460 nm is the wavelength where all three graphs meet and start following significantly different trends. If the curves on the left hand side of the spectra are positioned from forward, bi-directional to backward (from bottom to top), then on the right hand side of the spectra the curves are in reverse order. Such a trend can be explained by the limitations of the measurements and nonlinear effects occurring in the fibre. Predominantly it can be assumed that the four-wave mixing occurs between the signal and the pump modes, that transfers pump modes in vicinity of the signal. This effect is yet to be studied and will be reported in details elsewhere.

In addition to the graphical comparison of the different pumping schemes in terms of gain and NF, different parameters of all pumping schemes are compared in Table 4.3. For 5 dBm input signal power, the highest bandwidth is achieved with the bi-directional pumping scheme due to its more pronounced left-hand side (also obvious from Figure 4.14,a). In

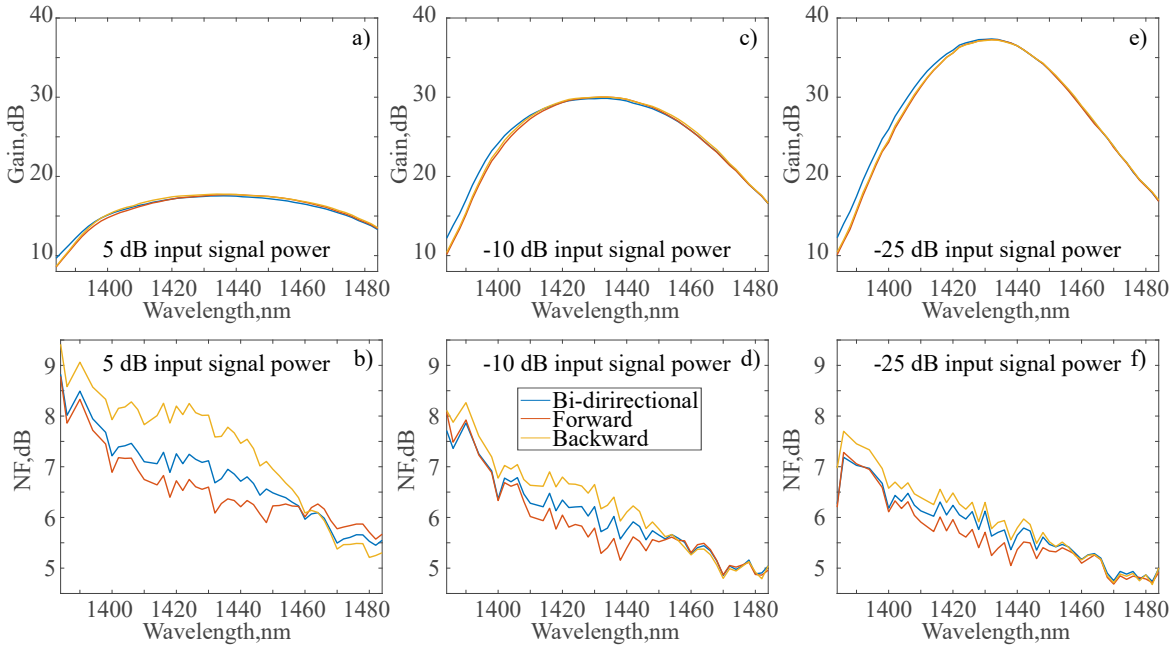

Fig. 4.14 The spectral dependencies of gain and NF for three different pumping schemes and for 5 dBm input signal power (a,b); for -10 dBm input signal power (c,d); for - 25 dBm input signal power (e,f)

contrast, the highest PCE of 37.9% is achieved with the backward pumping scheme along with the highest gain and lowest NF. It is important to note that the lowest NF in the 3 dB bandwidth is achieved in the forward pumping scheme along with the best mean NF performance.

The spectra of gain and NF for -10 dBm input signal power for the three investigated pumping schemes are presented in Figure 4.14,b,c, respectively. The maximum gain for all pumping schemes is significantly increased (with the decrease of signal power) up to 30 dB which is the maximum value among all three of them and is achieved with the backward and forward pumping scheme. The gain, in general, keeps its tendency to be more pronounced at lower wavelengths in the bi-directional pumping scheme, and this pumping scheme also features the highest bandwidth of 49.3 nm. The minimal NF of 4.8 dB is achieved for the backward pumping scheme. However, the difference to other pumping schemes is only in hundredths of dB, which is lower than the accuracy of the measurement methodology. Moreover, the NF spectral performance keeps its trend with lower NF for forward pumping on the hand right side and middle of operation bandwidth. The right hand side of the spectrum features almost equal values of NF for all three pumping schemes with slightly better performance by the backward pumping scheme. The achieved PCE for -10 dBm

Table 4.3 Comparison of the main BDFA-2 characteristics for different pumping schemes and three levels of input signal powers.

P_{in}, dBm	Pump	Gain, dB	Bandwidth, nm	Minimal NF, dB	PCE, %		
	forward	37.3	31.6	4.7	3.5		
-25	backward	37.2	32.1	4.7	3.5	bi-directional	37.
	forward	30	46.6	4.9	20.1		
-10	backward	30	48.5	4.8	20.2		
	bi-directional	29.9	49.3	4.9	19.4		
	forward	17.7	77.6	5.6	37.3		
5	backward	17.8	79.7	5.2	37.9		
	bi-directional	17.5	80.2	5.5	36		

input signal power are 20.1%, 20.2%, and 19.4% for forward, backward, and bi-directional pumping schemes, respectively.

At last, the comparison of pumping schemes in terms of gain and NF for -25 dBm input signal power is presented in Figure 4.14,e,f. The maximum gain is achieved with the bi-directional pumping scheme and is equal 37.4 dB. However, other pumping schemes show similar gain of 37.3 dB for forward and backward pumping schemes. For low signal, the bi-directional pumping scheme enables the widest bandwidth of 32.8 nm and a similar shape with 5 dBm and -10 dBm cases. The NF dependence on wavelength follows a similar trend as in the case of -10 dBm input signal power with even lower differences between pumping schemes. Moreover, the forward pumping scheme features the lowest NF almost in the whole operation bandwidth. The lowest NF of 4.7 dB is achieved for all pumping schemes. Such a small difference in minimal NF shows a significant advantage of forward pumping scheme because the overall performance is the best out of all pumping schemes. The highest PCE of 3.6% is featured by bi-directional pumping followed by 3.5% for forward pumping and 3.46% for the backward pumping scheme.

It is important to highlight, that for all input signal powers the most favourable pumping scheme in terms of achieved NF would be the forward pumping scheme due to generally better performance in operation bandwidth and in the region specifically close to the gain maximum. Moreover, the achieved PCE of 38% which is the record value for Bi-doped fibre amplifiers. Such a high PCE indicates that a significant improvement in the design and fabrication of Bi-doped fibres has been recently made. Most importantly, this value is almost twice as high as the PCE of L-band EDFAs which is typically around 20% [48]. It is also higher than that of C-band EDFAs pumped at 978 nm with 33% PCE, however, it is less than EDFAs pumped at 1480 nm with 50 % PCE [47]. Nevertheless, such a high PCE along with

40 dB Gain and 4.6 dB NF shows a great potential for BDFAs to be used for extending the current optical communication bandwidth while keeping relatively low power consumption of the line, and, potentially, even better than power consumption that L-band amplifiers offer which are currently being deployed.

4.3.2 Fibre from preform 2

The schematic of the amplifier with the fibre based on the preform 2 is described in the previous subsection 4.3.1. The main difference of this amplifier is the fibre that is used. It has the same geometric properties of 6 μm core diameter and 125 μm cladding diameter. The refractive index difference (Δn) is around 0.004. The fibre core consists of 95 mol% SiO_2, 5 mol% GeO_2 and <0.01 mol% of bismuth. The cutoff wavelength (λ_c) of the fibre is measured to be around 1000 nm. However, as this fibre is fabricated from a different preform , the fibre might have slightly different spectroscopic properties. Moreover, the length of the fibre is 20 m less than the fibre used for the second BDFA and is equal 150 m.

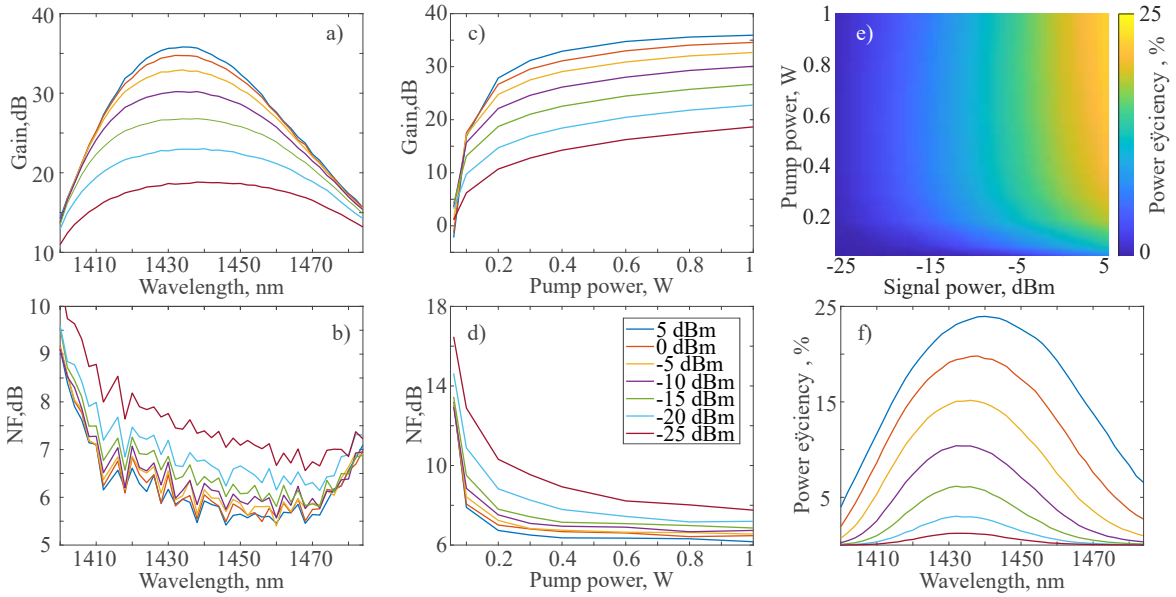

Fig. 4.15 Spectral dependencies of BDFA gain (a) and NF (b) for seven input signal powers and pump power of 1 W; gain (c) and NF (d) dependencies on the pump power for seven input signal powers at 1430 nm; e) colour map of the PCE for depending from both input signal and pump powers; f) spectra of power efficiencies for seven input signal powers.

The structure of this subsection is similar to the previous subsection due to the similarity of the discussed results. To begin with, the performance of the BDFA based on preform 2 (called BDFA-3) is investigated with bi-directional pumping scheme and seven different signal powers in the range from -25 dBm to 5 dBm. The gain and NF for different signal

powers and a maximum total pump power of 1 W (equally split between forward and backward pumps) are shown in Figure 4.3.2. The recorded spectra of gain are shown in Figure 4.3.2,a. The maximum gain of the amplifier is 35.9 dB achieved with -25 dBm signal power. The maximum gain decreases to 18.8 dB with the increase of the signal power to 5 dBm. However, the 3 dB bandwidth increases with the increase of the signal power from 28 nm for -25 dBm signal power to 62.6 nm for 5 dBm signal power. The minimal NF is 5.1 dB for - 25 dBm signal and it rises to 6.5 dB with the increase of the signal power to 5 dBm. For this amplifier, the NF follows a similar trend with the wavelength as the BDFA-1. It decreases significantly with the increase of the wavelength, however, it experiences a fast growing trend after 1470 nm. This, could, perhaps, be explained by significantly saturating gain at higher wavelengths. The main parameters of the amplifier for all recorded signal powers are presented in Table 4.4. Figures 4.3.2,c,d show the dependencies of gain and NF at 1430 nm on pump power for seven different signal powers. All curves follow a natural trend with the pump power increase: the gain rises with the increase of pump power, and NF goes down with the increase of pump power. The curves are presented only for 1430 nm as all wavelengths experienced similar behaviour and additional representation would be redundant.

Table 4.4 Comparison of the main amplifier characteristics for 1 W bi-directional pumping scheme and various signal powers

P_{in}, dBm	Gain, dB	Bandwidth, nm	Minimal NF, dB	PCE, %
-25	35.9	28	5.1	1.5
-20	34.7	30.5	5.3	3.5
-15	32.9	34.8	5.4	7
-10	30.2	39.7	5.5	11
-5	26.8	46.9	5.86	15
0	23	43.6	6.1	20
5	18.8	62.5	6.5	24.8

At last, the PCE of BDFA-3 is presented in Figure 4.3.2,e,f. The measured PCE dependence on total pump power and input signal power at 1430 nm (maximum) is presented in Figure 4.3.2,e. The maximum achieved PCE is 24.8% which is significantly less than for the amplifier reported in subsection 4.3.1. This level of PCE is achieved at 5 dBm signal power, and the further increase of signal power does not provide any improvements to the PCE. The PCE saturates with the pump power after a pump power of around 250 mW. The spectra of PCE for different input signal powers are presented in Figure 4.3.2,f. The increase of the

input signal power significantly improves the PCE from 1.5% to 24.8% for -25 dBm and 5 dBm input signal powers, respectively.

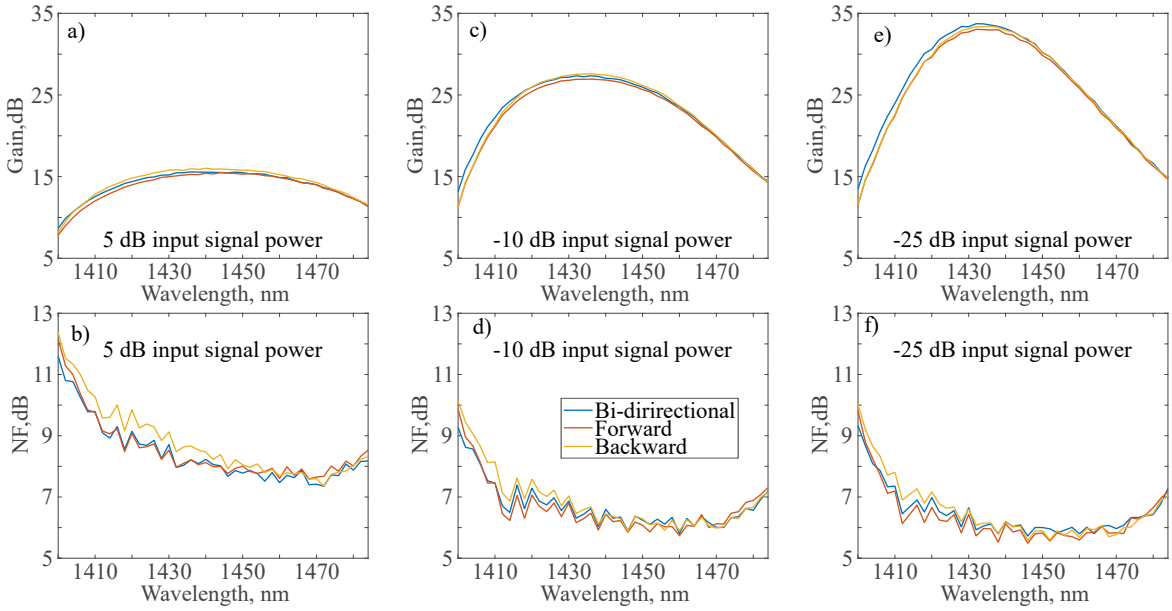

Fig. 4.16 The spectral dependencies of gain and NF for three different pumping schemes and for 5 dBm input signal power (a,b); for -10 dBm input signal power (c,d); for - 25 dBm input signal power (e,f)

As the next step, the influence of different pumping schemes on the amplifier performance is investigated. As the performance of the amplifier does not change significantly between the critical input powers of 5 dBm, -10 dBm, and -25 dBm, only the spectra for these signal powers are presented in Figure 4.16. The pumping scheme in all cases is 500 mW, and the bi-directional pumping scheme has 500 mW pump power equally split between forward and backward pumping diodes. In general, the performance of the amplifier is quite similar to BDFA-1 and BDFA-2. To begin with, the 5 dBm input signal power is considered. The gain and NF spectra for different pumping power schemes and 5 dBm input signal power are presented in Figure 4.16,a,b. All the gain curves have almost the same behaviour, with only the backward pumping scheme having slightly higher gain in almost the whole operation region. Forward pumping shows the worst performance in terms of gain and this trend is repeated with BDFA-3 similarly to BDFA-2. The maximum achieved gain is 16 dB for backward pumping, and the lowest gain is 15.5 dB for forward pumping. The NF spectra trends have similarities with the same spectra for BDFA-2.

The NF also goes down significantly with the increase of wavelength and then starts to grow. The forward pumping scheme performs almost the same as the bi-directional pumping scheme. The backward pumping scheme features the highest NF on the left hand side of the

Table 4.5 Comparison of the main BDFA-2 characteristics for different pumping schemes and three levels of input signal powers

P_{in}, dBm	Pump	Gain, dB	Bandwidth, nm	Minimal NF, dB	PCE, %
	forward	33	28.9	5.5	1.3
-25	backward	33.4	28.8	5.6	2
	bi-directional	33.7	28.7	5.7	1.5
	forward	26.9	42.7	5.7	9.9
-10	backward	27.6	41.4	5.9	11
	bi-directional	27.4	42.7	5.8	10.5
	forward	15.5	66.8	7.6	22
5	backward	16	66.7	7.3	25
	bi-directional	15.6	68.2	7.4	23

spectrum, but then becomes better than the forward one and has similar performance to the bi-directional. This NF alteration is described in detail in subsection 4.3.1 where it is more significantly pronounced. The lowest NF is achieved for the backward pumping scheme and is equal 7.4 dB. The worst performance in terms of NF is for forward pumping with 7.6 dB NF. However, it is important to note again, that the area with the highest gain has a better performance in terms of NF for both bi-directional and forward pumping schemes. The 3 dB bandwidth in all schemes is similar, but the highest value of 68.2 nm is achieved for the bi-directional pumping scheme. The comparison of the main parameters of the amplifiers for different pumping schemes is presented in Table 4.5. At last, the PCE should also be compared. The highest PCE is achieved for the backward pumping scheme and is equal 25% which aligns well with the highest achieved gain.

Next, the performance of the pumping schemes in terms of gain and NF spectra are compared for -10 dBm input signal power. This time, the bi-directional pumping scheme visually has the widest bandwidth, however, gain spectra for all pumping schemes are similar and are presented in Figure 4.16,c. The highest gain is achieved for the backward pumping scheme and is equal 27.6 dB. The lowest gain of 26.9 is measured for the forward pumping scheme. The forward and backward pumping schemes have the same 3 dB gain bandwidth of 42.7 dB. The lowest bandwidth of 41.7 dB is achieved for the backward pumping scheme. Figure 4.16,d shows the comparison of NF spectra for different pumping schemes. Similar behaviour to the trend visible for 5 dBm signal can be seen: NF goes down with the wavelength increase up to 1470 nm, when the NF starts to grow back. The forward pumping scheme has the lowest NF of 5.7 dB and is lower than other curves until 1470 nm. After that, the backward and bi-directional pumping schemes start to compete in terms of the

best performance. The highest minimal NF is 5.9 NF achieved for the backward pumping scheme. The PCE is yet again the highest for backward pumping with 11%. The lowest PCE of 9.9 % is achieved for the forward pumping scheme.

At last, the -25 dBm signal amplification is compared with different pumping schemes. The gain spectra comparison for three different pumping schemes is presented in Figure 4.16,e. The highest gain of 33.7 dB is achieved for the bi-directional pumping scheme. The lowest gain is achieved again for the forward pumping scheme. The highest gain bandwidth is 28.9 nm and is achieved with the forward pumping scheme. However, all gain bandwidths differ insignificantly. The NF spectra comparison for the three pumping schemes is shown in Figure 4.16,f. The lowest minimal NF is achieved with forward pumping and is 5.5 dB. The highest one is for bi-directional pumping and is 5.7 dB. All NF curves overlap a lot with each other, especially on the right hand side of the spectrum. However, overall performance of the forward pumping scheme is considered to be the best. The highest PCE of 2% is achieved with the backward pumping scheme. The lowest value of 1.3% is yet again achieved for the forward pumping scheme.

To conclude, the behaviour of the BDFA-3 is quite close to BDFA-2, however, BDFA-3 suffers from slightly lower gain, PCE, and higher NF. All the conclusions drawn regarding gain and NF performance of BDFA-2 can also be applied for BDFA-3. The PCE of the developed amplifier is higher than that of BDFA-1, however, it cannot compete with the outstanding performance of the BDFA-2. This behaviour can be explained by slightly different composition of the fibre core, which will be examined in details in the future.

4.4 Pumping scheme comparison

With the capabilities provided by the automatic measurement setup, the pump optimisation can be performed by direct measurement of the performance of the amplifiers with different pumping combinations. Three different pumping lasers are available for optimisation: 1330 nm, 1310 nm, and 1260 nm. Two amplifiers are characterised in terms of gain, gain bandwidth, NF, and PCE with all available combinations of the bi-directional pumping scheme: BDFA-1 and BDFA-2. The measurements with BDFA-3 are not made as its performance is close to the BDFA-2. However, this characterisation is planned to be conducted in the future. Both amplifiers are characterised with pumps running at 1600 A, which corresponds to different pump values for different diodes. Even though the difference is small for pump diodes at 1330 and 1310 nm (less than 40 mW), the pump power of 1260 nm laser diodes is significantly higher than those at longer wavelength and is higher than 100 mW. However, even though the initial approach of making the measurements with constant current instead of pump power is

not completely correct, there are some conclusions that can be made based on the received data measurements. Both amplifiers are tested with moderately high and moderately low signal powers of 0 dBm and -20 dBm and characterised in terms of maximum gain, 3 dB bandwidth, and minimal NF. Additional measurements are planned to be conducted after submission, focused on measurement of all pumping schemes with equal pumping power and comparison in terms of PCE to be made as well.

The results of the measurements and a comparison between different pumping schemes for BDFA-1 is presented in Table 4.6. The first number in the column "Pumping scheme" indicates the wavelength of the forward pumping, and the second number shows the wavelength of the backward pump laser diode. The best performance in terms of maximum gain for 0 dBm signal can be obtained with the pumping scheme with both 1330 nm laser diodes. This can be mostly explained by the fact, that 1330 nm pump is the closest to the maximum of the absorption spectra. However, for the -20 dBm signal, both 1130-1310 nm and 1310-1330 nm pumping schemes have similar gain around 32.9 which is the highest among all pumping schemes. On the other hand, the lowest gain is achieved with both 1260 nm pumps, especially for 0 dBm signal power. In contrast, as the gain is generally lower for this pumping scheme, the bandwidth is the highest with 54.9 nm and 33 nm for 0 dBm and -20 dBm input signal power. In terms of NF, the best performance for 0 dBm input signal power is both 1260-1310 nm and 1260-1330 nm pumping scheme. These two pumping schemes also show the two lowest NF for -20 dBm input signal power. This behaviour can be explained by lower ASE generated with the lower pumping wavelengths due to their remoteness from the absorption maximum, thus the pump radiation is absorbed more uniformly by the fibre and does not produce as much ASE.

As the next step, the results of the measurement of BDFA-2 are presented in Table 4.7. The maximum gain is yet again achieved with the 1330-1330 nm pumping scheme with 24.9 dB for 0 dBm input signal power, and 38.3 dB for -20 dBm. However, most of the pumping schemes with just 1310 and 1330 nm pump lasers have a comparable level of gain higher than 38 dB. The lowest gain is achieved with 1260-1260 nm. The transition for 1260 is less effective than the one for 1330 nm for amplification at 1440 nm transition. Similar performance of BDFA-2 to BDFA-1 can be observed in terms of gain bandwidth. The highest one for both input signals is the 1260-1260 nm pumping scheme with 67.2 dB and 38.2 dB for 0 dBm and -20 dBm, respectively. Using lower wavelength pump laser diodes for forward pumping and higher wavelength for backward pumping allows to achieve the best performance in terms of achieved NF. The lowest general NF performance is best with 1310-1330 nm, and 1260-1330 nm pumping schemes, with the latter being slightly better with 4.8 dB for 0 dBm input signal power, and 4.4 dB for -20 dBm input signal power.

Table 4.6 Comparison of the main BDFA-1 characteristics for different pumping schemes and two levels of input signal powers

Pumping	Gain, dB		Bandwidth,nm		Minimal NF, dB	
scheme, nm	0 dBm	-20 dBm	0 dBm	-20 dBm	0 dBm	-20 dBm
1330-1330	22.7	32.8	48.5	29.6	6	5.3
1330-1310	22.2	32.9	49.2	30	6.3	5.3
1310-1330	22.2	32.9	48.6	29.8	6.1	5.3
1310-1310	22.1	32.6	49.8	30.2	6.2	5.3
1260-1310	21	32.7	52.2	31.2	5.9	5.1
1310-1260	21.2	32.5	51.9	31.2	6.3	5.5
1260-1330	21.4	32.5	50.5	30.3	5.9	5.1
1330-1260	21.3	32.2	49.9	30.8	6.2	5.3
1260-1260	18.9	31.2	54.9	33	6.5	5.7

To conclude, the lower wavelength forward pump laser diodes (1310 nm or 1260 nm) allow to significantly improve the performance of the amplifier in terms of NF. However, if the gain is the critical factor for a specific application, the pump lasers with higher wavelength should be used for gain enhancement. One can see that this conclusion can be applied for both amplifiers, and similar performance is expected from BDFA-3. Later in the text the amplifier designs are presented with already optimised pump wavelengths to allow both good NF and gain performance, specifically for better performance in transmission experiments enabled by developed BDFAs.

4.5 Summary

In this chapter the procedure of main amplifier characteristics measurement was presented and discussed. Three amplifiers were developed based on three different Bi-doped active fibres. These amplifiers were thoroughly characterised in terms of gain, NF, and PCE with different pumping schemes, pump powers, and input signal powers. The record characteristics of 39.8 dB gain, 4.5 NF for -25 dBm input signal power and 38% PCE for 5 dBm input signal power are achieved with the BDFA-2. These characteristics were compared to the commercial EDFAs, and it was proven that such performance shows a great potential for E-band BDFAs to be used for expanding the bandwidth of the current telecommunication optical links. The BDFA-1 and BDFA-2 performance was also compared with the different pumping wavelengths and their combinations. For both amplifiers, it has been evident that use of a shorter wavelength pump for forward pumping and longer wavelength pump for

Table 4.7 Comparison of the main BDFA-2 characteristics for different pumping schemes and two levels of input signal powers

Pumping	Gain, dB		Bandwidth,nm		Minimal NF, dB	
scheme, nm	0 dBm	-20 dBm	0 dBm	-20 dBm	0 dBm	-20 dBm
1330-1330	24.9	38.3	63.7	34.7	4.9	4.5
1330-1310	24.8	38.3	62.4	34.7	5	4.4
1310-1330	24.7	38.2	61.3	34.7	4.8	4.4
1310-1310	24.5	38	64	34.9	5	4.5
1260-1310	23.4	37.2	65.8	36.9	4.9	4.5
1310-1260	23.7	37.3	64.3	36.3	5	4.6
1260-1330	23.5	37.2	66.1	35.8	4.8	4.4
1330-1260	24.2	37.7	62	34.5	4.9	4.6
1260-1260	21.5	35.5	67.2	38.2	5.1	4.7

backward allows to improve the NF performance. However, if the gain is the critical factor for a specific application, the pump lasers with higher wavelength should be used for gain enhancement.

Chapter 5

Data transmission experiments enabled by BDFA

This chapter is devoted to the experimental research of capabilities of developed E-band BDFAs for data transmission. Different modulation formats are considered, including IM/DD and coherent signals.

5.1 Main metrics of signal quality for IM/DD and coherent transmission signals

In digital communication systems, the bit-to-error rate (BER) is considered as one of the most popular and straightforward performance indicators [118]. The BER shows a simple ratio between received error bits and the total amount of received bits. Figure 5.1 schematically shows an EYE diagram of a fluctuating binary of on-off keying non-return-to-zero (OOK NRZ) signal received by the optical receiver. The EYE diagram is a representation of the signal by the oscilloscope by repetitive sampling of the digital signal from a receiver, while the data rate is used to trigger the horizontal sweep. The t_d shows the period of sampling. The sampled values fluctuate from bit to bit around an average value of μ_1 for 1 and μ_0 for 0. The sampled values are then compared with decision value μ_d and if $\mu > \mu_d$ then the decision is made towards bit 1. Bit 0 is achieved when $\mu < \mu_d$. However, an error occurs when the decision is made incorrectly due to the noise. The error probability as BER can then be represented as:

$$BER = \rho(1)P(0|1) + \rho(0)P(1|0), \tag{5.1}$$

where ρ_1 and ρ_0 are the probabilities of receiving a 1 and a 0, respectively; $P(0|1)$ is the probability of deciding a 0 when in fact receiving a 1, and $P(1|0)$ is the probability of deciding 1 when receiving a 0. In the case when probabilities of a 1 and a 0 to occur are the same, the equation 5.1 can be simplified to:

$$BER = \frac{1}{2}(P(0|1) + P(1|0)). \tag{5.2}$$

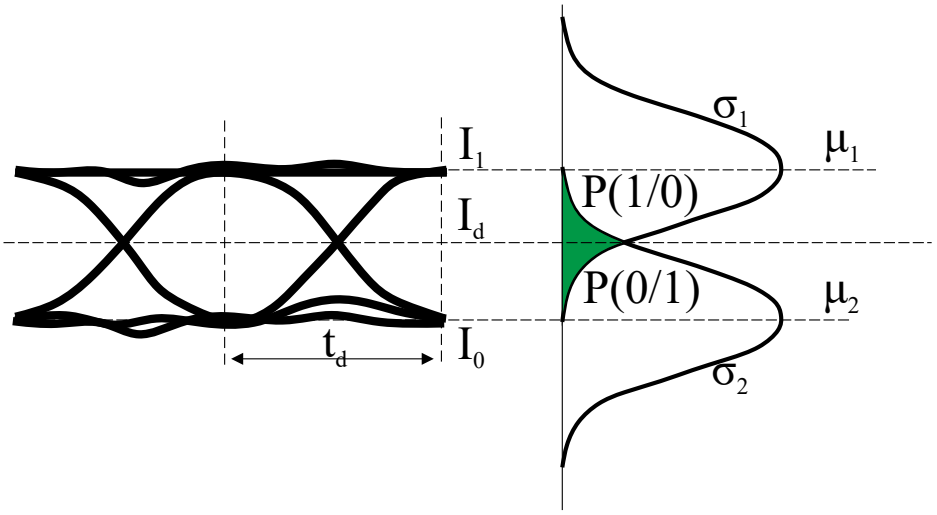

Fig. 5.1 EYE diagram of an NRZ OOK signal.

Figure 5.1 also shows the probability density functions of bit 1 and 0 distributions on the receiver and the width of the curves represents the noise in the signal. σ_1 and σ_0 are the standard deviations for a 1 and a 0 level, as the noise on the receiver side follows a Gaussian distribution. The lower the noise, the narrower the distribution curve and therefore the smaller the overlap. In fact, the overlap area between the distribution curves for a 1 and a 0 is what determines the BER, as that is where the receiver has a greater chance of interpreting a 1 as a 0 and vice versa, producing a bit error. The equation 5.2 can be represented through mean intensity levels and standard deviations in the following way:

$$BER = \frac{1}{4}(erfc(\frac{\mu_1 - \mu_d}{\sigma_1\sqrt{2}}) + erfc(\frac{\mu_d - \mu_0}{\sigma_0\sqrt{2}})), \tag{5.3}$$

where $erfc$ is the complimentary error function. The details of the transition from Equation 5.2 to equation 5.3 can be found in [1]. To connect the BER to other important signal quality metrics, the Q factor should be introduced. The Q factor is the parameter showing the difference between the mean values of the signal levels for a 1 and a 0 that

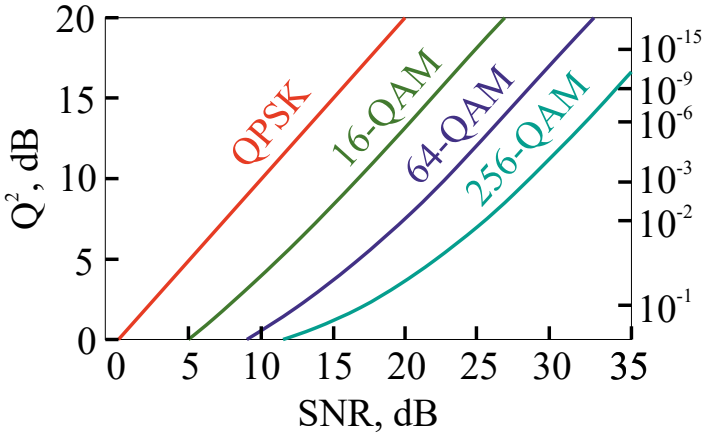

Fig. 5.2 Theoretical relation between Q factor, BER, and SNR.

are determined by μ_1 and μ_0, respectively (Figure 5.1) divided by the sum of the standard deviations for a 1 and a 0 [119]:

$$Q = \frac{\mu_1 + \mu_0}{\sigma_1 + \sigma_0}. \tag{5.4}$$

For a binary system, the definition of Q factor is well defined, and the one-to-one equivalence between Q, SNR, and BER is well known. The Q factors are often calculated from EYE diagrams recorded on digital sampling oscilloscopes or from BER version decision threshold characteristics [120]. However, the relation between a parameter derived from the statistical Q-function, the SNR and BER changes for each modulation format for non-binary systems [121]. This relation can be found starting with examining the hard-decision performance predictions for a rectangular constellation with N constellation points:

$$BER = \frac{2}{log_2(N)}(1 - \frac{1}{\sqrt{M}} erfc(\sqrt{\frac{3 \cdot SNR \cdot log_2(N)}{2(N-1)}}). \tag{5.5}$$

To further understand the relation between BER and Q factor, the relation between SNR and Q factor should be introduced (details are presented in the book by Agrawal [1]):

$$SNR = \frac{2Q}{\sqrt{N}}. \tag{5.6}$$

In order to avoid the use of a double-log axis, the results are typically represented by a Q factor. To obtain Q factor from a BER (for any constellation), the binary version of Equation 5.1 should be solved with regards to the relation between SNR and Q factor

(Equation 5.6):

$$BER = \frac{1}{2} erfc(\frac{Q}{\sqrt{2}}). \tag{5.7}$$

Using the equation 5.1 and equation 5.7, one can obtain the relation between Q factor, SNR and BER for the four most commonly used modulation formats: QPSK, 16 QAM, 64 QAM, and 256 QAM (Figure 5.2[14]). There are two main patterns of the curves that should be noted. The first is that the performance of the Q^2 factor requires the same value of SNR for QPSK, which significantly simplifies the analysis of the signal quality for QPSK. However, the same level of performance requires a significant increase of SNR for QAM modulation signals with incremental increase with the constellation complexity.

5.2 IM/DD experiments

In this section the setup of IM/DD system is presented and characterised. At the beginning of this experiment there was only one demonstration of the data transmission in E-band enabled by BDFA [69]. The work featured 80 km long transmission of a single channel of NRZ OOK. The goal of the work presented here was to repeat the experiment presented by Melkumov and exceed the length of the NRZ OOK data transmission, number of channels transmitted, and operation spectral band in E-band enabled solely by BDFA.

5.2.1 IM/DD setup description and performance characterisation

Due to the lack of experimental investigations of BDFAs, performance in terms of signal transmission in E- and S- optical bands of the previously designed transmission setup was improved and tested to allow characterisation of the signal transmission in any preferred band. For this experiment, the wavelength range was fixed to 1410-1490 nm as this spectral range is predicted to have sufficient gain enabled by the BDFA. The setup allows to transmit and receive an NRZ OOK coding with up to 20 GBaud rate and is presented in Figure 5.3.

The scheme consists of a tunable laser which emits radiation in the spectral range from 1410 to 1490 nm. Using a standard SMF, the radiation from the tunable laser is transmitted through a $LiNbO_3$ electro-optical modulator where the electrical modulation is transferred into optical modulation via electro-optical effect [122]. The modulator receives the electrical signal from an RF signal driver. The RF signal driver gets the PRBS sequence of the NRZ OOK signal from the pulse pattern generator and amplifies it in regards with the bias voltage controlled by the bias board. The bias board is used to setup up the bias voltage of the modulator as the modulator performance varies significantly depending on radiation wavelength and bias voltage. The typical transfer function of an electro-optical modulator is

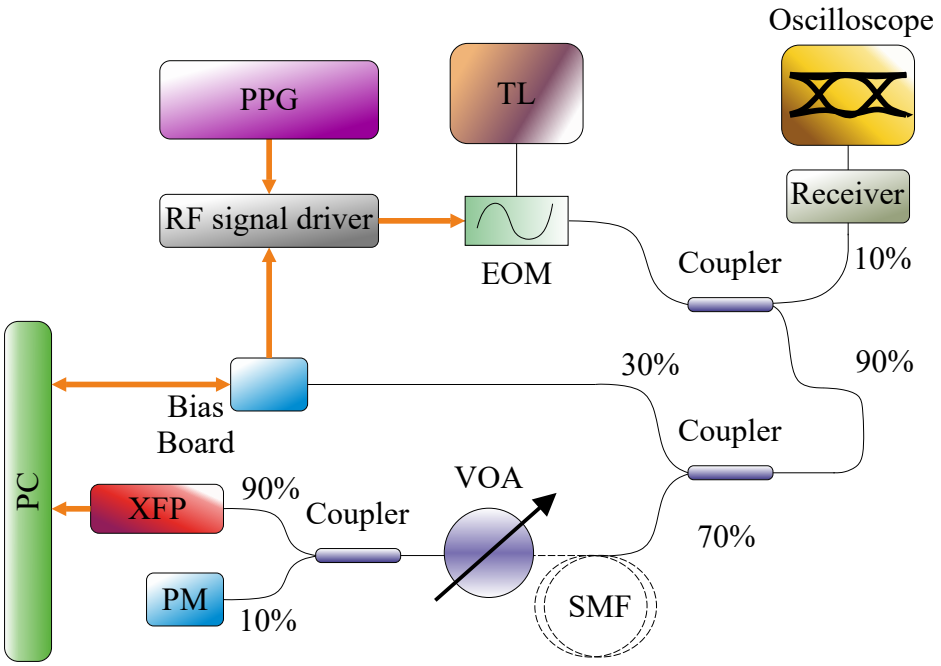

Fig. 5.3 Schematic of NRZ OOK transmission measurement.

presented in Figure 5.4. The dependency of the transmittance of the electro-optical modulator can be described by quadratic sine: $sin^2(\frac{\pi V}{2V_{pi}})$. However, a typical electro-optical modulator also has a quasi linear region of the voltage to the transmittance conversion allowing an accurate transition from electrical modulation to the modulation of transmittance. The modulation of transmittance is then converted into optical modulation when the optical radiation is transmitted though a modulator. Thus, the bias voltage should be carefully chosen to enable this accurate transition and usually equals $V_\pi/2$, where V_π is the voltage which enables maximum transmittance of the modulator.

After the modulation is applied to the optical signal, the radiation of the data carrier is split into two parts by a 90/10 coupler. The smaller part of the radiation then goes to the receiver where it is converted to the electrical signal that is transmitted to the oscilloscope for EYE diagram control. It allows to control the quality of the modulated signal before it comes into the measurement line. The EYE diagram is used to tune the performance of the bias voltage to enable the best quality of the modulation. The second part of the radiation is again split into two parts: one part goes to the bias board, and another one goes to the receiver. In the back-to-back case the signal carrier is directed to the receiver part of the setup. It consists of VOA for signal power adjustment and another 90/10 coupler that allows simultaneous detection of the signal by the XFP module and optical power measurement by the PM. It is worth noting that the XFP module has an internal laser source and modulator

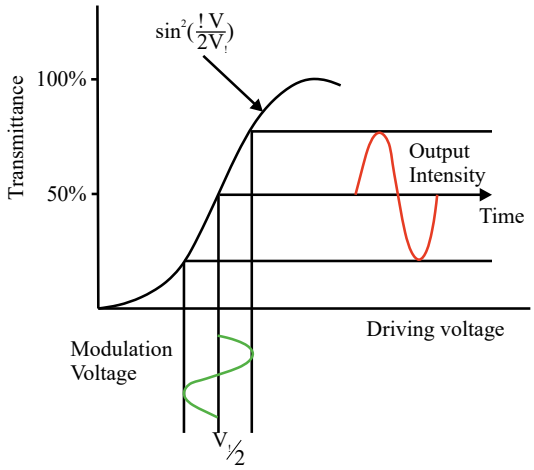

Fig. 5.4 The typical transfer function of an electro-optical modulator.

that is designed for C-band operation, thus it is impossible to use an internal XFP source for measurements beyond C-band. The PC is used for controlling of both bias and receiving analysed data by the XFP module. The commercial interface of the XFP module is presented in Figure 5.5 and developed by SocioNext. The interface shows the counted bits, errors, and calculated BER by XFP. The XFP module also measures received optical power, however, the accuracy of the measurement is 1 dB, thus, an additional external PM is used for accurate optical power measurements. The interface allows to choose the patterns and the baud rate of the transmitted signal. Moreover, it controls the internal laser of the module and allows its tunability.

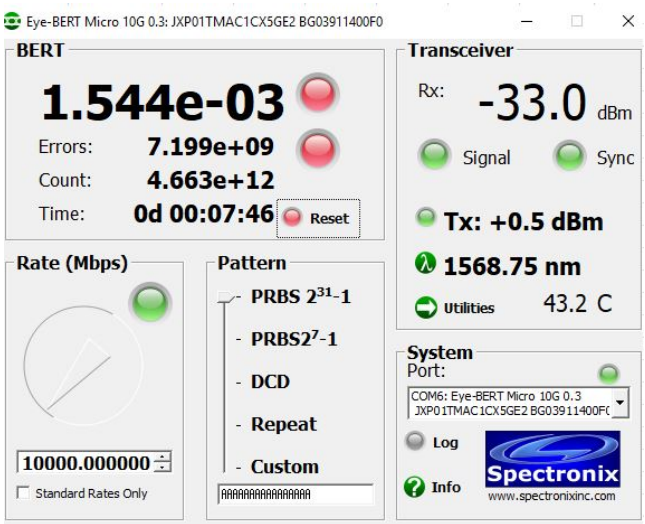

Fig. 5.5 The interface of the XFP module.

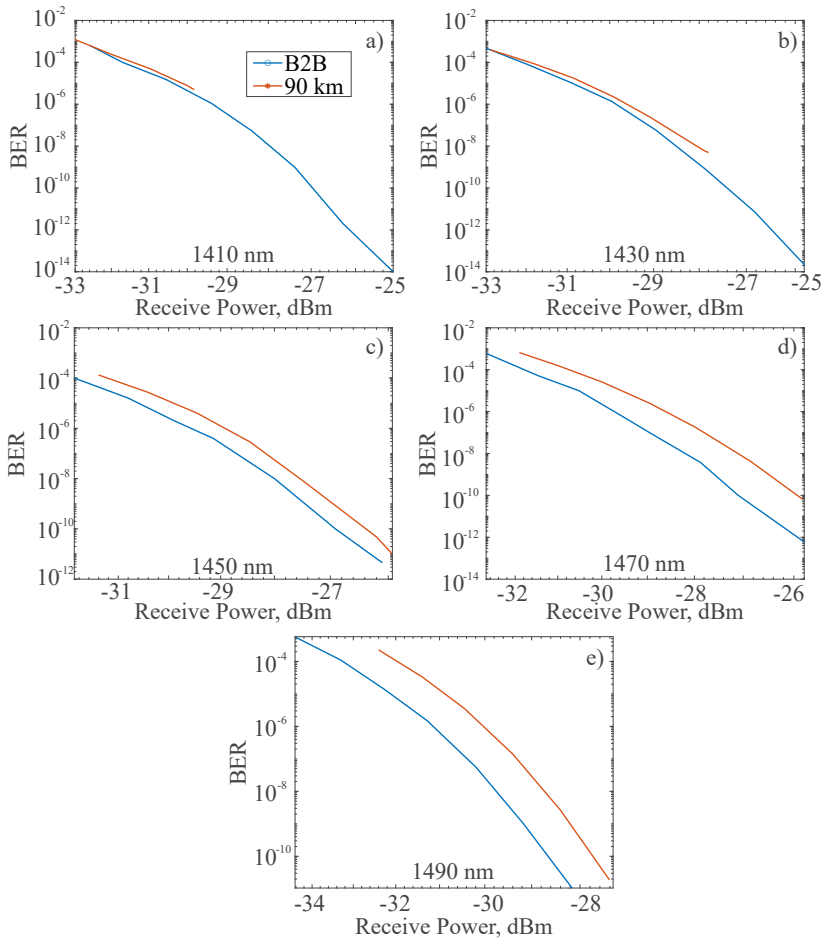

Fig. 5.6 Bit-to-error rate (BER) characteristic vs Receiver power (RX power) for different wavelengths for back-to-back case, and transmission line length of 90 km of SMF.

When the transmission is performed, additional 90 km of SMF is installed before VOA. The measurements are generally performed in the following order. First, the back-to-back performance is measured by changing the power on the receiver by VOA starting from the lowest detected power and increasing the receive power step by step. After that, the experiment is repeated but with additional 90 km of SMF introduced before VOA. The results of the experimental measurements of BER for 10 GBaud NRZ signal vs received signal power for different wavelengths and fibre lengths are presented in Figure 5.6.

The difference of the performance for different wavelengths for B2B case can be explained by the responsivity of the photodiode and different performance of the optical modulator at different wavelengths. The responsivity of the typical InGaAs photodiode is presented in Figure 5.7 [123]. It is clearly seen that the responsivity of the photodiode decreases significantly in E and S-bands in comparison to the C-band. The BER performance has a well pronounced trend: the penalty is minimising with the decrease of the wavelength. This

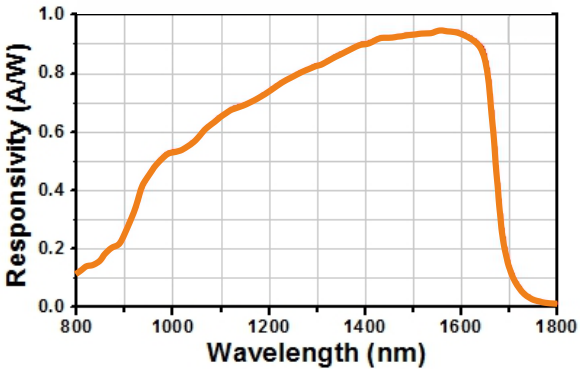

Fig. 5.7 Responsivity of typical InGaAs photodiode.

can be explained by a significant decrease of the dispersion towards shorter wavelengths with zero dispersion wavelength for SMF being typically around 1330 nm. Moreover, generally penalties of the transmission are quite minor (except 1490) and the performance shows a good potential for the fibre increase, especially if the amplifier is introduced. However, better performance towards shorter wavelengths should be taken into the account when the performance of a transmission for longer lengths enabled by BDFA are analysed.

5.2.2 NRZ OOK 160 km transmission in E-band enabled by single BDFA

As the next step, the BDFA described in Section 4.2 is used for IM/DD transmission of 10 GBaud NRZ OOK. As the results from the previous subsection 5.2.1 indicated, there is a potential to increase the length of the transmission line by introducing an optical amplifier. The experimental setup of the transmission experiment enabled by the E-band BDFA is presented in Figure 5.8. The output radiation of the TL operating in the spectral range of 1410-1490 nm is modulated by a transmitter setup covered in the previous Subsection 5.2.1, and its power is controlled with a VOA. The radiation of three CW laser diodes operating at the wavelengths of 1430, 1450, and 1470 nm was combined in a multiplexer (MUX). These three channels are used only as dummy channels to fill up the signal spectrum and do not carry any data. One of the 50:50 coupler outputs is used for the input signal monitoring of input signal power and optical spectrum with a PM and an OSA, respectively. The total input signal power is 5 dBm and equally split between four channels. A typical input spectrum of the signal with TL adjusted to 1410 nm is shown in Figure 5.9a (spectral lines for the input and outputs are digitally shifted by ±2 nm during data processing to avoid overlap). In the case of back-to-back measurements, the input signal from the other coupler end

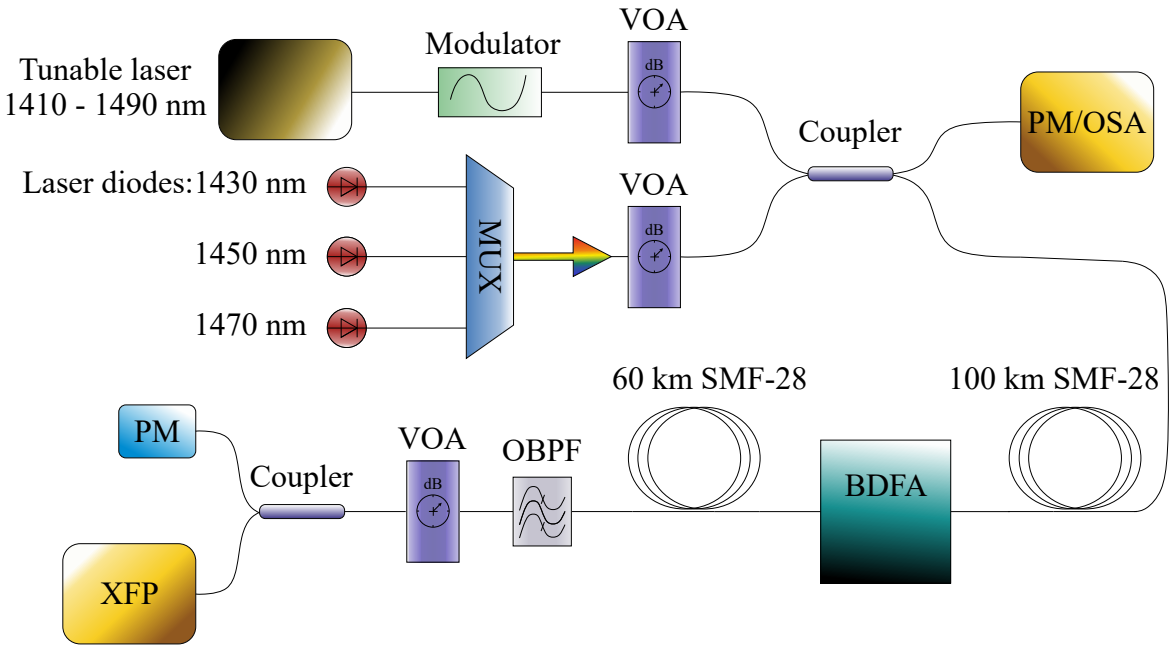

Fig. 5.8 The scheme of the BER measurement of 4 NRZ 10 Gbaud channel transmission through SMF-28 fibre using a BDFA.

goes directly into the receive line. The receive line includes an OBPF for modulated signal filtering, a VOA for received power control, and a coupler for the simultaneous detection of the received power and BER measurement with PM and XFP module, respectively. The characteristics of the XFP module are covered in previous subsection 5.2.1. There are three different experimental conditions under which the transmission is performed: back-to-back case; transmission through 100 km and amplification with BDFA; transmission through 100 km, amplification with BDFA and a further transmission through 60 km.

As a first step, the back-to-back experiment is performed. After that, the input signal is transmitted over the 100-km span of SMF-28 and amplified by the developed BDFA. Here, the amplifier designed and presented in section 4.2 is used with bi-directional pumping at 1320 nm. The forward and backward pump powers are 470 mW and 330 mW, respectively, which is higher than that reported before. The spectra of gain and NF in operating bandwidth are shown in Figure 5.9,b. The maximum gain is equal to 32 dB, and the NF varies from 5 dB at 1450 nm to 6.5 dB at 1410 nm. The typical spectrum of the signal at the output of the BDFA is depicted in Figure 5.9,a with the red line. In the case of 160-km transmission line, an additional 60-km spool of SMF fibre is added after the BDFA. The typical spectrum of the signal after the additional 60-km span is shown in Figure 5.9,a with the blue line.

To compare the performance across the band, three fixed dummy channels at wavelengths of 1430, 1450, 1470 nm are coupled with a data carrier signal (TL). That allows BER

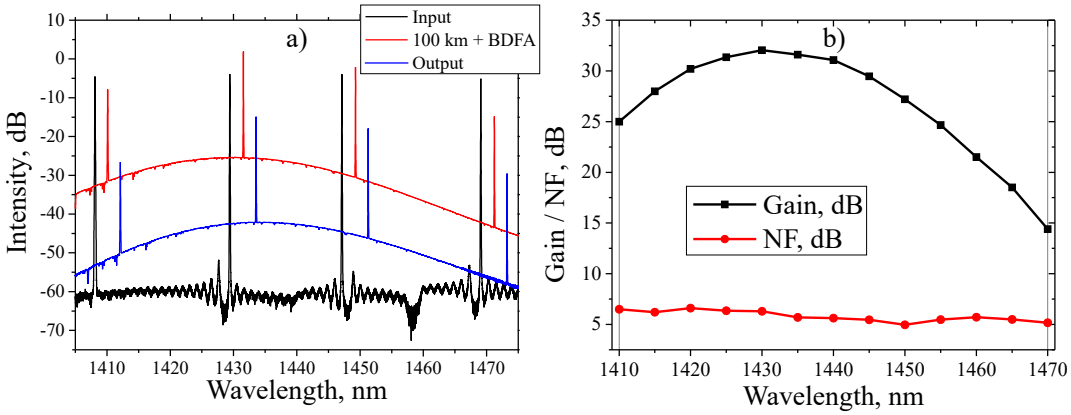

Fig. 5.9 BDFA and transmission line performance. a) signal spectra at the transmission line input (black line), after BDFA (red line), and at the transmission line output (blue line), the black and the blue lines are artificially shifted by ± 2 nm to aid visibility by avoiding spectra overlap; b) spectra of gain (black line) and NF (red line) of the BDFA in operation band.

monitoring in the spectral range of 1410-1460 nm (BER measurements for wavelengths longer than 1460 nm were not possible because of insufficient amplifier gain). The measured BER dependencies on the received power at 1425 nm for back-to-back, 100-km long, and 160-km long schemes are presented in Figure 5.10. The power penalty has been examined at the hard-decision forward error correction threshold for NRZ OOK signals of 10^{-3} as a difference between the back-to-back case and the respective transmission line length. A comparison between these power penalties obtained at different wavelengths for 100- and 160-km-long transmission lines is presented in Table 5.1.

Table 5.1 Received power penalties at the hard-decision forward error correction threshold for NRZ OOK of 10^{-3} BER for 100 km long and 160 km long transmission lines

Wavelength, nm	1410	1415	1420	1425	1435	1440	1445	1455	1460
100 km Penalty, dB	0.8	0.71	0.62	0.42	0.1	0.07	0.36	1.39	1.62
160 km Penalty, dB	1.15	1.02	0.89	0.62	0.63	0.67	0.98	3.02	3.7

There are two main physical effects contributing to the BER penalties for the IM/DD signal: chromatic dispersion and optical amplifier noise. Even though nonlinearity can potentially impact such signal, the signal power should be significantly higher for the impact. The dispersion slope of the SMF is responsible for the higher penalties at the longer wavelengths of 1455 and 1460 nm. At the same time, penalties increase due to the higher level of amplifier noise in the "blue" part of the spectrum. Table 5.1 shows that the increase of the transmission span length to 160 km changes the penalty in the spectral range of 1410-1445 nm insignificantly. The additional penalties due to fibre dispersion and amplifier ASE

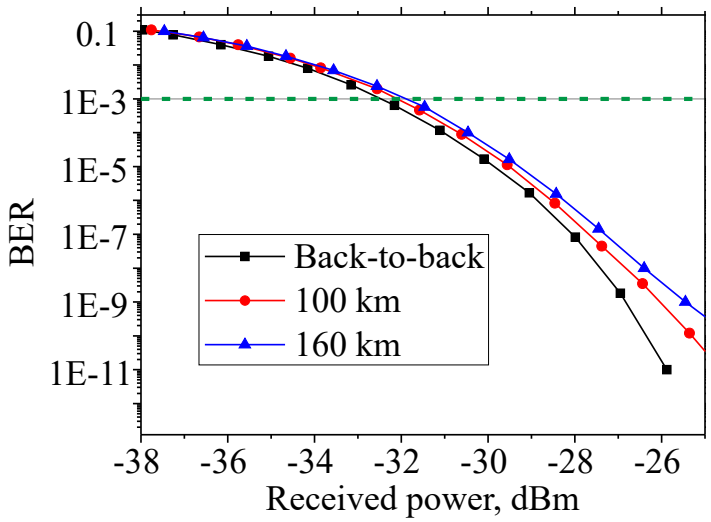

Fig. 5.10 Measured BER dependency on the received power at 1425 nm in back-to-back (black line) case, at 100 km and BDFA output (red line), and after 160 km transmission (blue line); hard decision forward-error correction threshold for NRZ OOK (green dashed line).

are evidently low enough (<0.5 dB) for the 100-km-long line to allow almost penalty-free transmission in the spectral range of 1425-1445 nm.

The lowest power penalty has been observed at the wavelength of 1440 nm (0.07 dB, 100-km transmission line), and 1425 nm (0.62 dB, 160-km transmission line). The penalty is higher for the longer transmission line, as expected. The point of the minimum penalty shifts to a shorter wavelength with increase of the span length due to lower impact of dispersion. The impact of the dispersion on the overall transmission performance predictably grows with the increase of the fibre span length. Therefore, the transmission results might be further improved by using a lower dispersion fibre or compensating fibre dispersion in this spectral range, however, a more perspective approach is to use coherent modulation formats to allow a significant increase of the data rate.

The additional visual representation of the results in Table 5.1 is shown in Figure 5.11. Both power penalties curves show good correspondence with the dispersion curve. It is clearly seen that the difference between the curves for 160 km transmission and 100 km transmission grows with the increase of the wavelength and, thus, the dispersion parameter. To conclude, the setup of NRZ OOK transmission was presented and discussed. The transmission experiments of 10 GBaud NRZ OOK through various lengths of SMF were presented including a 4 channel 10 GBit/s E-band transmission through 160 km enabled by a single BDFA. The results were discussed and are in good agreement with the main physical effects affecting IM/DD systems: loss, dispersion, and amplifier noise. As the next

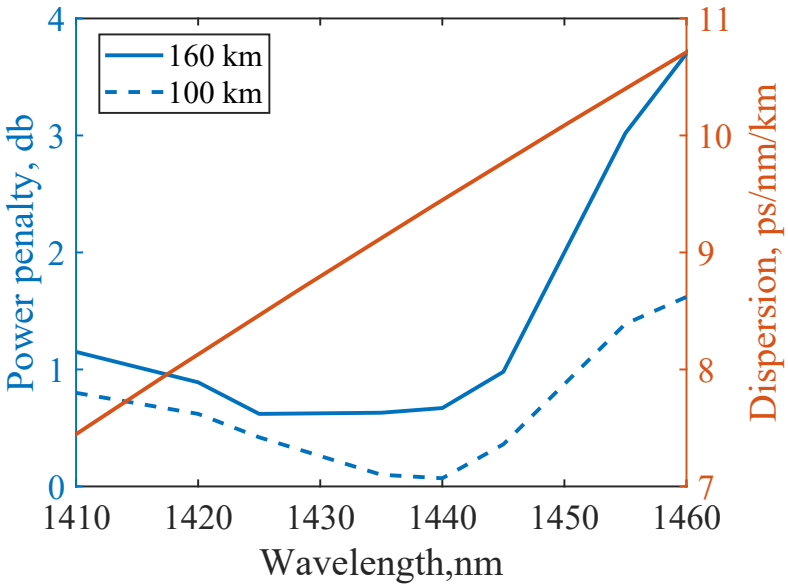

Fig. 5.11 The visual representation of the table 5.1 along with dispersion parameter of SMF.

step, a coherent detection system and experimental investigation of transmission of various modulation formats are considered.

5.3 Coherent transmission

This section is organised in a similar manner to the previous section 5.2. First, the setup of coherent transmission is presented and characterised. Then, experimental investigation of three different setups are considered. At the beginning of this investigation there had been no examples of coherent transmission in E-band enabled by BDFA.

5.3.1 Coherent optical communication system description and setup

As the first step, the coherent optical communication system should be described and important concepts of setting up the equipment for coherent transmission should be considered. The typical transmission setup for coherent detection consists of two parts: transmitter and receiver. The schematic of the used optical communication system is shown in Figure 5.12. It is clearly seen that it consists of two lines: transmitter and receiver. As it has been mentioned before, the role of the optical transmitter is to convert electrical signal into optical. In the proposed structure, the optical part of the transceiver line consists of a tuneable laser, a dual polarisation IQ modulator and an amplifier. The optical amplifier in coherent transceiver line is the crucial component due to high internal loss ($\geq$ 10 dB) of the DP IQ modulator. It

is commonly called a booster amplifier. The electrical part of the transceiver line consists of an arbitrary wave generator that generates necessary patterns for different modulation formats and a set of four digital-to-analog converters (DACs) for each polarisation and IQ components. The DACs do not only convert the digital pattern generated by AWG but also allow to correctly set the bias for each of the paths of the modulator.

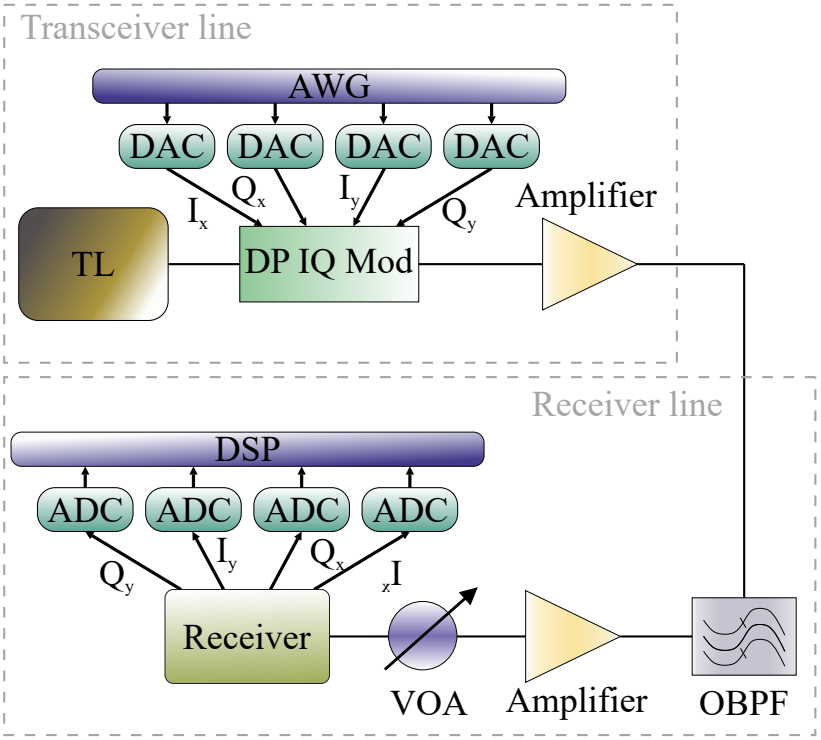

Fig. 5.12 A generic coherent optical communication system.

To understand how the DP IQ modulator works, a typical schematic of such a modulator is presented in Figure 5.13. When the optical radiation enters the optical DP IQ modulator it is split into two different polarisations with a polarisation beam splitter (PBS). As the splitting ratio of a PBS significantly varies with the polarisation of the incident radiation, it is important to keep polarisation of the incident radiation aligned to the DP IQ modulator manual. Most commonly the required input polarisation is linear as it is provided by most commercially available systems. Use of polarisation maintaining fibre connecting TL and DP IQ modulator is a key way to minimise unnecessary polarisation impairments. After polarisation splitting radiation in each of the lines passes through an equal path. First, the radiation is split again in a 50/50 coupler. Then radiation after splitting pass a Mach-Zender Modulator (MZM) for each of the polarisation I/Q components. MZMs are controlled by an individual DAC that has been mentioned earlier in the text. As the next step, the radiation in

Q path of each polarisation is rotated by 90°. After that, both I and Q paths are combined in another 50/50 coupler. As a final step, the radiation passes another PBS where it is combined.

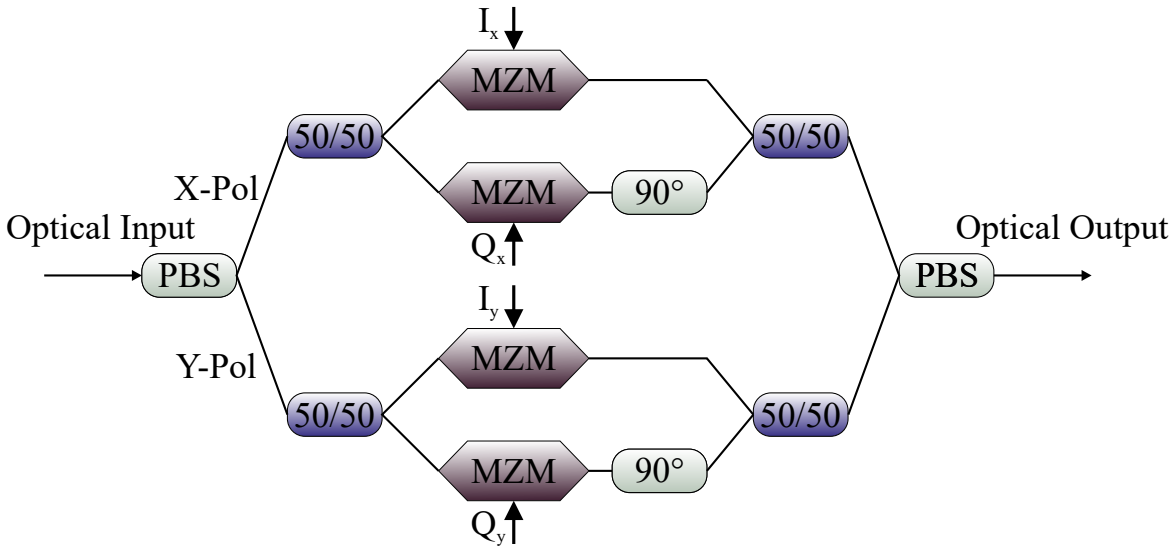

Fig. 5.13 A generic optical DP IQ modulator.

After the radiation leaves the optical DP IQ modulator it is amplified in a booster amplifier which compensates the loss of the modulator. In the back-to-back experiment the radiation is directed into the receiver line. When the transmission experiment is performed additional SMF and amplifiers are introduced between transceiver and receiver lines. The receiver line starts with the optical bandpass filter (OBPF) that filters out the data carrier channel. In the case of just one signal (without WDM grid or "dummy channels") OBPF can be extracted from the transmission line. After OBPF another amplifier is used for compensation of OBPF loss. After that, the radiation is passed through a variable optical attenuator (VOA) that is used to control the maximum power directed into the optical receiver. Generally, the input power to the receiver should not exceed 8 dBm. The schematic of a generic optical coherent receiver is presented in Figure 5.14.

The coherent optical receiver generally starts with a polarisation hybrid which consists of two inputs. One input is used for the data carrier signal, and the other one is used for the local oscillator that is used to form a beating signal with the carrier signal. The optical carrier signal passes PBS that splits the radiation into two polarisations. Each of the polarisations is directed into a 90° optical hybrid. A 90° optical hybrid is used to split radiation of the LO and the signal in such a way that the four optical outputs of the optical hybrid have the

following field distributions at the output:

$$\begin{aligned} E_1 &= \frac{1}{\sqrt{2}}(E_s + E_{LO}), \\ E_2 &= \frac{1}{\sqrt{2}}(E_s - E_{LO}), \\ E_3 &= \frac{1}{\sqrt{2}}(E_s - jE_{LO}), \\ E_4 &= \frac{1}{\sqrt{2}}(E_s + jE_{LO}), \end{aligned} \tag{5.8}$$

where E_1, E_2, E_3, E_4 are the field distributions of the output 1-4, respectively; E_s is the field of the signal, and E_{LO} is the field of the local oscillator. The radiation of four optical outputs are then directed onto two balanced photo detectors (PDs): E_1, E_2 are directed to the first balanced PD, and E_3, E_4 are combined at the second balanced PD. The balanced PD is also sometimes called differential photo detector and is used to detect small differences in optical power between two optical input signals while decreasing any unnecessary fluctuations of the inputs. The same procedure is made for the second polarisation with the help of the second 90° optical hybrid and a set of two balanced PDs. After the electrical signal is received at the output of the balanced PD, this electrical signal is sent to a set of four analogue-to-digital-converters (ADCs) for digitising of the signals of each component (see Figure 5.12). After the traces of the signal are recorded they are processed with an offline digital signal processing script described in detail in the paper by Skvortcov [124]. For further information on general DSP algorithms refer to the following papers [125, 126]. In short the DSP chain used in this work consists of the following: electrical gaussian filtering, resampling, skew estimation and compensation, signal conditioning, static chromatic dispersion estimation and compensation, coarse time synchronisation, clock recovery, polarisation derotation, preconvergance, matched filtering, fine time synchronisation, MIMO equalisation, frame parsing, frequency offset estimation, constant modulus algorithm, carrier phase estimation.

As the next step, some important notes regarding setting up of the transceiver and receiver should be made. There are several steps that one needs to follow to set up a coherent optical transmission line. The following description is fully based on the setup developed at AiPT by Dr Ian Phillips and Dr Marc Stephens. As the first step after turning on an optical receiver and transmitter and all the components of the line, one needs to correctly set the bias voltage of each of the MZMs of the optical transceiver. For this purpose, usually one of the I/Q paths of any of two polarisation states is modulated by a sine. The output of the optical transceiver

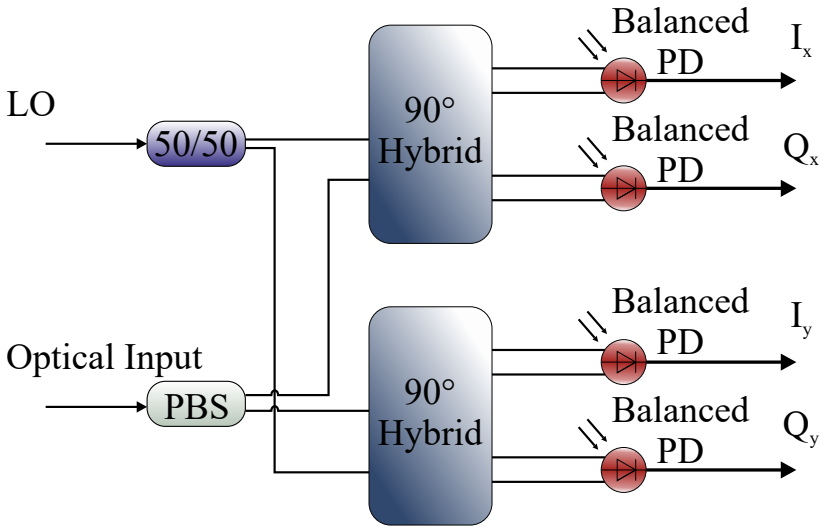

Fig. 5.14 A generic optical coherent receiver.

is then connected to the optical spectrum analyser (OSA). The optical spectrum of the data carrier modulated with a single 10 GHz sine wave is presented in Figure 5.15.

Figure 5.15 shows print screens from the OSA. The red line shows the carrier frequency. In Figure 5.15,a the spectra of the data carrier modulated with a 10 GHz sine for a modulator with incorrectly set bias is presented. One can see that the third harmonic component exists in the spectrum, indicating the wrong disposition of the bias point for a linear operation regime. The transfer function of an EOM has been shown in Figure 5.4 and the details of the operation of the EOM is presented in subsection 5.2.1. An MZM has a similar operation principle, thus it is not covered here. The spectra can help to quickly and reliably set up the bias voltage of the MZM by minimising the 3rd order harmonics that represent parasitic spectral components generated due to incorrect biasing, and, thus, such a trace represents a spectrum of an incorrect signal in time domain. After gradually setting up the bias voltage of the MZM, the spectrum of a signal should be improved to have the 3rd order harmonic minimised like shown in Figure 5.15,b. Red circles indicate the position of the 3rd order harmonics and one can notice that they are significantly suppressed. Next, the same process should be repeated for all other I/Q channels for both polarisation states.

After setting the bias correctly, another common problem that requires attention in both receiver and transceiver lines is optical and electrical deskew. Commonly, the electrical deskew of the receiver is solved using a manual for optical oscilloscope which is the key component of the receiver containing ADCs. However, to minimise optical deskew of the receiver obtained by different optical paths between 90° optical hybrids and balanced PD and path difference in 90° optical hybrid itself. Additional electrical deskew is usually produced

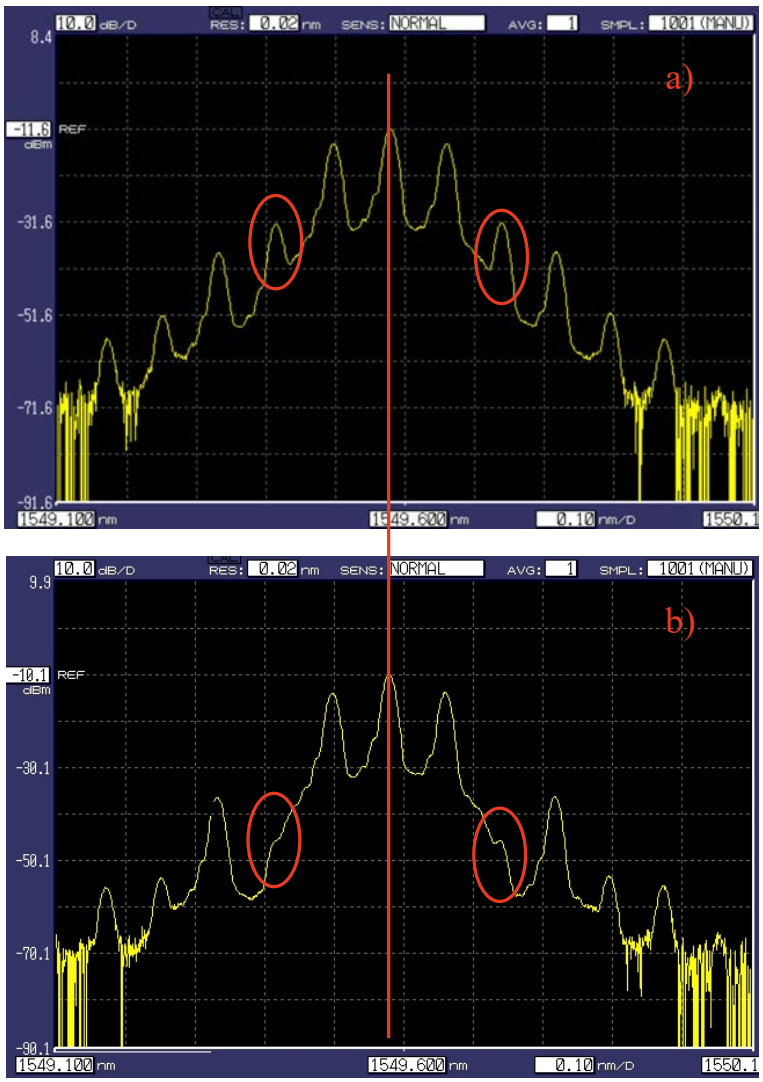

Fig. 5.15 Spectra of the data carrier modulated with a 10 GHz sine for modulator with incorrectly set bias (a); for modulator with correctly set bias (b).

in the optical transceiver due to three main factors: difference of electrical paths between AWG and DACs; difference of electrical paths between DACs and DP IQ modulator; and, finally, the delay between different boards of AWG. In the case presented here two different boards of AWG control different polarisation, thus they need to be synchronised, and the deskew between electrical signals of board 1 and board 2 should be minimised. For this purpose, the signal for all I/Q and polarisation should be replaced with single bit with a 1 and thousand or more bits of a 0. This way it is easy to find the deskew as the majority of the signal is just a constant value. After the modulation is converted into an electrical signal the output of the transceiver should be connected to the optical receiver.

Figure 5.16,a shows four traces of I_x, Q_x, I_y, and Q_y (from top to bottom) for a system with high value of deskew. It is visible that pulses of one polarisation are clearly misaligned with the pulses of the second polarisation and there are minor discrepancies between I and Q components of both polarisations. To fix this problem two approaches can be used. The first one is less precise and can only fix polarisation deskew. It is based on introducing a digital delay to one of the boards. The second approach is to use digital delay on the receiver side to make small, precise changes. Figure 5.16,b shows a signal with minor deskew that was fixed using the first approach. Additional delay values are introduced to all the channels except channel 1 which was used as a reference. After the correct delay is set and the deskew is minimised, one can move to the final step of the setting up of an optical communication link.

As the final step, a simple QPSK modulation format at 30 GBaud rate and a fast DSP algorithm can be used for final optimisation of the bias. Figure 5.17,a shows constellations for X and Y polarisation states for a QPSK signal that has high quadrature error of Y polarisation and some I and Q bias errors of X polarisation. The bias voltage should be changed to minimise the size of the constellation points of the constellation for X polarisation. The Y polarisation signal suffers from high quadrature error (tilt of the constellation). When both of the problems are fixed by changing the bias voltage and quadrature bias voltage, the clear constellations are achieved for 30 GBaud QPSK signal (Figure 5.17),b.

Generally, the deskew minimisation step can be performed once after hard reset of the setup, later only small changes to the bias voltage should be made to keep the constellation in the right form. Next, three different transmission experiments of coherent signal enabled by BDFAs in E-band are considered and discussed: 4 channel 50 GBaud SP QPSK signal transmission through 60 km; 5 channel 30 GBAud DP 16 QAM signal transmission through 160 km; 143 channel transmission of 30 GBaud DP 16 QAM in ESCL- bands, with E-band fully supported by BDFAs.

5.3.2 SP 50 Gbaud QPSK transmission through 60 km long SMF enabled by two BDFAs

The first out of three experiments of coherent transmission enabled by BDFA is single polarisation 50 GBaud QPSK transmission through 60 km long SMF enabled by two BDFAs. In this experiment, the amplifier from subsection 4.2 is used as a receive amplifier, and the amplifier from section 4.3.1 is used as a booster amplifier. The experimental setup is presented in Figure 5.18. The output optical signal from the TL operating in the spectral range from 1340-1480 nm is modulated with a 50 Gbaud SP-QPSK signal by the I-Q modulator. This signal will be referred to as data carrier channel later in the text. The booster BDFA is

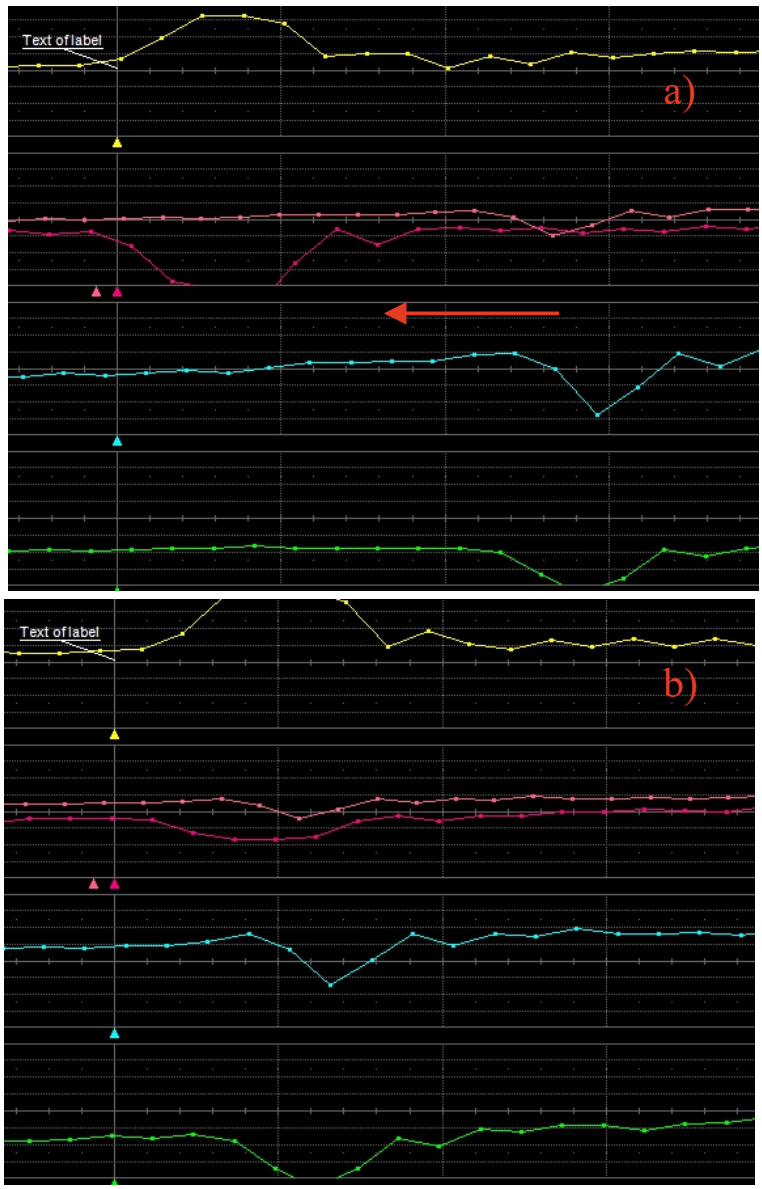

Fig. 5.16 Oscilloscope traces of I_x, Q_x, I_y, and Q_y (from top to bottom) for a system with high value of deskew (a) and for a system with low level of deskew (b). Red arrow shows the direction where the signal of Y polarisation should be moved to minimise deskew.

used to amplify the data carrier channel due to the high internal loss of the I-Q modulator (14 dB). The specifics of the I-Q modulator is discussed in subsection 5.3.1. It is important to note that in this section on single polarisation transmission is presented due to temporal problems related to the transmitter and receiver polarisation skew. The methodology for how to cope with this problem is also described in subsection 5.3.1. The booster amplifier is based on the BDFA from subsection 4.3.1 that operates with only the forward LD with 300 mW

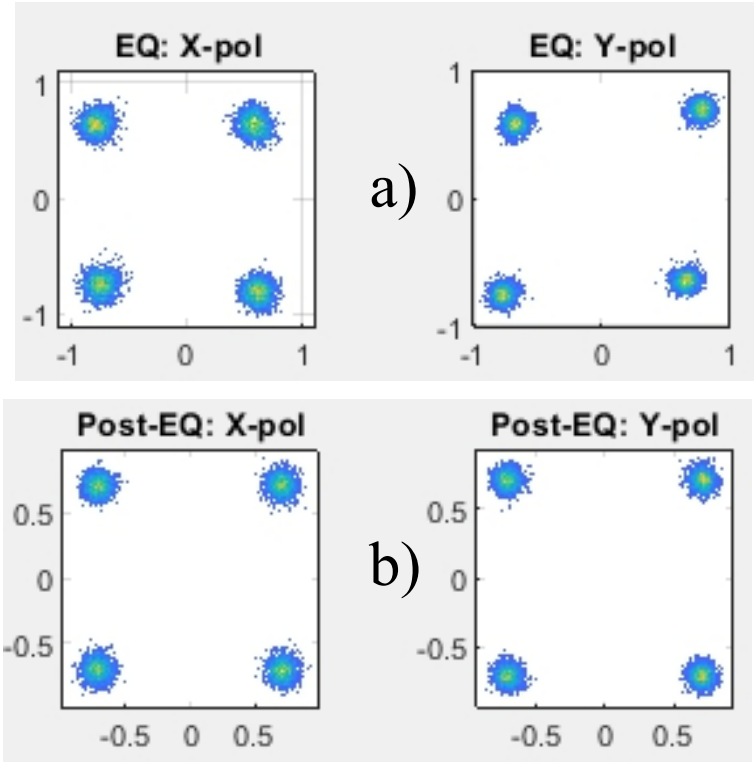

Fig. 5.17 a) Constellations for X and Y polarisation states for QPSK signal that has high quadrature error of Y polarisation and some I and Q bias errors of X polarisation; b) constellations for X and Y polarisation states for QPSK signal that has low quadrature error, and I and Q bias errors.

power to allow low NF discussed in subsection 4.3.1 and paper [63]. The detailed description of this amplifier is not presented here as it has already been covered in subsection 4.3.1. A VOA is used to adjust the power of the data carrier to that of the "dummy" channels. Next, the data carrier signal is combined with an optical signal of the continuous wave laser diodes in a 3 dB optical fibre coupler. The optical signal of four laser diodes operating at the wavelengths of 1410, 1430, 1450, and 1470 nm is combined in a multiplexer (MUX) and forms "dummy" channel signals. The total input signal power before the SMF is 8 dBm. The transmission line is comprised of a 60 km long span of SMF, followed by another BDFA. The receive BDFA has a bi-directional pumping scheme with total 700 mW pump power of two pump laser diodes at 1320 nm to enable high gain and low NF operation. It is also the amplifier extensively covered in subsection 4.2 and paper [63]. Figure 5.18 also shows the input spectrum before the SMF and the output spectrum after the receive BDFA. Both spectra are recorded from -20 dB coupler output. An OBPF at the receive side is used for filtering out the signal. Due to sufficient gain of the amplifier (see Figure 5.19,a) no additional amplifier is required in the receive line and another VOA is used to limit the signal to less than 6 dBm.

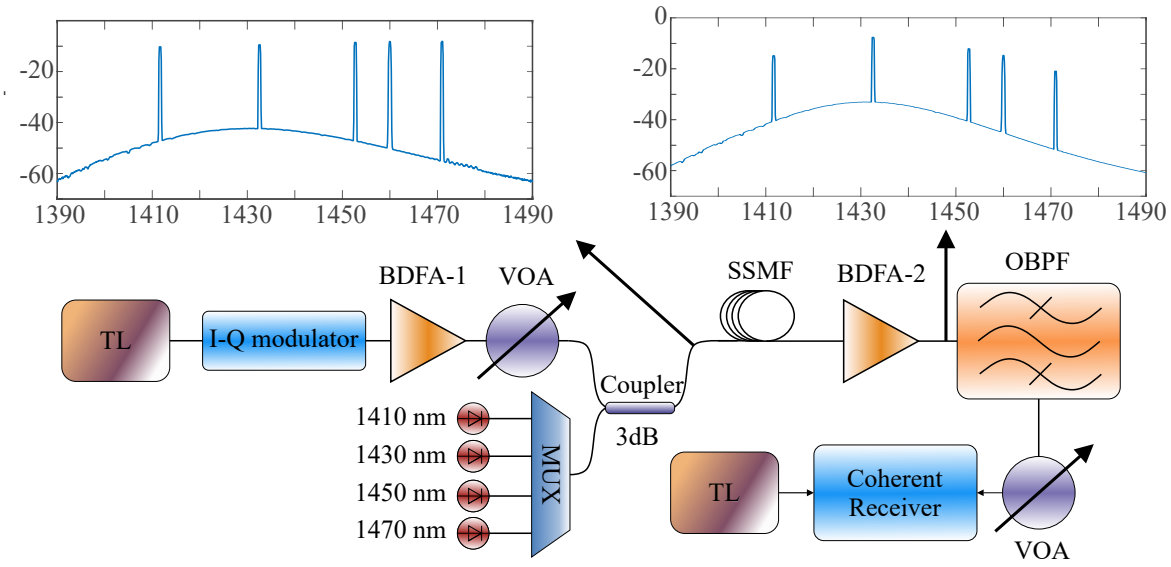

Fig. 5.18 Setup of coherent transmission of SP 50 GBaud QPSK signal through 60 km of SMF and BDFA. Input and output spectra from -20 dB coupler output are presented at the top. BDFA-1: Booster BDFA; BDFA-2: receive BDFA.

After VOA, the signal passes to the coherent receiver where the signal is received with an 80 GSa/s, 36GHz bandwidth oscilloscope and processed by an offline digital signal processing, as described in further detail in paper [124].

The gain and NF of the developed amplifier are measured by the methodology described in Subsection 4.1.2 and are presented in Figure 5.19,a. However, during the gain and NF measurement "dummy channels" are kept in the transmission to keep the conditions of operation as close to the transmission experiment as possible. The amplifier features a maximum gain of 29.8 dB with a 3 dB bandwidth of 35 nm for -15 dBm signal power. The NF is as low as 5 dB and does not exceed 6.25 dB.

The transmission performance of the 50 Gbaud SP-QPSK signal is measured every 5 nm from 1415 nm to 1450 nm, except 1445 nm. Due to unavailability of an additional TL that could be used for the local oscillator at 1445 nm, the measurement at this wavelength is skipped. Even though tunable sources are available outside the 1415-1450 nm range, measurements beyond the specified spectral region are not possible due to insufficient gain of the receive BDFA. First, the back-to-back Q^2 factor of the transreceiver setup is measured at the desired wavelengths and is shown in Figure 5.19,b with black squares. This measurement is performed without the 60 km SSMF span and the receive BDFA. The average Q^2 factor in the operating range is around 18 dB and has a very flat performance in the spectral range from 1415 to 1440 nm. The decreased performance at 1450 nm can be explained by a limitation of the power of the LO that was only 3 dBm in comparison to 10 dBm for all other wavelengths.

In the following subsections this dip no longer exists due to an improved setup that allows a consistent power of LO at all wavelengths (see subsection 5.3.3 and subsection 5.3.4).

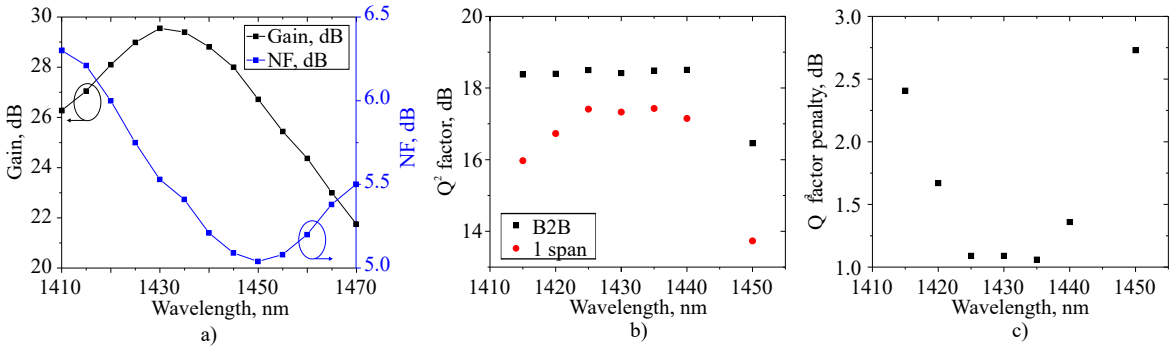

Fig. 5.19 a) Spectra of the gain and NF of the receive BDFA; b) Spectra of Q^2 factors for B2B and single span measurements for SP-QPSK signal; c) Spectrum of the Q^2 penalties for SP-QPSK signal; d) SP-32-QAM constellations for B2B measurement (top) and single span transmission measurement (bottom).

The spectrum of the Q^2 factor after a single span of SSMF and BDFA amplification is presented in Figure 5.19,b with red circles and is well above the HD-FEC limit of 8.5 dB for QPSK. However, it shows a more significant spectral dependence than the B2B performance which should be addressed. The Q^2 factor penalties are presented in Figure 5.19,c showing < 2 dB penalty in the spectral range 1420-1440 nm. The penalty increase at the edges of the measurement corresponds to increased NF in these spectral regions. It is important to highlight that the experiment is conducted using a trans-receiver system designed for operation in C- and L-bands. The measurements are conducted without the use of any extra recently reported techniques, such as nonlinear transmitter pre-distortion, that can substantially improve the transmission performance in the E-band with the use of conventional C+L equipment [127, 128]. In general, the penalty in the E-band is mainly attributed to the low OSNR of the transmitted SP-QPSK signal due to imperfections of the transreceiver system, and I-Q imbalance that are explained in aforementioned works. Nevertheless, the output signal quality allows to achieve error-free transmission in the 1415-1450 nm spectral band. The achieved results show a potential for BDFAs to be used for transmission of higher order modulation format, transmission on longer distances (by using more BDFAs with more pump power) and its use in multi-band transmission networks. In the next step, a longer distance transmission with higher modulation formats case is considered.

5.3.3 DP 30 GBaud 16 QAM transmission through 160 km long SMF enabled by 3 BDFAs

In this next step the 5 channel transmission of DP 30 GBaud 16 QAM through 160 km long SMF enabled by 3 BDFAs is considered. The results here are the record transmission length for the coherent detection signal achieved in the E-band and one of the first coherent transmission demonstrations enabled by a fully BDFA supported system [70, 85]. The experimental setup of DP 30 Gbaud 16 QAM 5 channel transmission through 160 km of SMF is presented in Figure 5.20,a. The coarse wavelength division multiplexing (CWDM) grid consists of four "dummy" channels at 1411 nm, 1431 nm, 1451 nm, and 1470 nm. The number of channels is limited by component availability rather than the fundamental BFDA design as has been mentioned before. The data carrier signal is generated using a TL operating from 1410 to 1460 nm in this experiment. The radiation of the TL is modulated by a dual-polarisation IQ modulator (DP IQ Mod) driven by a DAC to achieve DP 30 GBaud 16 QAM modulation. The details of the transceiver are presented in subsection 5.3.1. The signal after the modulator is amplified by the booster amplifier which is based on the setup described in subsection 4.3.2. For the power equalisation of the data channel with the CWDM grid, a VOA is used ahead of a 90/10 coupler. In the case of back-to-back (B2B) transmission the signal after the coupler is directed to an OBPF, where the data carrier signal is filtered from "dummy" channels. When the 160 km transmission is performed, the signal is directed into another VOA that is used for total input power control (before the transmission line). After the VOA, the signal is transmitted through a 80 km-long SMF, amplified by the in-line BDFA (based on the amplifier described in subsection 4.3.1) and transmitted through another 80 km long SMF. In both cases, after the data carrier filtering, the signal is amplified by the receive amplifier (the amplifier described in subsection 4.2). The input power to the coherent receiver is controlled by another VOA, and an external tunable laser operating from 1410-1460 nm is used as a local oscillator for the coherent detection system. Channel reception is completed by a standard set of 80 GSa/s, 36 GHz ADCs. The transceiver setup used for the coherent detection in this work is described in detail in subsection 5.3.1. The DSP chain used for analysis of the received signal has been previously described in detail in [124] and mentioned in subsection 5.3.1.

The spectra of the signal channels at the different critical points of the transmission line are presented in Figures 5.20,b-e. Figure 5.20,b shows the spectrum of the channels at the input to the transmission line. The signal at 1440 nm is a data carrier. It has a lower power level at the spectra due to higher bandwidth of the signal in comparison to the bandwidth of the "dummy" channels, thus the average power per channel is kept the same for all the channels. Figure 5.20,c shows the signal after transmission through the 80 km-long SMF.

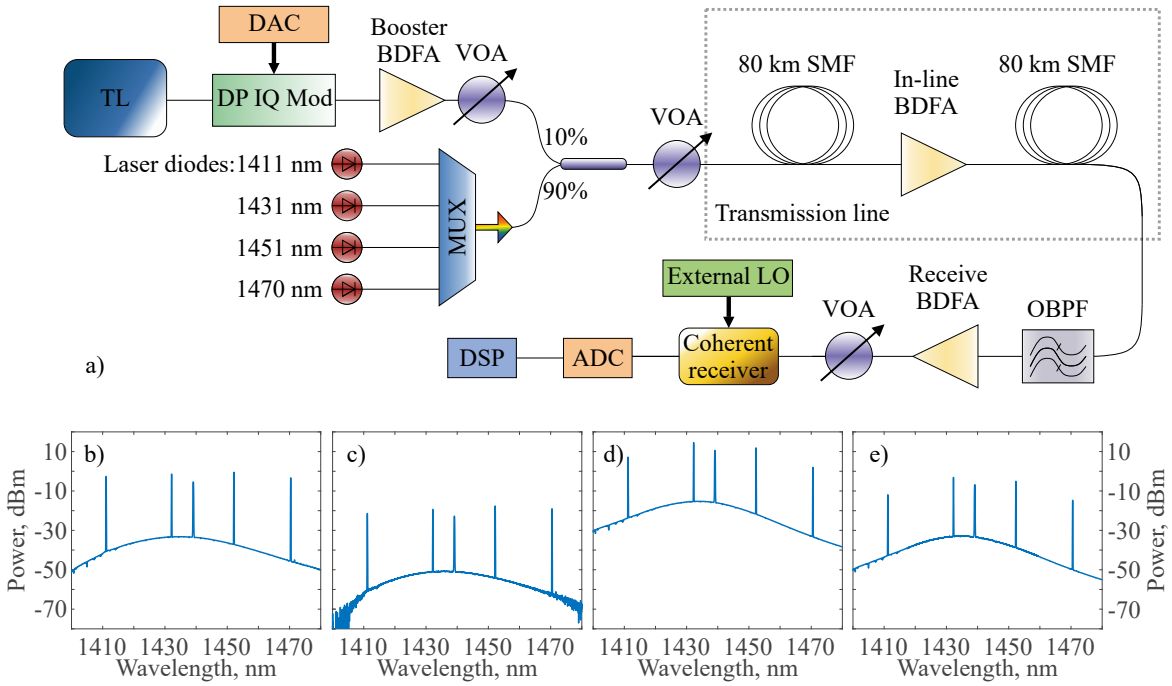

Fig. 5.20 a) The experimental setup of E-band 5 channel DP 30 Gbaud 16 QAM transmission through 160 km SMF; The spectrum of the signal at the input to the transmission line (b), after 80 km-long SMF (c), after the in-line amplifier (d), at the output of the transmission line (e).

The intrinsic loss of the SMF is slightly higher at lower wavelengths, thus it leads to the development of a tilt in the spectrum. The signal after the in-line BDFA is presented in Figure 5.20,d. Amplification with the BDFA further distorts the spectrum due to bell-like shape of the BDFA. After the amplification in the in-line BDFA the signal is transmitted through another 80 km-long SMF and the signal spectrum at the output of the transmission line is presented in Figure 5.20,e. Another span of SMF introduces extra attenuation of the signal and further distorts the signal spectrum.

The schematic depiction of the used amplifiers is presented in Figure 5.21. All of the amplifiers are optimised in terms of best performance of gain and NF using different pump diode wavelengths based on the procedure described in subsection 4.4 . Each of the amplifiers consists of active BDF, two isolators for unidirectional propagation of the signal, and two TFF-WDMs for signal and pump radiation multiplexing. A set of pump diodes is used for each amplifier to allow the best performance in terms of gain and NF. As only a limited amount of pump laser diodes is available for BDFAs optimisation, the choosing of the pumps is performed to achieve overall best performance with the following priority: in-line amplifier, booster amplifier, receive amplifier. The booster BDFA is presented in Figure 5.21,a. It is based on the 153 m-long piece of germanosilicate BDF described in subsection 4.3.2. The

1260 nm (forward) and 1330 nm pump (backward) allow to achieve the lowest NF of 4.8 dB and the highest gain of 27.3 dB in the setup.The maximum total pump power is 900 mW in this experiment. The spectra of gain and NF of the booster BDFA are presented in Figure 5.21,b. The BDFA also has a 46 nm 3 dB bandwidth.

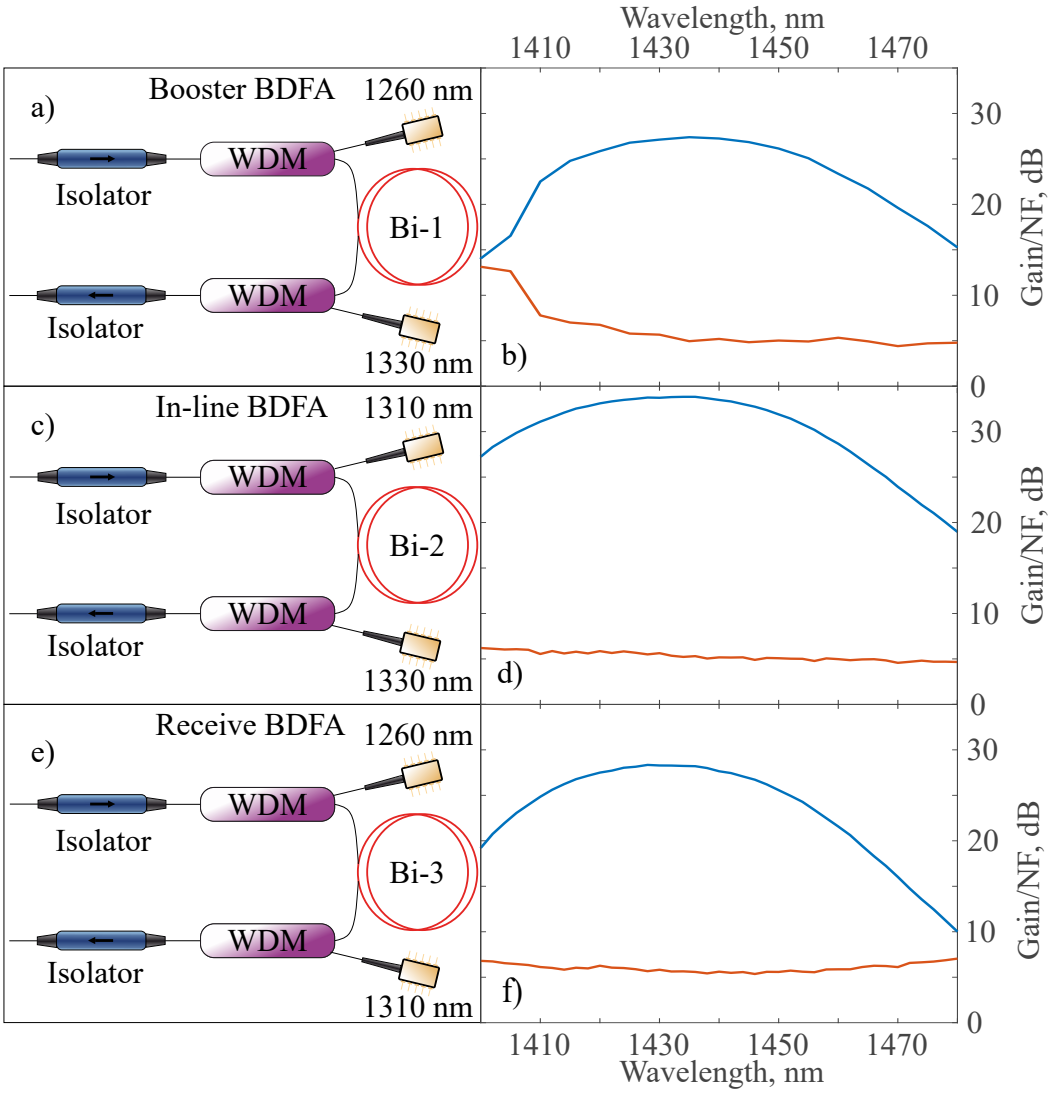

Fig. 5.21 The schematic of booster BDFA (a), in-line BDFA (c), receive BDFA (e); Spectra of gain and NF of three amplifiers: booster BDFA (b), in-line BDFA (d), receive BDFA (f).

The in-line amplifier has the same schematic as the booster amplifier, however, it is based on the fibre described in subsection 4.3.1. The pump laser diodes used for this setup are 1310 nm (forward) and 1330 nm (backward) pump diodes with total 900 mW pump power. These diodes are used for bi-directional pumping of the fibre. The Bi-doped fibre is manufactured to have the same geometric characteristics as the fibre of the booster, however, it is made of a

different preform and has a length of 173 m. This amplifier has a maximum gain of 33.8 dB and the achieved NF is the lowest and is equal 4.7 dB in comparison to the booster BDFA. The spectra of gain and NF of the in-line BDFA are presented in Figure 5.21,d. Moreover, the 3 dB bandwidth is also the highest of all three amplifiers and is equal 50 nm.

At last, the schematic of the receive amplifier is presented in Figure 5.21,e. It is based on the 300 m long fibre which is presented in [63] and in subsection 4.2. The fibre has the following characteristics: the core is 9 μm. The numerical aperture (NA) is 0.14, and the cutoff wavelength is around 1.2 μm. The 1260 nm pump diode is used for forward pumping and the 1310 nm pump diode is used for backward pumping. The amplifier has the maximum gain of 28.3 dB, minimal NF of 5.3 dB, and 42 nm 3 dB bandwidth. The spectra of both gain and NF are presented in Figure 5.21,f.

As all amplifiers have different performance, the choice of the amplifier for each of the position in the setup was made based on the following criteria. To begin with, the in-line amplifier was assigned: the amplifier with the highest gain and the lowest NF. Parameters of this amplifier are especially important in multi-span or transmission loop measurements. Next, the booster amplifier was chosen to have low NF and high enough gain to have sufficient signal power at the input to the line. It is important to have low noise amplifier at the input of the line, as SNR degrades quicker the higher the input noise is. Finally, the last amplifier was assigned as a receive BDFA.

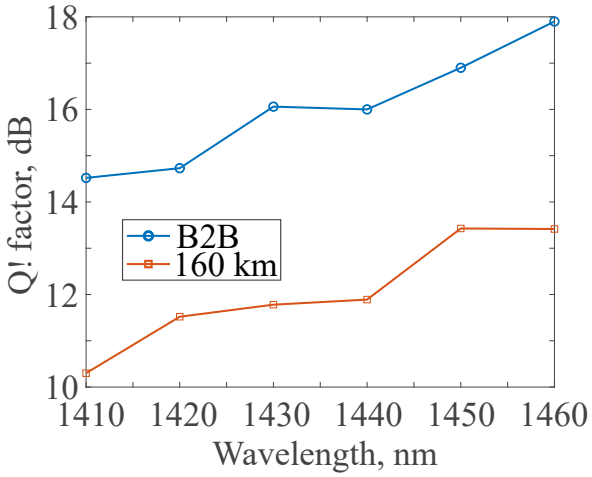

Fig. 5.22 The spectra of the Q^2 factor for back-to-back case (blue line with circles) and transmitted signal (orange line with squares).

To perform the measurements across the desired spectral band the operation wavelength of the input TL and the external LO TL are tuned accordingly. In this work, the six wavelengths are experimentally characterised: 1410, 1420, 1430, 1440, 1450, and 1460 nm. After the wavelength is tuned, the first step is to perform the back-to-back measurement. The

dependence of the Q^2 factor on wavelength for the back-to-back case is presented in Figure 5.22 (blue line with circles). After the measurements of the back-to-back performance the transmission line is assembled. The power at the input to the transmission line is controlled with a VOA to allow studying the performance at different input powers per channel. The dependence of the Q^2 factor on the input power per channel for all six wavelengths under test are shown in Figure 5.23.

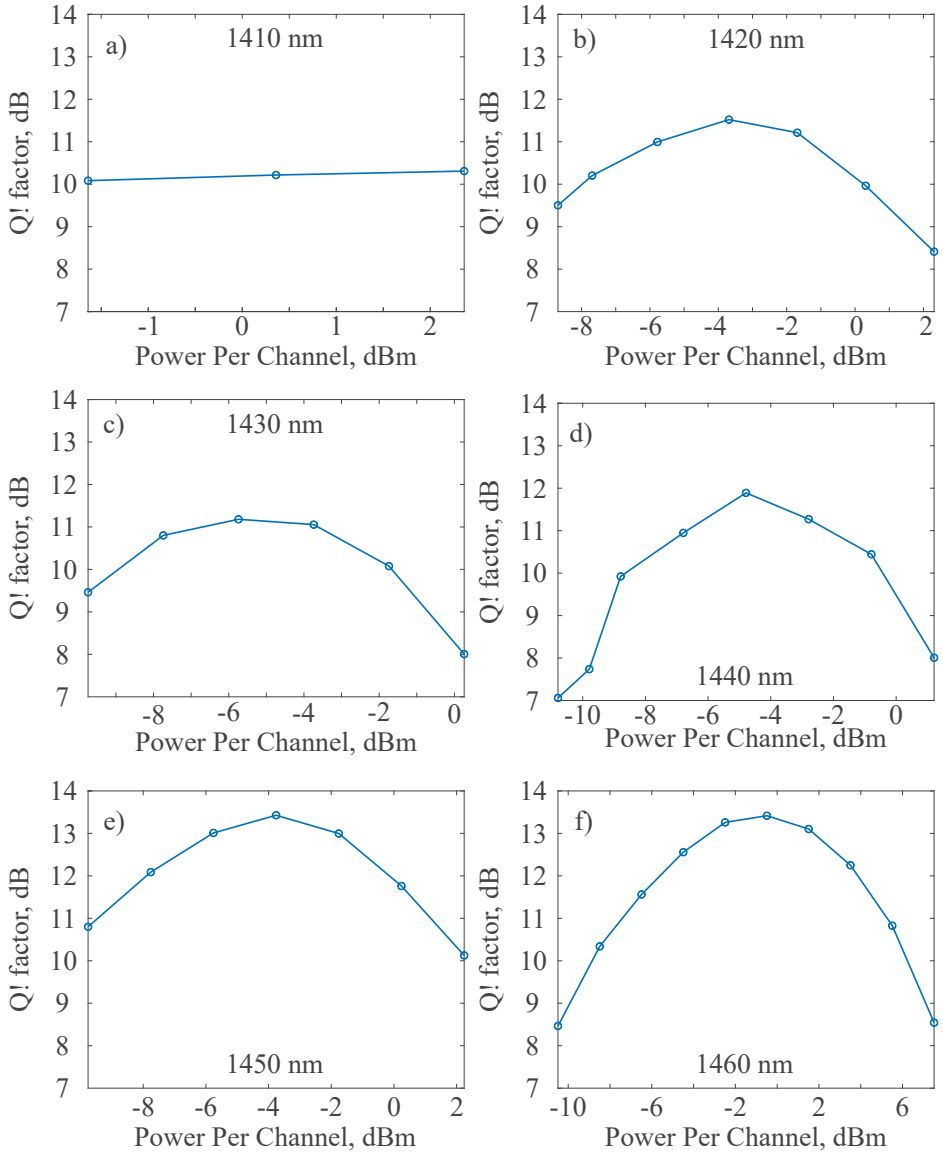

Fig. 5.23 The dependencies of the Q^2 factor of the transmitted signal on the input power per channel at 1410 nm (a), 1420 nm (b), 1430 nm (c), 1440 nm (d), 1450 nm (e), 1460 nm (f).

Generally, the change of the Q^2 factor with the input power per channel has the following pattern: the Q^2 factor grows with an increase of input power per channel until an optimal

level is achieved (the input power per channel with the highest Q^2 factor achieved for this wavelength); after the optimal level, the Q^2 factor decreases with the increase of the input power per channel due to the nonlinear effects that lead to increased nonlinear signal distortion. The Q^2 factor dependence on the input power per channel at 1410 nm is only recorded within linear regime before an optimal point due to the power limitations (not high enough gain of all amplifiers and increased intrinsic loss of the SMF fibre in the lower wavelength region due to water peak absorption). All measurements (except the one at 1410 nm) are performed to determine the optimal input power per channel for this particular transmission setup. The input power per channel is calculated from the recorded spectra and power meter measurements at the input to the transmission line. The spectra are used to calculate a portion of the input power dedicated to the data carrier channel. The optimal input power per channel is around -4 dBm for 1420 nm, then it decreases up to -6 dBm for 1430 nm, then it goes up to -5 dBm, -4 dBm, and 0 dBm for 1440 nm, 1450 nm, and 1460 nm, respectively. Such a substantial variation of the optimal input power per channel for all the wavelengths can be explained by several factors: non flat gain and different additive noise of the amplifiers, increased loss and decreased nonlinearity of SMF on the left hand side of the spectrum.

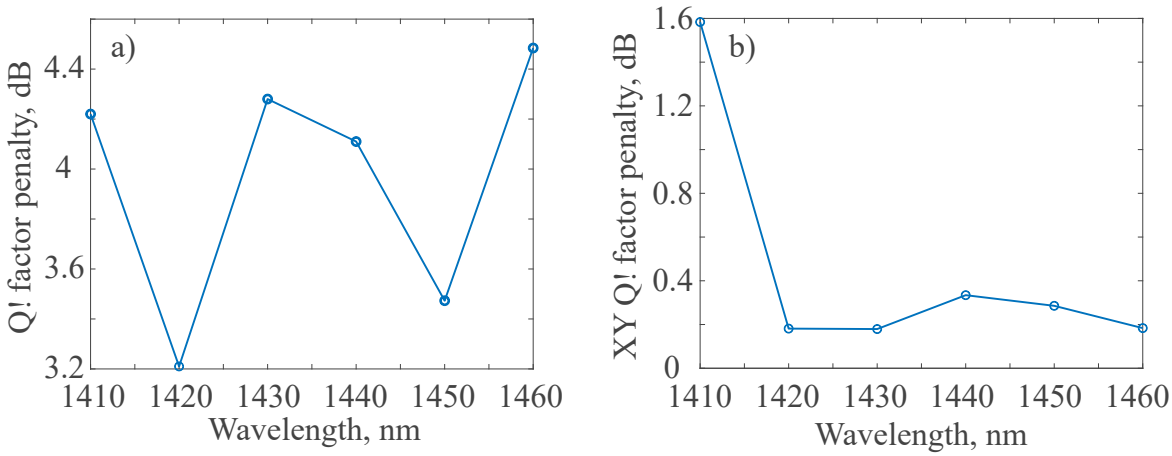

Fig. 5.24 a) Spectra of Q^2 factor penalty between back-to-back and transmission over 160 km of DP 30 GBaud 16 QAM channel; b) spectra of the polarisation Q^2 factor penalty.

As the next step, the back-to-back performance of the setup is compared to the transmission results. The dependence of the Q^2 factor at the optimal input power per channel on the wavelength is presented in Figure 5.22 as the orange line with squares. Both B2B and 160 km transmission performance follow a similar trend: a significant degradation of the performance towards lower wavelengths. The difference between the back-to-back and transmission performance (Q^2 factor penalty) is presented in Figure 5.24,a. Both back-to-back

and transmission performance are improved with the increase of the wavelength of the signal (Figure 5.22). This can be mostly explained by the fact that a C-L optical transceiver and receiver have been used in this work and worse NF performance of the amplifiers at the lower wavelengths. The problem of performance degradation of C+L equipment in S-band and beyond has been addressed in the following papers by Emmerich [129] and di Rosa [130]. Mostly, such degradation can be explained by an I/Q imbalance of the optical transceiver at lower wavelengths and both I/Q and polarisation imbalances of the optical hybrid used in the experiment.

The polarisation imbalance (difference between average X and Y Q^2 factor values at each wavelength) is recorded in terms of Q^2 factor penalty between X and Y components and is presented in Figure 5.24,b. There is a significant increase of the impairment at the 1410 nm signal wavelength. This can be explained by limitations of the used optical hybrid optimised for operation in C+L bands. As an improvement to the setup for future experiments it is possible to use tunable optical hybrids whose performance can be adjusted for better performance in different optical bands. To achieve almost error-free transmission a specific level of the BER should be achieved in the setup pre-FEC, and, generally, measurement of the pre-FEC BER is enough to predict post-FEC BER. The $2.7 * 10^{-2}$ pre-FEC BER corresponding to the 5.7 dB Q^2 factor is achieved for all powers and wavelengths in the experiment. This pre-FEC BER has been shown to be corrected to 10^{-15} and below using soft-decision FEC with 20% overhead [131].

Finally, it is important to discuss the results of the Q^2 factor penalty achieved in the E-band. The maximum penalty is 4.5 dB at 1460 nm and the lowest penalty is 3.2 dB at 1420 nm. There is no clear tendency of the Q^2 factor penalty dependence on wavelength in E-band due to the complexity of the system and a big number of factors that impact the performance of the setup in their own way. However, it is insightful to address the impacts of various factors at different wavelengths. First of all, the shorter wavelength region suffers from high optical loss, relatively low gain, high NF and the increased polarisation or I/Q imbalance. it should be noted, that the OSNR of the signal at the output of the amplifier is determined not only by the NF but also by input signal (lower input signal leads to lower OSNR). Thus, if we have higher loss and smaller signal at the input to the amplifier, the output OSNR will be lower. Longer wavelengths feature both increased dispersion and low gain. However, the impact of the dispersion in relative short coherent detection systems are negligible. On the other hand, transmission in this region benefits from lower loss, NF, and transceiver-receiver induced penalties. The dominating factor for an increased penalty in the region of 1430-1440 nm is, perhaps, nonlinearity due to increased gain and Kerr nonlinearity in this region. The use of a gain-flattening filters might potentially improve the performance

of the transmission line by significantly decreasing the nonlinearity in the 1430-1440 nm range. However, the BDFAs should potentially be improved more in terms of NF at the lower wavelengths ($<$ 1430 nm). Another potential factor contributing to the performance of the system at shorter wavelengths is the responsivity of the photodiodes. The responsivity of the photodiodes used in this work were not measured, however, they are made of InGaAs, and the typical values of responsivity of the InGaAs photodiodes can be used [123]. Such photodiodes' responsivity typically falls down from the C-band toward lower wavelengths. The typical responsivity of the InGaAs is presented in Figure 5.7. Next, let us consider a case of wideband transmission using both BDFA and Raman amplifiers as in-line amplifiers and compare the performance of the optical transmission line in the E-, S-, C-, and L-bands.

5.3.4 Wideband DP 30 GBaud 16 QAM transmission through 70 km long SMF enabled by hybrid Raman and BDFA

The schematic of the ESCL-band amplifier is presented in Figure 5.25. It comprises two separate optical paths, with a BDFA operating in the E-band and a dual-stage DRA operating in the SCL-bands. These bands are separated by a filter WDM (FWDM), with transmission and reflection bands of 1410-1457 nm and 1470-1620 nm. After band-splitting, the E-band signal follows the upper path in Figure 5.25 passing via an isolator to a 300 m long Bi-doped fibre that is bi-directionally pumped via a pair of WDM couplers by two pump diodes at 1260 nm (forward) and 1310 nm (backward). Additionally, two isolators are used to ensure unidirectional propagation of the signal. The Bi-doped fibre used in this paper is the one reported in [63]. The SCL-band signal follows the lower path in Figure 5.25 where the first stage of the amplifier targets S-band amplification, and consists of an isolator, a 7.5 km-long inverse dispersion fibre (IDF), a WDM, a pump combiner and three pump diodes at 1365 nm, 1385 nm, and 1405 nm. The second stage amplifies the C- and L-bands and consists of the same set of components with the exception of the pump combiner and pump laser diodes at 1425 nm, 1445 nm, 1464 nm, 1485 nm, and 1508 nm [31]. Finally, both amplified signals are combined with 1410-1457nm/1470-1620nm FWDM. The Raman amplifier presented here is a result of the work of my fellow PGR student and colleague Mr Pratim Hazarika, thus, this amplifier is discussed in details in his thesis work.

The measured gain and noise figure (NF) of the amplifier are presented in Figure 5.26, showing a maximum gain of 18 dB and a minimum NF of 5.9 dB. The E-band BDFA was pumped at only 200 mW to enable matching gain with the DRA. The reduced gain at 1460 nm is explained by the lower efficiency of the BDFA in this region at this relatively low pump power level. The minimum of the NF is at 1450 nm which corresponds well with the

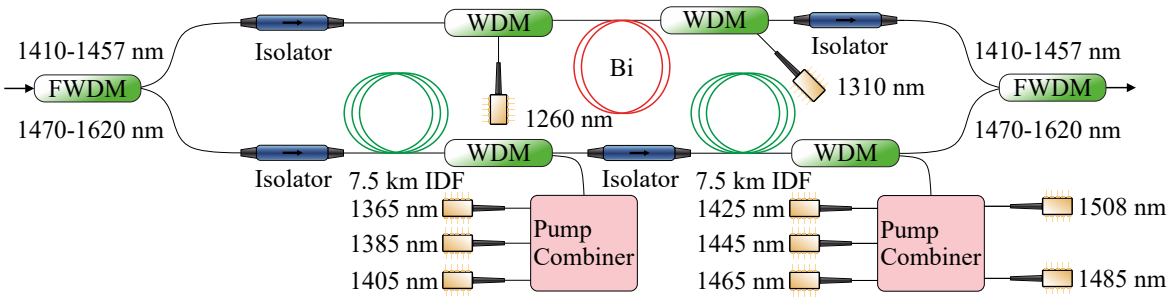

Fig. 5.25 Experimental setup E-,S-,C-,L-band amplifier enabled by active Bi-doped fiber and discrete Raman amplification.

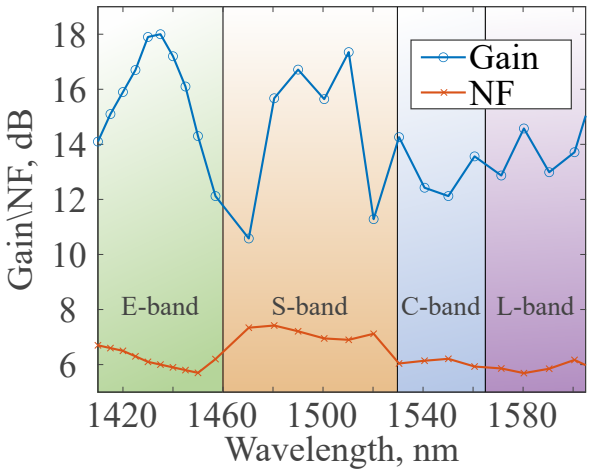

Fig. 5.26 Gain and NF spectra of the developed hybrid E-,S-,C-,L-band amplifier enabled by active Bi-doped fiber and discrete Raman amplification.

behaviour reported previously [63]. The DRA has increased gain in the S-band except gain in vicinity of 1470 nm and 1520 nm due to high attenuation values, inter-stimulated Raman scattering (ISRS) power transfer to the C and L band signals, and limitations of the pump. The NF was found to be lowest in the C-band with a minimum value of 5.9 dB NF. The DRA has a flat gain (with variations less than 3dB) from 1520 nm to 1605 nm with an average gain of 13 dB covering the entire C and L bands.

The setup of the data transmission experiment is presented in Figure 5.27. The E-, S-, C-, L-band WDM grid consists of 143x100 GHz ASE-emulated channels in the S-, C-, and L-bands, plus three E-band laser diodes at wavelengths of 1411 nm, 1432 nm, and 1451 nm (see Figure 5.28,a,b,c). The S-band channels (1470-1520 nm) are generated using a supercontinuum source and a commercial wavelength selective switch (WSS) for channel spacing and flattening followed by a thulium doped fibre amplifier (TDFA). There are also two guard bands of 4 nm and 6 nm around each of the longest wavelength pumps at 1485 nm and 1508 nm, respectively. The S-band channels are combined together with a flat

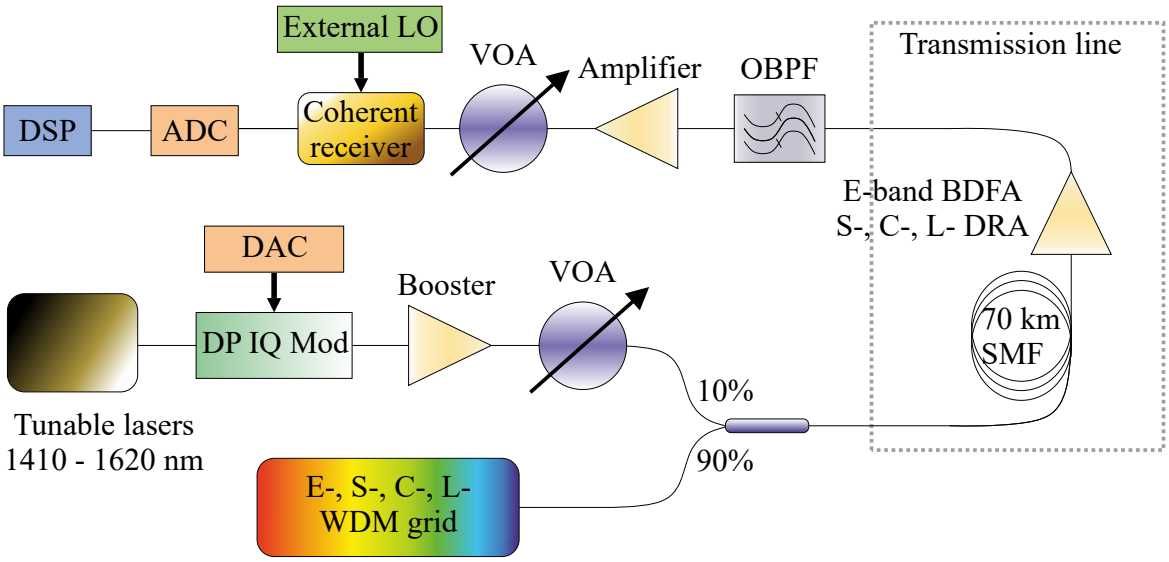

Fig. 5.27 Experimental setup of a B2B and transmission experiment.

channelised C and L-band ASE noise extending out to 1608 nm, generated using C and L-band EDFAs and two WSSs for equalisation and flattening.

The data carrier signal is generated using different tunable lasers operating from 1410 to 1605 nm, which are modulated by a dual-polarisation IQ modulator (DP IQ Mod) driven by a digital-to-analog converter (DAC) to achieve a 30 GBaud 16 QAM signal. The signal after the modulator is amplified by a booster amplifier (in-house BDFA for E-band, commercial TDFA for S-band, and commercial EDFAs for C- and L-bands). For power equalisation of the data channel with WDM grid, a variable optical attenuator (VOA) is used ahead of a 90/10 coupler.

As the WDM grid is dense in S-,C-,L- bands, the WDM channel corresponding to the data carrier signal is turned off by WSS to avoid channel overlap. In the case of back-to-back (B2B) transmission the signal then is directed to an optical bandpass filter (OBPF), where the data carrier is filtered. When the transmission is performed, the signal is directed into a 70 km-long SMF-28 fibre and then amplified by the developed hybrid MB amplifier. In both cases, after the data carrier is filtered by OBPF it is amplified by an appropriate receive amplifier, similarly to the booster. The input power to the coherent receiver is controlled by another VOA, and a set of external tunable lasers operating from 1410-1605 nm is used as a local oscillator for the coherent detection system. Channel reception is completed by a standard set of 80 GSa/s analog-to-digital converters (ADCs). The digital signal processing (DSP) chain used for analysis of the received signal has been described previously [124].

The recorded results of the transmission experiment are presented in Figure 5.29. The wavelength dependence of the Q^2 factor of a DP 30 GBaud 16 QAM signal is recorded

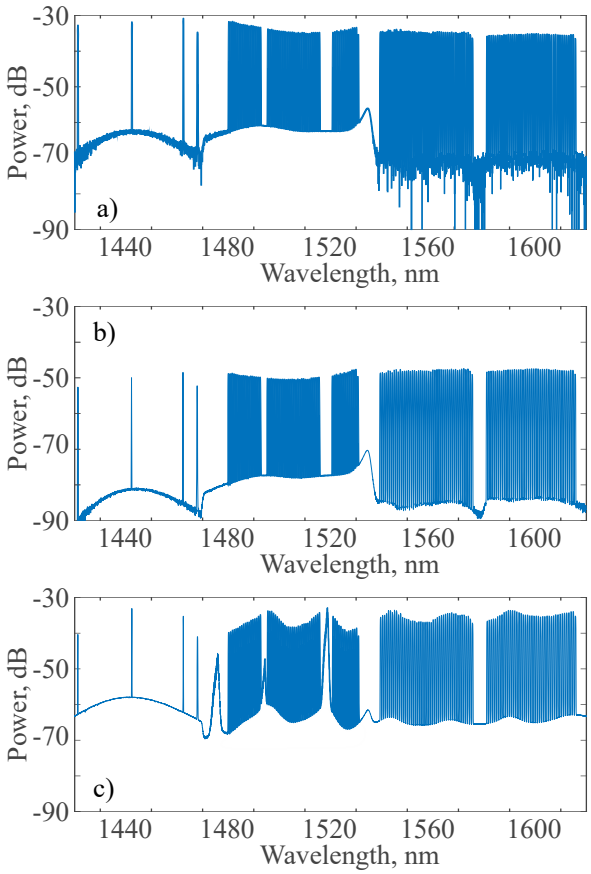

Fig. 5.28 Spectra of the WDM grid and E-band data carrier signal at 1457 nm at (a) input to the span, (b) end of the span, (c) after the amplifier.

by tuning the wavelength of the tunable lasers (signal and local oscillator) across 195-nm bandwidth from 1410 to 1605 nm. The wavelength dependencies of the Q^2 factor (average between X and Y) for B2B and 70 km-long transmission are presented in Fig. 5.29,a. The Q^2 factor was calculated from the signal-to-noise ratio obtained from the recovered constellations [120].

The transmission performance of the DRA in the L-band features a Q^2 factor penalty no higher than 2.2 dB and the lowest Q^2 factor penalty for the whole DRA of just 1 dB (see Figure **??**,b). The C-band shows the best B2B performance achieved in the experiment enabled by commercial EDFAs. The DRA has the maximum Q^2 factor penalty of 1.7 dB in this region. The B2B performance in the S-band shows similar performance to the L-band. However, a noticeable decrease of the S-band B2B performance at around 1470 nm is due to the relatively high NF of the TDFA in this region. The performance of the DRA in the S-band has a maximum penalty of 3.3 dB and the minimum of 2 dB. The substantial increase

of the Q^2 factor penalty at 1470 nm can be explained by the high NF of the DRA at this wavelength of operation.

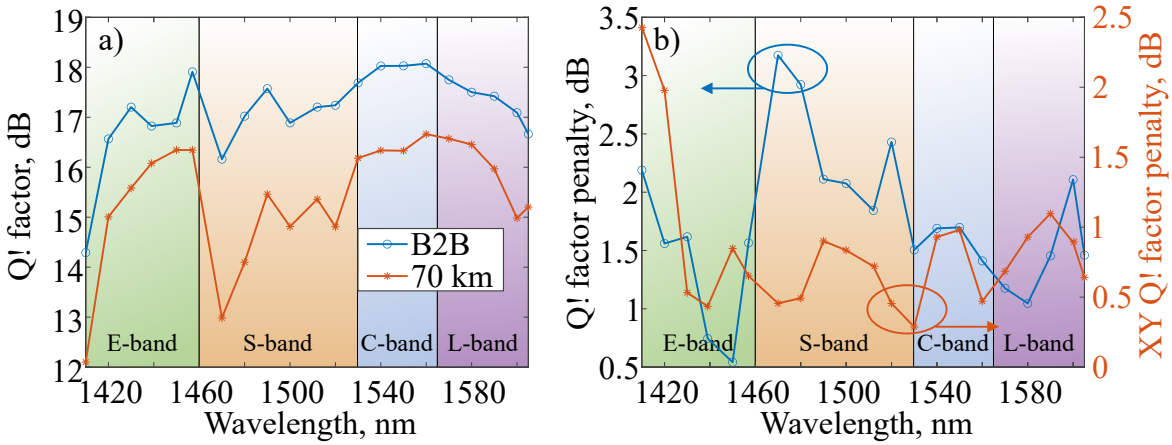

Fig. 5.29 a) Wavelength dependency of the Q^2 factor for B2B case and 70-km long transmission; b) wavelength dependency of Q^2 factor penalty between B2B case and transmission (blue line with circles) and X and Y polarisation Q^2 factor imbalance (orange line with stars).

The E-band B2B measurement was enabled by two in-house-made BDFAs that are the BDFA-2 and BDFA-3 from Section 4.3. The general B2B performance level is similar to the L-band case. However, there is a significant decrease of the performance at 1410 nm. This can be explained by substantial limitations of the optical hybrid, in terms of polarisation balance starting at 1420 nm. The X and Y polarisation imbalance penalty is presented in Figure 5.29,b. The polarisation imbalance was measured as a difference between the average performance of the system in terms of Q^2 factor for X and Y polarisation. There is a significant increase of the X and Y impairment below 1430 nm. The commercial optical hybrid, transceiver and optical photodiodes used in this experiment were optimised for operation in the C- and L-optical bands. Despite the limited operation bandwidth, the X-Y impairment is lower than 2.5 dB in the whole region from 1430 to 1605 nm. The E-band transmission features the lowest Q^2 factor penalty of just 0.5 dB. Otherwise, the general performance of the in-line BDFA is similar to C- and L- band DRA. The increase of penalty towards 1410 nm is explained by both rising NF and decreasing gain of the amplifier. Based on the discussed results, here we report one of the record transmission bandwidths for coherent transmission lines with 195 nm and total of 34.2 Tbits/s (2 x 4 bits x 30GBaud x 143 channels) [132–134].

5.4 Summary

In this chapter the description of the main quality metrics for both IM/DD and coherent signals were presented. The setup descriptions of both IM/DD and coherent systems were provided along with the procedure for their control and set up. The developed BDFAs were used to demonstrate 4 channel IM/DD transmission through 160 km of 10 Gbit/s OOK NRZ signal which was the record transmission distance for IM/DD system in E-band. An in-depth study of the coherent transmission systems enabled by developed BDFAs was performed. It included two separate experimental works. A 60 km long transmission of 50 GBaud SP QPSK supported by 2 BDFAs was performed first. Then a 4 channel E-band 30 GBaud 16 QAM transmission over 160 km supported by 3 BDFAs was demonstrated. The transmission quality was characterised and the performance degradation factors were appropriately discussed. The main factors are: sensitivity of the photodiodes, limitation of the optical hybrid and the optical modulator. The record bandwidth transmission of the coherent signal in E-S,C-L bands was demonstrated. The transmission was supported by developed BDFAs and DRA discussed in details in the PhD thesis of Dr Pratim Hazarika. The signal consisted of DP 143 30 Gbaud 16 QAM channels and is transmitted through 70 km of SMF. The main conclusion of this thesis is that the BDFA is a reliable lump amplifier that can effectively be used as an in-line, booster, or receive amplifier.

Chapter 6

Discussion, future work and conclusion

In this thesis, it has been shown that BDFAs are a robust and flexible solution for expanding the capacity of optical communication networks. In particular, a lot of attention has been paid to the development and utilisation of E-S-band BDFAs based on low-germanosilicate fibre. The expansion towards E-band and lower S-band allows to not only widen the bandwidth of the already deployed network with minimal impact on the already deployed C and L-bands due to minimal SRS from E-band towards C-band, but also to develop ulta-wideband communication networks (with bandwidths more than 200 nm) enabled by the combination of BDFAs with other amplifiers.

Three BDFAs based on low-germanosilicate Bi-doped fibre for operation in E- and S-bands were developed. The record characteristics for single-stage BDFA have been achieved with a 173 m-long BDF-based BDFA. The developed amplifier features a maximum gain of 40 dB, the lowest NF of 4.7 dB, and the maximum PCE of 38%. One of the most important amplifier parameters is PCE due to high requirements from optical network providers. However, the achieved PCE shows a great potential for E-band BDFAs to be next in line for the upgrade of optical communication networks, as it is twice as high as L-band BDFA and almost as big as the PCE of C-band BDFAs with 50%. In future work, multi-stage and multi-band BDFAs are planned to be studied. Such BDFAs can achieve even higher PCE and better gain flatness. Moreover, a BDFA can be combined with a C-band EDFA to achieve a wideband E-S-C-band amplifier [135].

In terms of data transmission, a number of experiments have been performed to proved E-S-band BDFA applicability for both IM/DD and coherent data transmission. As the first step, the record transmission in E-band was performed with four 10 Gbit/s NRZ OOK channels in E-bands supported by two developed BDFAs to allow to expand the distance from the previous record of 80 km to 160 km. As E-S-band BDFA seems to be a solution for network capacity increase for long-haul and metro networks, it was important to demonstrate

a coherent transmission enabled by BDFA. A coherent transmission of 5 SP 50 GBaud QPSK channels was transmitted through 60 km of SSMF. This work was the first-ever demonstration of coherent transmission enabled by a BDFA. Later, a transmission of five DP 30 GBaud 16 QAM channels over 160 km enabled by three developed BDFAs was performed. This experiment showed a record coherent data transmission for E-band. Finally, a multi-band (E-S-C-L-bands) experiment of a DP 143x30 Gbaud 16 QAM signal transmission over 70 km was demonstrated. The amplifier used for this experiment was developed to combine BDFA in E-band and DRA in S-C-L-bands. The quality of the transmission was appropriately analysed in terms of the BER for the IM/DD experiment the and Q factor for the coherent transmissions.

The first approaches in modelling of BDFAs have been made based on conventional rate equation modelling and neural-network-based approaches for modelling of BDFA as a "black box". As the concentration of the Bi-related centres is too small to be detected by conventional measurement methods, it is still a matter of correct retrieval of the concentration using, for instance, convergence methods. The proposed method showed allowed to achieve the unknown parameters like absorption and emission cross sections of the signal and pump, lifetime and BACs concentration. The model was used to predict a single channel amplification in the spectral range 1384-1480 nm and for three different input signal powers. However, the retrieved parameters depended highly on the initial guesses indicating that an alternative approach should be proposed for retrieval of the parameters or modelling of BDFAs as black boxes. The NN-based approach has been proposed to map the input BDFA parameters (signal power, signal wavelength, and pump powers) with output BDFA parameters (wavelength dependent gain and NF). The model was studied with different types of data sets and their sizes for a case of four channel amplification (1430 nm, 1450 nm, 1470nm, and 1490 nm). Even though a randomly distributed data set showed a good performance in the boundaries of the measurement with the maximum absolute error E_{MAX} less than 1 dB, the model was not used to predict BDFA performance beyond the data set range. Performing the modelling to predict the performance of BDFAs beyond the measurement range seems to be a natural next step to prove that the NN approach can be used for modelling of BDF-based systems.

The results presented in this thesis show an excellent performance of BDFAs and their high compatibility with already deployed optical components. Moreover, BDFA performance seems better than other natural competitors like SOAs, NDFAs, and DRAs, however, BDFAs are not yet well studied to allow a robust and reliable method of modelling of BDF-based systems which is the crucial part of optimisation of any optical amplifier. Alternative approaches should be proposed and studied to enable maximisation of BDFAs' performance.

Unfortunately, WSS or optical cantilevers are not commercially available yet, thus, a full WDM transmission experiment in E-band was not performed. This experiment is a crucial part of proving that E-band transmission enabled by BDFAs will minimally effect already deployed C-L systems. At last, the final challenge associated with BDFA is fibre length. Even though the progress of the fibre quality is visibly being made (5 years ago, 30 dB gain was achieved with 300 m fibre; today, 40 dB gain can be achieved with 173 m fibre), this fibre length still seems to be too long for a full ITU-T item size compatibility. To conclude, BDFAs have shown a great progress in recent years, and they seem to be a perfect candidate for expanding optical communication networks. However, BDFAs still require some crucial steps to become mature enough to be implemented in commercial communication networks.

References

[1] Govind P Agrawal. *Fiber-optic communication systems*. John Wiley & Sons, 2012.

[2] Robert J Mears, L Reekie, IM Jauncey, and David N Payne. Low-noise erbium-doped fibre amplifier operating at 1.54 μm. *Electronics Letters*, 19(23):1026–1028, 1987.

[3] Peter J Winzer, David T Neilson, and Andrew R Chraplyvy. Fiber-optic transmission and networking: the previous 20 and the next 20 years. *Optics express*, 26(18): 24190–24239, 2018.

[4] Erik Agrell, Magnus Karlsson, AR Chraplyvy, David J Richardson, Peter M Krummrich, Peter Winzer, Kim Roberts, Johannes Karl Fischer, Seb J Savory, Benjamin J Eggleton, et al. Roadmap of optical communications. *Journal of Optics*, 18(6):063002, 2016.

[5] Junho Cho, Xi Chen, Sethumadhavan Chandrasekhar, Gregory Raybon, Ronen Dar, Laurent Schmalen, Ells Burrows, Andrew Adamiecki, Steve Corteselli, Yan Pan, et al. Trans-atlantic field trial using high spectral efficiency probabilistically shaped 64-qam and single-carrier real-time 250-gb/s 16-qam. *Journal of Lightwave Technology*, 36 (1):103–113, 2017.

[6] Thierry Zami, Bruno Lavigne, Oriol Bertran Pardo, Stefan Weisser, Julien David, Maël Le Monnier, and Jean-Paul Faure. 31.2-tb/s real time bidirectional transmission of 78x400 gb/s interleaved channels over c band of one 90-km smf span. In *Optical Fiber Communication Conference*, pages W1B–5. Optical Society of America, 2018.

[7] Peter J Winzer and Rene-Jean Essiambre. Advanced optical modulation formats. In *Optical Fiber Telecommunications VB*, pages 23–93. Elsevier, 2008.

[8] Metodi P Yankov, Francesco Da Ros, Edson P da Silva, Søren Forchhammer, Knud J Larsen, Leif K Oxenløwe, Michael Galili, and Darko Zibar. Constellation shaping for wdm systems using 256qam/1024qam with probabilistic optimization. *Journal of Lightwave Technology*, 34(22):5146–5156, 2016.

[9] Samuel LI Olsson, Junho Cho, Sethumadhavan Chandrasekhar, Xi Chen, Peter J Winzer, and Sergejs Makovejs. Probabilistically shaped pdm 4096-qam transmission over up to 200 km of fiber using standard intradyne detection. *Optics express*, 26(4): 4522–4530, 2018.

[10] Xi Chen, Junho Cho, Andrew Adamiecki, and Peter Winzer. 16384-qam transmission at 10 gbd over 25-km ssmf using polarization-multiplexed probabilistic constellation

shaping. In *45th European Conference on Optical Communication (ECOC 2019)*, pages 1–4. IET, 2019.

[11] Claude Elwood Shannon. A mathematical theory of communication. *The Bell system technical journal*, 27(3):379–423, 1948.

[12] Govind P Agrawal. Nonlinear fiber optics. In *Nonlinear Science at the Dawn of the 21st Century*, pages 195–211. Springer, 2000.

[13] Partha P Mitra and Jason B Stark. Nonlinear limits to the information capacity of optical fibre communications. *Nature*, 411(6841):1027–1030, 2001.

[14] Andrew D Ellis, Jian Zhao, and David Cotter. Approaching the non-linear Shannon limit. *Journal of Lightwave Technology*, 28(4):423–433, 2009.

[15] Glenn Wellbrock and Tiejun J Xia. How will optical transport deal with future network traffic growth? In *2014 The European Conference on Optical Communication (ECOC)*, pages 1–3. IEEE, 2014.

[16] David J Richardson, John M Fini, and Lynn E Nelson. Space-division multiplexing in optical fibres. *Nature photonics*, 7(5):354–362, 2013.

[17] Takayuki Kobayashi, Masanori Nakamura, Fukutaro Hamaoka, Kohki Shibahara, Takayuki Mizuno, Akihide Sano, H Kawakami, Akira Isoda, Munehiko Nagatani, Hiroshi Yamazaki, et al. 1-pb/s (32 sdm/46 wdm/768 gb/s) c-band dense sdm transmission over 205.6-km of single-mode heterogeneous multi-core fiber using 96-gbaud pdm-16qam channels. In *2017 Optical Fiber Communications Conference and Exhibition (OFC)*, pages 1–3. IEEE, 2017.

[18] Alessio Ferrari, Antonio Napoli, Johannes Karl Fischer, Nelson Manuel Simes da Costa, Andrea D'Amico, Joao Pedro, Wladek Forysiak, Erwan Pincemin, Andrew Lord, Alexandros Stavdas, et al. Assessment on the achievable throughput of multi-band ITU-T G. 652.D fiber transmission systems. *Journal of Lightwave Technology*, 2020.

[19] Jay W Dawson, Leily S Kiani, Paul H Pax, Graham S Allen, Derrek R Drachenberg, Victor V Khitrov, Diana Chen, Nick Schenkel, Matthew J Cook, Robert P Crist, et al. E-band Nd 3+ amplifier based on wavelength selection in an all-solid micro-structured fiber. *Optics express*, 25(6):6524–6538, 2017.

[20] Yan Ososkov, Aleksandr Khegai, Sergei Firstov, Konstantin Riumkin, Sergey Alyshev, Alexander Kharakhordin, Alexey Lobanov, Alexey Guryanov, and Mikhail Melkumov. Pump-efficient flattop o+ e-bands bismuth-doped fiber amplifier with 116 nm–3 db gain bandwidth. *Optics Express*, 29(26):44138–44145, 2021.

[21] M Tan, Pawel Rosa, ST Le, Md A Iqbal, ID Phillips, and P Harper. Transmission performance improvement using random dfb laser based raman amplification and bidirectional second-order pumping. *Optics express*, 24(3):2215–2221, 2016.

[22] Chandra B Gaur, Vladimir Gordienko, Florent Bessin, and Nick J Doran. Dual-band amplification of downstream l-band and upstream c-band signals by fopa in extended reach pon. In *2020 European Conference on Optical Communications (ECOC)*, pages 1–4. IEEE, 2020.

[23] Jeremie Renaudier, Aymeric Arnould, Amirhossein Ghazisaeidi, Dylan Le Gac, Patrick Brindel, Elie Awwad, Mathilde Makhsiyan, Karim Mekhazni, Fabrice Blache, Aurelien Boutin, et al. Recent advances in 100+ nm ultra-wideband fiber-optic transmission systems using semiconductor optical amplifiers. *Journal of Lightwave Technology*, 38 (5):1071–1079, 2020.

[24] B Correia, A Donodin, R Sadeghi, V Dvoyrin, A Napoli, J Pedro, N Costa, W Forysiak, SK Turitsyn, and V Curri. Qot evaluation of optical line system transmission with bismuth-doped fiber amplifiers in the e-band. In *Asia Communications and Photonics Conference*, pages M4I–5. Optica Publishing Group, 2021.

[25] Chandrasekhara Venkata Raman. A new radiation. *Indian Journal of physics*, 2: 387–398, 1928.

[26] E Woodbury and W Nag. First demonstration of stimulated raman scattering. *Proc. IRE*, 50(6):2347, 1962.

[27] Shu Namiki and Yoshihiro Emori. Ultrabroad-band raman amplifiers pumped and gain-equalized by wavelength-division-multiplexed high-power laser diodes. *IEEE Journal of Selected Topics in Quantum Electronics*, 7(1):3–16, 2001.

[28] Mohammed N Islam. Raman amplifiers for telecommunications. *IEEE Journal of selected topics in Quantum Electronics*, 8(3):548–559, 2002.

[29] Mingming Tan, Paweł Rosa, Son Thai Le, Ian D Phillips, and Paul Harper. Evaluation of 100g dp-qpsk long-haul transmission performance using second order co-pumped raman laser based amplification. *Optics express*, 23(17):22181–22189, 2015.

[30] Lukasz Krzczanowicz, Md Asif Iqbal, Ian Phillips, Mingming Tan, Pavel Skvortcov, Paul Harper, and Wladek Forysiak. Low transmission penalty dual-stage broadband discrete raman amplifier. *Optics express*, 26(6):7091–7097, 2018.

[31] Pratim Hazarika, Mingming Tan, Aleksandr Donodin, Ian Phillips, Paul Harper, Ming-Jun Li, and Wladek Forysiak. 210 nm e, s, c and l band multistage discrete raman amplifier. In *Optical Fiber Communication Conference*, pages Tu3E–2. Optica Publishing Group, 2022.

[32] Sijing Liang, Saurabh Jain, Lin Xu, Kyle RH Bottrill, Natsupa Taengnoi, Massimiliano Guasoni, Peng Zhang, Mengben Xiao, Qiongyue Kang, Yongmin Jung, et al. High gain, low noise, spectral-gain-controlled, broadband lumped fiber raman amplifier. *Journal of Lightwave Technology*, 39(5):1458–1463, 2021.

[33] Uiara Celine De Moura, Md Asif Iqbal, Morteza Kamalian, Lukasz Krzczanowicz, Francesco Da Ros, Ann Margareth Rosa Brusin, Andrea Carena, Wladek Forysiak, Sergei Turitsyn, and Darko Zibar. Multi–band programmable gain Raman amplifier. *Journal of Lightwave Technology*, 39(2):429–438, 2020.

[34] Michael J Connelly. *Semiconductor optical amplifiers*. Springer Science & Business Media, 2007.

[35] Lutz Rapp and Michael Eiselt. Optical amplifiers for multi–band optical transmission systems. *Journal of Lightwave Technology*, 40(6):1579–1589, 2021.

[36] Michel E Marhic, Peter A Andrekson, Periklis Petropoulos, Stojan Radic, Christophe Peucheret, and Mahmoud Jazayerifar. Fiber optical parametric amplifiers in optical communication systems. *Laser & photonics reviews*, 9(1):50–74, 2015.

[37] Thomas Torounidis, Peter A Andrekson, and B-E Olsson. Fiber-optical parametric amplifier with 70-db gain. *IEEE Photonics Technology Letters*, 18(10):1194–1196, 2006.

[38] Jose M Chavez Boggio, Slaven Moro, Evgeny Myslivets, Joshua R Windmiller, Nikola Alic, and Stojan Radic. 155-nm continuous-wave two-pump parametric amplification. *IEEE Photonics Technology Letters*, 21(10):612–614, 2009.

[39] Zhi Tong, Carl Lundström, PA Andrekson, CJ McKinstrie, Magnus Karlsson, DJ Blessing, Ekawit Tipsuwannakul, BJ Puttnam, Hiroyuki Toda, and L Grüner-Nielsen. Towards ultrasensitive optical links enabled by low-noise phase-sensitive amplifiers. *Nature photonics*, 5(7):430–436, 2011.

[40] Adonis Bogris and Dimitris Syvridis. Distributed optical parametric amplification at 1.3μm : Performance and applications in optical access networks. *IEEE Photonics Technology Letters*, 24(8):694–696, 2012.

[41] Vladimir Gordienko, Filipe M Ferreira, Chandra B Gaur, and Nick J Doran. Looped polarization-insensitive fiber optical parametric amplifiers for broadband high gain applications. *Journal of Lightwave Technology*, 39(19):6045–6053, 2021.

[42] Chandra B Gaur, Vladimir Gordienko, Pratim Hazarika, and Nick J Doran. Polarization insensitive fiber optic parametric amplifier with a gain bandwidth of 22 nm in s-band. In *Optical Fiber Communication Conference*, pages W4J–1. Optica Publishing Group, 2022.

[43] C Randy Giles and Emmanuel Desurvire. Modeling erbium-doped fiber amplifiers. *Journal of lightwave technology*, 9(2):271–283, 1991.

[44] Michel JF Digonnet. *Rare-earth-doped fiber lasers and amplifiers, revised and expanded*. CRC press, 2001.

[45] Emmanuel Desurvire and Michael N Zervas. Erbium-doped fiber amplifiers: principles and applications. *Physics Today*, 48(2):56, 1995.

[46] Emmanuel Desurvire. *Erbium-doped fiber amplifiers: Device and System Developments*. Wiley-Interscience, 2002.

[47] RI Laming, JE Townsend, DN Payne, F Meli, G Grasso, and EJ Tarbox. High-power erbium-doped-fiber amplifiers operating in the saturated regime. *IEEE Photonics technology letters*, 3(3):253–255, 1991.

[48] Li Qian and Ryan Bolen. Erbium-doped phosphosilicate fiber amplifiers: a comparison of configurations for the optimization of noise figure and conversion efficiency. In *Photonic Applications in Devices and Communication Systems*, volume 5970, page 59702V. International Society for Optics and Photonics, 2005.

[49] Ziwei Zhai, Arindam Halder, Martín Núñez-Velázquez, and Jayanta K Sahu. Temperature-dependent study on l-band edfa characteristics pumped at 980 nm and 1480 nm in phosphorus and aluminum-rich erbium-doped silica fibers. *Journal of Lightwave Technology*, 40(14):4819–4824, 2022.

[50] Y Miyajima, T Sugawa, and Y Fukasaku. 38.2 db amplification at 1.31 mu m and possibility of 0.98 mu m pumping in Pr/sup 3+/-doped fluoride fibre. *Electronics Letters*, 27(19):1706–1707, 1991.

[51] B Pedersen, WJ Miniscalco, and RS Quimby. Optimization of Pr/sup 3+: Zblan fiber amplifiers. *IEEE Photonics technology letters*, 4(5):446–448, 1992.

[52] Yoshiki Nishida, Makoto Yamada, Terutoshi Kanamori, Kenji Kobayashi, Jiro Temmyo, Shoichi Sudo, and Yasutake Ohishi. Development of an efficient praseodymium-doped fiber amplifier. *IEEE journal of quantum electronics*, 34(8):1332–1339, 1998.

[53] M Brierley, S Carter, P France, and JE Pedersen. Amplification in the 1300 nm telecommunications window in a Nd-doped fluoride fibre. *Electronics Letters*, 26(5): 329–330, 1990.

[54] Charles D Boley, Jay W Dawson, Leily S Kiani, and Paul H Pax. E-band neodymium-doped fiber amplifier: model and application. *Applied Optics*, 58(9):2320–2327, 2019.

[55] Pavel Peterka, Basile Faure, Wilfried Blanc, M Karasek, and Bernard Dussardier. Theoretical modelling of s-band thulium-doped silica fibre amplifiers. *Optical and Quantum Electronics*, 36(1):201–212, 2004.

[56] Rajandeep Singh and Maninder Lal Singh. Investigation of the effect of change in doping parameters on the gain of a thulium doped fiber amplifier. *Journal of Optical Technology*, 88(4):215–226, 2021.

[57] Fabien Roy, Florence Leplingard, Laurence Lorcy, A Sauze, Pascal Baniel, and Dominique Bayart. 48% power conversion efficiency in a single-pump gain-shifted thulium-doped fiber amplifier. In *OFC 2001. Optical Fiber Communication Conference and Exhibit. Technical Digest Postconference Edition (IEEE Cat. 01CH37171)*, volume 4, pages PD2–PD2. IEEE, 2001.

[58] Fabien Roy, Dominique Bayart, Céline Heerdt, André Le Sauze, and Pascal Baniel. Spectral hole burning measurement thulium-doped fiber amplifiers. *Optics letters*, 27 (1):10–12, 2002.

[59] MH Aly, M Nasr, and HE Seleem. Thulium doped fiber amplifier in the s/s/sup+/band employing different concentration profiles. In *2005 Fifth Workshop on Photonics and its Applications*, pages 39–49. IEEE, 2005.

[60] Evgenii M Dianov, VV Dvoyrin, Valerii Mikhailovich Mashinsky, Andrei Aleksandrovich Umnikov, Mikhail Viktorovich Yashkov, and Aleksei Nikolaevich Gur'yanov. CW bismuth fibre laser. *Quantum Electronics*, 35(12):1083, 2005.

[61] Vladislav V. Dvoyrin, Alexander V. Kir'yanov, Valery M. Mashinsky, Oleg I Medvedkov, Andrey A Umnikov, Alexei N Guryanov, and Evgeny M Dianov. Absorption, gain, and laser action in bismuth-doped aluminosilicate optical fibers. *IEEE journal of quantum electronics*, 46(2):182–190, 2009.

[62] NK Thipparapu, Yu Wang, S Wang, P Barua, and JK Sahu. Bi-doped silica-based fiber amplifier for O-band transmission. In *Asia Communications and Photonics Conference*, pages S3G–6. Optical Society of America, 2019.

[63] Aleksandr Donodin, Vladislav Dvoyrin, Egor Manuylovich, Lukasz Krzczanowicz, Wladek Forysiak, Mikhail Melkumov, Valery Mashinsky, and Sergei Turitsyn. Bismuth doped fibre amplifier operating in e-and s-optical bands. *Optical Materials Express*, 11(1):127–135, 2021.

[64] Sergei Firstov, Sergey Alyshev, Mikhail Melkumov, Konstantin Riumkin, Alexey Shubin, and Evgeny Dianov. Bismuth-doped optical fibers and fiber lasers for a spectral region of 1600–1800 nm. *Optics letters*, 39(24):6927–6930, 2014.

[65] Yu Wang, Naresh Kumar Thipparapu, David J Richardson, and JK Sahu. Broadband bismuth-doped fiber amplifier with a record 115-nm bandwidth in the O and E bands. In *Optical Fiber Communication Conference*, pages Th4B–1. Optical Society of America, 2020.

[66] NK Thipparapu, Y Wang, AA Umnikov, P Barua, DJ Richardson, and JK Sahu. 40 dB gain all fiber bismuth-doped amplifier operating in the O-band. *Optics letters*, 44 (9):2248–2251, 2019.

[67] Yang Hong, Natsupa Taengnoi, Kyle RH Bottrill, Hesham Sakr, Thomas D Bradley, John R Hayes, Gregory T Jasion, Yu Wang, Naresh K Thipparapu, Andrey A Umnikov, et al. Dual o+ c-band wdm transmission over 1-km hollow core nanf using an o-band bismuth-doped fibre amplifier. 2019.

[68] Vitaly Mikhailov, MA Melkumov, Daryl Inniss, AM Khegai, KE Riumkin, SV Firstov, FV Afanasiev, Man F Yan, Yingzhi Sun, Jiawei Luo, et al. Simple broadband bismuth doped fiber amplifier (bdfa) to extend o-band transmission reach and capacity. In *Optical Fiber Communication Conference*, pages M1J–4. Optical Society of America, 2019.

[69] MA Melkumov, V Mikhailov, AM Hegai, KE Riumkin, PS Westbrook, DJ DiGiovanni, and EM Dianov. E-band data transmission over 80 km of non-zero dispersion fibre link using bismuth-doped fibre amplifier. *Electronics Letters*, 53(25):1661–1663, 2017.

[70] Aleksandr Donodin, Mingming Tan, Ian Phillips, Abdallah AI Ali, Pratim Hazarika, Mohammed Patel, Paul Harper, Vladislav Dvoyrin, Wladek Forysiak, and Sergei Turitsyn. Gbaud qpsk e-band transmission using bismuth doped fiber amplifiers. In *Optical Fiber Communication Conference*, pages W3J–5. Optica Publishing Group, 2022.

[71] Naresh Kumar Thipparapu. *Development of bi-doped fibre amplifiers and lasers & broadband Er-doped multi-element fibre amplifiers*. PhD thesis, University of Southampton, 2018.

[72] Evgeny M Dianov. Bismuth-doped optical fibers: a challenging active medium for near-IR lasers and optical amplifiers. *Light: Science & Applications*, 1(5):e12–e12, 2012.

[73] Yasushi Fujimoto Yasushi Fujimoto and Masahiro Nakatsuka Masahiro Nakatsuka. Infrared luminescence from bismuth-doped silica glass. *Japanese Journal of Applied Physics*, 40(3B):L279, 2001.

[74] VV Dvoyrin, VM Mashinsky, EM Dianov, AA Umnikov, MV Yashkov, and AN Guryanov. Absorption, fluorescence and optical amplification in mcvd bismuth-doped silica glass optical fibres. In *2005 31st European Conference on Optical Communication, ECOC 2005*, volume 4, pages 949–950. IET, 2005.

[75] Lenar I Bulatov, Valerii M Mashinskii, Vladislav V Dvoirin, Evgenii F Kustov, and Evgenii M Dianov. Luminescent properties of bismuth centres in aluminosilicate optical fibres. *Quantum electronics*, 40(2):153, 2010.

[76] SV Firstov, VF Khopin, IA Bufetov, EG Firstova, AN Guryanov, and EM Dianov. Combined excitation-emission spectroscopy of bismuth active centers in optical fibers. *Optics express*, 19(20):19551–19561, 2011.

[77] LI Bulatov, VM Mashinsky, VV Dvoirin, EF Kustov, EM Dianov, and AP Sukhorukov. Structure of absorption and luminescence bands in aluminosilicate optical fibers doped with bismuth. *Bulletin of the Russian Academy of Sciences: Physics*, 72(12): 1655–1660, 2008.

[78] Evgeny M Dianov, Alexey V Shubin, Mikhail A Melkumov, Oleg I Medvedkov, and Igor A Bufetov. High-power cw bismuth-fiber lasers. *JOSA B*, 24(8):1749–1755, 2007.

[79] VG Truong, L Bigot, Alain Lerouge, M Douay, and I Razdobreev. Study of thermal stability and luminescence quenching properties of bismuth-doped silicate glasses for fiber laser applications. *Applied Physics Letters*, 92(4):041908, 2008.

[80] AA Umnikov, AN Guryanov, AN Abramov, NN Vechkanov, SV Firstov, VM Mashinsky, VV Dvoyrin, LI Bulatov, and EM Dianov. Al-free core composition bismuth-doped optical fibre with luminescence band at 1300 nm. In *2008 34th European Conference on Optical Communication*, pages 1–2, 2008.

[81] Elena G Firstova. Optical properties of bismuth-doped sio2-or geo2-based glass core optical fibers. *arXiv preprint arXiv:1503.05065*, 2015.

[82] Evgenii M Dianov, Mikhail A Mel'kumov, Aleksei V Shubin, Sergei V Firstov, Vladimir Fedorovich Khopin, Aleksei N Gur'yanov, and Igor'A Bufetov. Bismuth-doped fibre amplifier for the range 1300—1340 nm. *Quantum electronics*, 39(12): 1099, 2009.

[83] Evgenii Mikhailovich Dianov, Sergei Vladimirovich Firstov, Vladimir Fedorovich Khopin, Aleksei Nikolaevich Gur'yanov, and Igor'Alekseevich Bufetov. Bi-doped fibre lasers and amplifiers emitting in a spectral region of 1.3 μm. *Quantum Electronics*, 38(7):615, 2008.

[84] Yu Wang, Naresh K Thipparapu, David J Richardson, and Jayanta K Sahu. Ultra-broadband bismuth-doped fiber amplifier covering a 115-nm bandwidth in the o and e bands. *Journal of Lightwave Technology*, 39(3):795–800, 2021.

[85] Yuta Wakayama, Vitaly Mikhailov, Daniel J Elson, Rachata Maneekut, Jiawei Luo, Cen Wang, Filippos Balasis, Noboru Yoshikane, Daryl Inniss, and Takehiro Tsuritani. 400gbase-lr4 transmission over field-deployed fibre link supported by bismuth-doped fibre amplifier. In *2021 European Conference on Optical Communication (ECOC)*, pages 1–4. IEEE, 2021.

[86] Yang Hong, Natsupa Taengnoi, Kyle RH Bottrill, Naresh K Thipparapu, Yu Wang, Jayanta K Sahu, David J Richardson, and Periklis Petropoulos. Experimental demonstration of single-span 100-km o-band 4$\times$ 50-gb/s cwdm direct-detection transmission. *Optics Express*, 30(18):32189–32203, 2022.

[87] Yang Hong, Kyle RH Bottrill, Natsupa Taengnoi, Naresh K Thipparapu, Yu Wang, Andrey A Umnikov, Jayanta K Sahu, David J Richardson, and Periklis Petropoulos. Experimental demonstration of dual o+ c-band wdm transmission over 50-km ssmf with direct detection. *Journal of Lightwave Technology*, 38(8):2278–2284, 2020.

[88] Yang Hong, Hesham Sakr, Natsupa Taengnoi, Kyle RH Bottrill, Thomas D Bradley, John R Hayes, Gregory T Jasion, Hyuntai Kim, Naresh K Thipparapu, Yu Wang, et al. Multi-band direct-detection transmission over an ultrawide bandwidth hollow-core nanf. *Journal of Lightwave Technology*, 38(10):2849–2857, 2020.

[89] VV Dvoyrin, OI Medvedkov, VM Mashinsky, AA Umnikov, AN Guryanov, and EM Dianov. Optical amplification in 1430–1495 nm range and laser action in Bi-doped fibers. *Optics Express*, 16(21):16971–16976, 2008.

[90] VM Mashinsky and VV Dvoyrin. Bismuth-doped fiber amplifiers: State of the art and future prospect. In *2009 IEEE LEOS Annual Meeting Conference Proceedings*, pages 775–776. IEEE, 2009.

[91] Evgenii M Dianov, Sergei Vladimirovich Firstov, Vladimir Fedorovich Khopin, Oleg Igorevich Medvedkov, Aleksei N Gur'yanov, and Igor'A Bufetov. Bi-doped fibre lasers operating in the range 1470–1550 nm. *Quantum Electronics*, 39(4):299, 2009.

[92] Igor A Bufetov, Mikhail A Melkumov, Sergei V Firstov, Konstantin E Riumkin, Alexey V Shubin, Vladimir F Khopin, Alexei N Guryanov, and Evgeny M Dianov. Bi-doped optical fibers and fiber lasers. *IEEE Journal of Selected Topics in Quantum Electronics*, 20(5):111–125, 2014.

[93] Egor Manuylovich, Vladislav Dvoyrin, Dmitrii Pushkarev, Inga Mazaeva, and Sergei Turitsyn. 4-channel bi-doped fibre amplifier. In *45th European Conference on Optical Communication (ECOC 2019)*, pages 1–4. IET, 2019.

[94] Yu Wang, Naresh K Thipparapu, David J Richardson, and Jayanta K Sahu. High gain bi-doped fiber amplifier operating in the e-band with a 3-db bandwidth of 40nm. In *Optical Fiber Communication Conference*, pages Tu1E–1. Optica Publishing Group, 2021.

[95] Aleksandr Donodin, Egor Manuylovich, Vladislav Dvoyrin, Mikhail Melkumov, Vitaly Mashinsky, and Sergei Turitsyn. 38 db gain e-band bismuth-doped fiber amplifier. In *48th European Conference on Optical Communication (ECOC 2022)*, pages 1–4. IET, 2022.

[96] Aleksandr Donodin, Vladislav Dvoyrin, Egor Manuylovich, Ian Phillips, Wladek Forysiak, Mikhail Melkumov, Valery Mashinsky, and Sergei Turitsyn. 4-channel e-band data transmission over 160 km of smf-28 using a bismuth-doped fibre amplifier. In *Optical Fiber Communication Conference*, pages Tu1E–3. Optica Publishing Group, 2021.

[97] Aleksandr Donodin, Pratim Hazarika, Mingming Tan, Vladislav Dvoyrin, Mohammed Patel, Ian Phillips, Paul Harper, Sergei Turitsyn, and Wladek Forysiak. 195-nm multi-band amplifier enabled by bismuth-doped fiber and discrete raman amplification. In *48th European Conference on Optical Communication (ECOC 2019)*, pages 1–4. IET, 2022.

[98] Aleksandr Donodin, Mingming Tan, Pratim Hazarika, Vladislav Dvoyrin, Ian Phillips, Paul Harper, Sergei K. Turitsyn, and Wladek Forysiak. 30-gbaud dp 16-qam transmission in the e-band enabled by bismuth-doped fiber amplifiers. *Opt. Lett.*, 47(19): 5152–5155, 2022.

[99] Sergei V Firstov, Sergey V Alyshev, Konstantin E Riumkin, Vladimir F Khopin, Alexey N Guryanov, Mikhail A Melkumov, and Evgeny M Dianov. A 23-db bismuth-doped optical fiber amplifier for a 1700-nm band. *Scientific reports*, 6(1):1–6, 2016.

[100] Sergei V Firstov, Sergey V Alyshev, Konstantin E Riumkin, Aleksandr M Khegai, Alexander V Kharakhordin, Mikhail A Melkumov, and Evgeny M Dianov. Laser-active fibers doped with bismuth for a wavelength region of 1.6–1.8 μm. *IEEE Journal of Selected Topics in Quantum Electronics*, 24(5):1–15, 2018.

[101] RM Martin and RS Quimby. Experimental evidence of the validity of the mccumber theory relating emission and absorption for rare-earth glasses. *JOSA B*, 23(9):1770–1775, 2006.

[102] Robert C Hilborn. Einstein coefficients, cross sections, f values, dipole moments, and all that. *American Journal of Physics*, 50(11):982–986, 1982.

[103] RS Quimby. Range of validity of mccumber theory in relating absorption and emission cross sections. *Journal of applied physics*, 92(1):180–187, 2002.

[104] Saša Singer and John Nelder. Nelder-mead algorithm. *Scholarpedia*, 4(7):2928, 2009.

[105] Maria Ionescu, Amirhossein Ghazisaeidi, Jérémie Renaudier, Pascal Pecci, and Olivier Courtois. Design optimisation of power-efficient submarine line through machine learning. In *2020 Conference on Lasers and Electro-Optics (CLEO)*, pages 1–2, 2020.

[106] Metodi Plamenov Yankov, Uiara Celine De Moura, and Francesco Da Ros. Power evolution modeling and optimization of fiber optic communication systems with edfa repeaters. *Journal of Lightwave Technology*, 2021. doi: 10.1109/JLT.2021.3061632. early access.

[107] Darko Zibar, Ann Margareth Rosa Brusin, Uiara C de Moura, Francesco Da Ros, Vittorio Curri, and Andrea Carena. Inverse system design using machine learning: the Raman amplifier case. *Journal of Lightwave Technology*, 38(4):736–753, 2019.

[108] Aleksandr Donodin, Uiara Celine de Moura, Ann Margareth Rosa Brusin, Egor Manuylovich, Vladislav Dvoyrin, Francesco Da Ros, Andrea Carena, Wladek Forysiak, Darko Zibar, and Sergei K Turitsyn. Neural network modeling of bismuth-doped fiber amplifier. *Journal of the European Optical Society-Rapid Publications*, 19(1):4, 2023.

[109] Douglas M Baney, Philippe Gallion, and Rodney S Tucker. Theory and measurement techniques for the noise figure of optical amplifiers. *Optical fiber technology*, 6(2): 122–154, 2000.

[110] Guang-Bin Huang, Dian Hui Wang, and Yuan Lan. Extreme learning machines: a survey. *Int. J. Mach. Learn. Cyb.*, 2(2):107–122, 2011. ISSN 1868-808X. doi: 10.1007/s13042-011-0019-y.

[111] HA Haus. The noise figure of optical amplifiers. *IEEE Photonics Technology Letters*, 10(11):1602–1604, 1998.

[112] JF Michel. Digonnet, rare-earth-doped fiber lasers and amplifiers, 2001.

[113] Chengmin Lei, Hanlin Feng, Younès Messaddeq, and Sophie LaRochelle. Investigation of C-band pumping for extended L-band EDFAs. *J. Opt. Soc. Am. B*, 37(8):2345–2352, Aug 2020. doi: 10.1364/JOSAB.392291. URL http://josab.osa.org/abstract.cfm?URI=josab-37-8-2345.

[114] Fırat Ertaç Durak and Ahmet Altuncu. The effect of ASE reinjection configuration through FBGs on the gain and noise figure performance of L-band EDFA. *Optics Communications*, 386:31–36, 2017.

[115] CL Chang, Likarn Wang, and YJ Chiang. A dual pumped double-pass L-band EDFA with high gain and low noise. *Optics communications*, 267(1):108–112, 2006.

[116] IA Bufetov, MA Melkumov, VF Khopin, SV Firstov, AV Shubin, OI Medvedkov, AN Guryanov, and EM Dianov. Efficient Bi-doped fiber lasers and amplifiers for the spectral region 1300-1500 nm. In *Fiber Lasers VII: Technology, Systems, and Applications*, volume 7580, page 758014. International Society for Optics and Photonics, 2010.

[117] VV Dvoyrin, VM Mashinsky, and SK Turitsyn. Bismuth-doped fiber amplifier operating in the spectrally adjacent to EDFA range of 1425-1500 nm. In *Optical Fiber Communication Conference*, pages W1C–5. Optical Society of America, 2020.

[118] Simon Haykin. *Digital communications*. Wiley New York, 1988.

[119] KEITH Willox. Q factor: the wrong answer for service providers and equipment manufacturers. *IEEE Communications Magazine*, 41(2):S18–S21, 2003.

[120] AD Ellis, ME McCarthy, MAZ Al Khateeb, Mariia Sorokina, and NJ Doran. Performance limits in optical communications due to fiber nonlinearity. *Advances in Optics and Photonics*, 9(3):429–503, 2017.

[121] John G Proakis and M Salehi. Digital communications, 5th expanded ed, 2007.

[122] Max Born, Emil Wolf, A. B. Bhatia, P. C. Clemmow, D. Gabor, A. R. Stokes, A. M. Taylor, P. A. Wayman, and W. L. Wilcock. *Principles of Optics: Electromagnetic Theory of Propagation, Interference and Diffraction of Light*. Cambridge University Press, 7 edition, 1999. doi: 10.1017/CBO9781139644181.

[123] InGaAs photodiode datasheet. https://www.thorlabs.com/newgrouppage9.cfm?objectgroup_id=285. Accessed: 2022-12-20.

[124] Pavel Skvortcov, Ian Phillips, Wladek Forysiak, Toshiaki Koike-Akino, Keisuke Kojima, Kieran Parsons, and David S Millar. Nonlinearity tolerant lut-based probabilistic shaping for extended-reach single-span links. *IEEE Photonics Technology Letters*, 32 (16):967–970, 2020.

[125] Md Saifuddin Faruk and Seb J Savory. Digital signal processing for coherent transceivers employing multilevel formats. *Journal of Lightwave Technology*, 35 (5):1125–1141, 2017.

[126] Seb J Savory. Digital coherent optical receivers: Algorithms and subsystems. *IEEE Journal of selected topics in quantum electronics*, 16(5):1164–1179, 2010.

[127] Matheus Sena et al. In *2021 Optical Fiber Communications Conference and Exhibition (OFC)*, pages 1–3. IEEE, 2021.

[128] Gabriele Di Rosa et al. In *45th European Conference on Optical Communication (ECOC 2021)*, pages 1–4. IET, 2021.

[129] Robert Emmerich, Matheus Sena, Robert Elschner, Carsten Schmidt-Langhorst, Isaac Sackey, Colja Schubert, and Ronald Freund. Enabling scl-band systems with standard c-band modulator and coherent receiver using coherent system identification and nonlinear predistortion. *Journal of Lightwave Technology*, 40(5):1360–1368, 2022.

[130] Gabriele Di Rosa, Robert Emmerich, Matheus Ribeiro Sena, Johannes Karl Fischer, Colja Schubert, Ronald Freund, and Andre Richter. Characterization, monitoring, and mitigation of the i/q imbalance in standard c-band transceivers in multi-band systems. *Journal of Lightwave Technology*, 2022.

[131] Deyuan Chang, Fan Yu, Zhiyu Xiao, Nebojsa Stojanovic, Fabian N Hauske, Yi Cai, Changsong Xie, Liangchuan Li, Xiaogeng Xu, and Qianjin Xiong. Ldpc convolutional codes using layered decoding algorithm for high speed coherent optical transmission. In *OFC/NFOEC*, pages 1–3. IEEE, 2012.

[132] Benjamin J Puttnam, Ruben S Luís, Georg Rademacher, Lidia Galdino, Domaniç Lavery, Tobias A Eriksson, Yoshinari Awaji, Hideaki Furukawa, Polina Bayvel, and Naoya Wada. 0.61 pb/s s, c, and l-band transmission in a 125μm diameter 4-core fiber using a single wideband comb source. *Journal of Lightwave Technology*, 39(4): 1027–1032, 2020.

[133] Seiji Okamoto, Kengo Horikoshi, Fukutaro Hamaoka, Kyo Minoguchi, and Akira Hirano. 5-band (o, e, s, c, and l) wdm transmission with wavelength adaptive modulation format allocation. In *ECOC 2016; 42nd European Conference on Optical Communication*, pages 1–3. VDE, 2016.

[134] Jérémie Renaudier, Aymeric Arnould, Dylan Le Gac, Amirhossein Ghazisaeidi, Patrick Brindel, M Makhsiyan, Agnes Verdier, Karim Mekhazni, Fabrice Blache, Helene Debregeas, et al. 107 tb/s transmission of 103-nm bandwidth over 3$\times$ 100 km ssmf using ultra-wideband hybrid raman/soa repeaters. In *Optical Fiber Communication Conference*, pages Tu3F–2. Optical Society of America, 2019.

[135] Frédéric Maes, Manish Sharma, Lixian Wang, and Zhiping Jiang. High power bdf/edf hybrid amplifier providing 27 db gain over 90 nm in the e+ s band. In *Optical Fiber Communication Conference*, pages Th4C–8. Optica Publishing Group, 2022.

Appendix A

Rate equations for three level system

Let us first consider the three-level system and derive atomic rate equation for such a system to analyse the main physical effects underlying behind the process of amplification in such a medium. The energy level diagram is presented in Fig. A.1. The level 1 in such a system is always a ground level and has the lowest energy of all three level shown in the figure. The second level is metastable level that is characterised by the level lifetime τ which should be significantly higher than that of the level 3 which is called a pump level. The emission transition takes places in between level 2 and level 1.

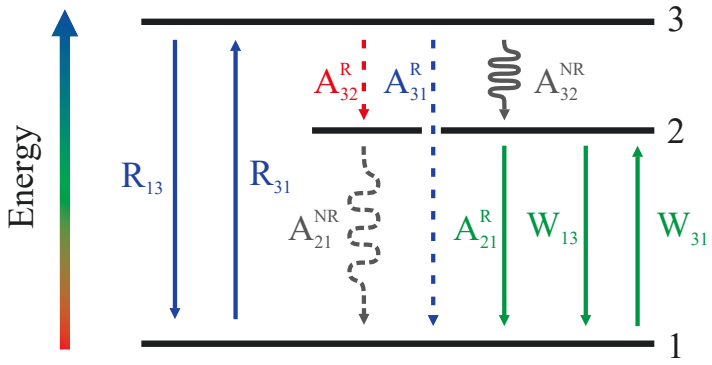

Fig. A.1 Energy level diagram of a basic three-level system, where the laser transition occurs between ground level 1 and metastable level 2. The symbols R, W, and A correspond to pumping rates, stimulated emission rates, and spontaneous decay rates between related levels; superscript R and NR referrer to radiative and nonradiative emission, respectively.

Let us now consider that the pump radiation satisfies the condition $h\nu = E_3 - E_1$ (where h is the Planck's constant, E_3 is the energy of the pump level, and E_1 is the energy of the ground level) and propagates in the three-level medium with all electrons being on the ground level. The probability of pump radiation to be absorbed in the media or to cause stimulated emission of the other photon are described by the pumping rate R_{13} and stimulated

emission rate R_{31}. Now when the pump radiation is absorbed, some of the electrons are on the pump level and there are two main possibilities to decay, i.e. radiative with rate $A_3^R = A_{32}^R + A_{31}^R$ and nonradiative with rate A_{32}^{NR}. The spontaneous decay from the level 3 is assumed to be predominantly nonradiative. After the electrons descend to the metastable level due to nonradiative transition they can further transfer to the ground level through the nonradiative (rate A_{21}^{NR}) and radiative (rate A_{21}^R) decay and stimulated emission of the excited state (rate W_{21}). On the other hand, electrons from the ground level might be transferred to the metastable level with absorption rate W_{12}. For the metastable level the spontaneous decay is essentially radiative. If we now introduce a variables $N = N_1 + N_2 + N_3$, which describe the total and population densities in the matter, we can write the atomic rate equations corresponding to these population:

$$\frac{\delta N_1}{\delta t} = -R_{13}N_1 + R_{31}N_3 - W_{12}N_1 + W_{21}N_2 + A_{21}N_2, \tag{A.1}$$

$$\frac{\delta N_2}{\delta t} = W_{12}N_1 - W_{21}N_2 - A_{21}N_2 + A_{32}N_3, \tag{A.2}$$

$$\frac{\delta N_3}{\delta t} = R_{13}N_1 - R_{31}N_3 - A_{32}N_3. \tag{A.3}$$

If we then consider a steady state regime where all the population levels are time independent, i.e. $dN_i/dt = 0$ (for i=1,2,3), and we include $a = R_{31} + A_{32}$ and $b = W_{21} + A_{21}$, we then obtain following equations from the equations (2)-(3):

$$0 = W_{12}N_1 - bN_2 + A_{32}N_3, \tag{A.4}$$

$$0 = R_{13}N_1 - aN_3. \tag{A.5}$$

If we now replace $N_3 = N - N_1 - N_2$ in the above expressions and solve for N_1 and N_2:

$$N_1 = N\frac{ab}{b(a+R_{13}) + aW_{12} + R_{13}A_{32}}, \tag{A.6}$$

$$N_2 = N\frac{R_{13}A_{32} + aW_{12}}{b(a+R_{13}) + aW_{12} + R_{13}A_{32}}, \tag{A.7}$$

If we then replace the definitions of a and b, factorise term $A_{21}A_{32}$, and assume that the nonradioative decay rate A_{32} dominates over the pumping rates R_{13}, R_{31}, eqs. (A.6)-A(A.7) yield:

$$N_1 = N\frac{1 + W_{21}\tau}{1 + R\tau + W_{12}\tau + W_{21}\tau}, \tag{A.8}$$

$$N_2 = N\frac{R\tau + W_{12}\tau}{1 + R\tau + W_{12}\tau + W_{21}\tau}, \tag{A.9}$$

where R =R_{13}. Above results show that $N_3 = N - N_1 - N_2 = 0$, thus the pump level population is negligibly small due to predominance of nonradiative decay A_{32}. The equations (8) and (9) are the central equations for calculations of the fibre gain coefficients in three-level system. Let us now write remaining equations that describe the propagation of the signal, pump,and noise beams through the fibre:

$$\frac{dP_s}{dz} = P_s\Gamma_s(\sigma_{se}N_2 - \sigma_{sa}N_1) - \alpha_s P_s, \tag{A.10}$$

$$\frac{dP_{pf}}{dz} = -P_{pf}\Gamma_p(\sigma_{pe}N_3 - \sigma_{pa}N_1) - \alpha_p P_{pf}, \tag{A.11}$$

$$\frac{dP_{pb}}{dz} = P_{pb}\Gamma_p(\sigma_{pe}N_3 - \sigma_{pa}N_1) + \alpha_p P_{pb}, \tag{A.12}$$

$$\frac{dP_{nf}}{dz} = P_{nf}\Gamma_s(\sigma_{se}N_2 - \sigma_{sa}N_1) + 2\sigma_{se}N_2\Gamma_s h\nu_s\Delta\nu - \alpha_s s_{nf}, \tag{A.13}$$

$$\frac{dP_{nb}}{dz} = -P_{nb}\Gamma_s(\sigma_{se}N_2 - \sigma_{sa}N_1) - 2\sigma_{se}N_2\Gamma_s h\nu_s\Delta\nu + \alpha_s s_{nf}, \tag{A.14}$$

where α_s and α_p are loss coefficients for signal and pump wavelength, respectively, and $\Delta\nu$ is spectral bandwidth of the noise. Here $2h\nu_s\Delta\nu$ is the contribution of spontaneous emission from the metastable level.

Appendix B

Rate equations for two level system

In many cases the lack of ions excited to the 3 energy level of 3-level system allows one to simplify three level system to two level system. Some of the doped ions are behaving as two-level systems or close to two level systems. As a first step let us consider a classical two-level system depicted in Figure B.1. The transitions R_{12} and W_{12} represent the absorption of the pump and signal, respectively. on the other hand both stimulated and spontaneous transition from the upper level can occur and are described by rates R_{21}, W_{21} and A_21. Typically spontaneous decay at the pump wavelength is negligibly low or it will be effectively reabsorbed by the neighbouring ions.

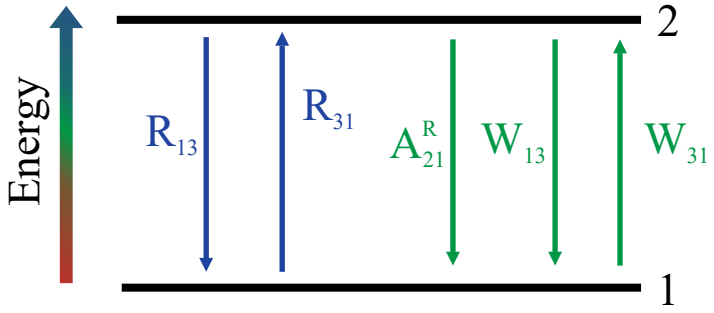

Fig. B.1 Energy level diagram of a basic three-level system, where the laser transition occurs between ground level 1 and pump level 2. The symbols R, W, and A correspond to pumping rates, stimulated emission rates, and spontaneous decay rates between related levels; superscript R and NR referrer to radiative and nonradiative emission, respectively.

As the next step the rate equations for two-level system can be written as following:

$$\frac{\delta N_1}{\delta t} = R_{21}N_2 + W_{21}N_2 - W_{12}N_1 - R_{12}N_1 + A_{21}N_2, \tag{B.1}$$

$$N_2 = N - N_1. \tag{B.2}$$

If we then consider a steady state regime where all the population levels are time independent we can achieve the following set of equations:

$$a = \frac{\sigma_{pa}\Gamma_p}{h\nu_p S_p}(P_{pf} + P_{pb}) + \frac{\sigma_{sa}\Gamma_s}{h\nu_s S_s}(P_s + P_{nf} + P_{nb}), \tag{B.3}$$

$$b = \frac{\sigma_{pe}\Gamma_p}{h\nu_p S_p}(P_{pf} + P_{pb}) + \frac{\sigma_{se}\Gamma_s}{h\nu_s S_s}(P_s + P_{nf} + P_{nb}) + A_{21}, \tag{B.4}$$

$$N_1 = \frac{bN}{a+b}, \tag{B.5}$$

$$N_2 = N - N_1. \tag{B.6}$$

where σ_{sa}, σ_{se}, σ_{pa} correspond to signal absorption cross section, signal emission cross section, and pump absorption cross section, respectively; Γ_s and Γ_p are the overlap integral between the erbium ions and the optical mode of signal and pump, respectively; ν_p and ν_s are frequency of pump and signal, respectively; S_p and S_s are the effective mode areas of the pump and the signal, respectively; P_{pf} is the power of the pump propagating forward in Watts, P_{pb} is the power of the pump propagating backward in Watts, P_s is power of the signal in Watts, P_{nb} is the power of the noise propagating backward in Watts, P_{nf} is the power of the noise propagating backward in Watts. The same set of equations should be used for calculation of the radiation propagation. as for three level system with the correct transition levels:

$$\frac{dP_s}{dz} = P_s\Gamma_s(\sigma_{se}N_2 - \sigma_{sa}N_1) - \alpha_s P_s, \tag{B.7}$$

$$\frac{dP_{pf}}{dz} = -P_{pf}\Gamma_p(\sigma_{pe}N_2 - \sigma_{pa}N_1) - \alpha_p P_{pf}, \tag{B.8}$$

$$\frac{dP_{pb}}{dz} = P_{pb}\Gamma_p(\sigma_{pe}N_2\sigma_{pa}N_1) + \alpha_p P_{pb}, \tag{B.9}$$

$$\frac{dP_{nf}}{dz} = P_{nf}\Gamma_s(\sigma_{se}N_2 - \sigma_{sa}N_1) + 2\sigma_{se}N_2\Gamma_s h\nu_s\Delta\nu - \alpha_s s_{nf}, \tag{B.10}$$

$$\frac{dP_{nb}}{dz} = -P_{nb}\Gamma_s(\sigma_{se}N_2 - \sigma_{sa}N_1) - 2\sigma_{se}N_2\Gamma_s h\nu_s\Delta\nu + \alpha_s s_{nf}, \tag{B.11}$$

where α_s and α_p are loss coefficients for signal and pump wavelength, respectively, and $\Delta\nu$ is spectral bandwidth of the noise. Here $2h\nu_s\Delta\nu$ is the contribution of spontaneous emission from the metastable level.

It is worth noting that the equation boundary-value problem for the two level system remains mathematically the same if we multiply ion concentration and lifetime by some constant and divide emission and absorption cross-sections by the same constant. To prove

this concept, first equation B.3 and equation B.4 can be represented as:

$$a_{new} = \frac{\sigma_{pa}\Gamma_p}{kh\nu_p S_p}(P_{pf} + P_{pb}) + \frac{\sigma_{sa}\Gamma_s}{kh\nu_s S_s}(P_s + P_{nf} + P_{nb}) = \frac{a}{k}, \tag{B.12}$$

$$b_{new} = \frac{\sigma_{pe}\Gamma_p}{kh\nu_p S_p}(P_{pf} + P_{pb}) + \frac{\sigma_{se}\Gamma_s}{kh\nu_s S_s}(P_s + P_{nf} + P_{nb}) + \frac{A_{21}}{k} = \frac{b}{k}, \tag{B.13}$$

where k is the constant that cross sections are divided by and lifetime and concentration are multiplied by. It should be reminded that $A_{21} = 1/\tau_{21}$. As the next step the values of a_new and b_new should be used for calculation of N_1 and N_2:

$$N_{1new} = \frac{kNb/k}{a/k + b/k} = kN_1, \tag{B.14}$$

$$N_{2new} = kN - kN_1 = kN_2. \tag{B.15}$$

Finally obtained values can be used to show that the equations B.7-B.11 has the same solution. The equation B.7 is show as an example, however, all other equations have the similar behaviour:

$$\frac{dP_s}{dz} = P_s\Gamma_s(kN_2\sigma_{se}/k - kN_1\sigma_{sa}/k) - \alpha_s P_s = P_s\Gamma_s(N_2\sigma_{se} - N_1\sigma_{sa}) - \alpha_s P_s. \tag{B.16}$$

Appendix C

Rate equations for four level system

Let us now consider a four-level system which energy-level diagram is presented in Figure C.1. The energy system consists of ground level 1 with the lowest energy, pump level 4 has the highest energy and it usually features short level lifetime provided by fast nonradiative decay from level 4 to level 3. Level 3 in four-level system is a metastable level with long level lifetime. Laser transitions can occur between metastable level and both lower levels 2 and 1. However, in most cases the transition between levels 3 and 1 are undesirable i.e. for Nd-doped fibre (see Subsection 2.4.3). Level two is a typical lower level to achieve efficient laser transition due to small lifetime of such a level provided by a short lifetime and a fast nonradiative decay to the ground level.

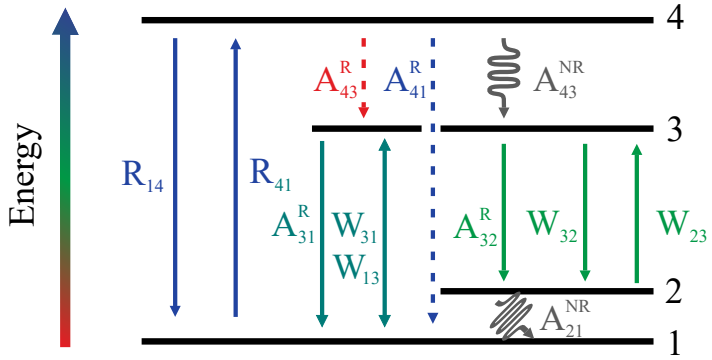

Fig. C.1 Energy level diagram of a basic four-level system, where the laser transition occurs between level 2 and metastable level 3. The symbols R, W, and A correspond to pumping rates, stimulated emission rates, and spontaneous decay rates between related levels; superscript R and NR referrer to radiative and nonradiative emission, respectively.

As the next step the general rate equations for population densities of a four-level system can be written as following:

$$\frac{\delta N_1}{\delta t} = -R_{14}N_1 + R_{41}N_4 + W_{31}N_3 - W_{13}N_1 + A_{31}N_3 + A_{21}^{NR}N_2, \tag{C.1}$$

$$\frac{\delta N_2}{\delta t} = W_{32}N_3 - W_{23}N_2 - A_{21}^{NR}N_2 + A_{32}^{R}N_3, \tag{C.2}$$

$$\frac{\delta N_3}{\delta t} = W_{13}N_1 - W_{31}N_3 - A_{31}^{R}N_3 - A_{32}^{R}N_3 - W_{32}N_3 + W_{23}N_2 + A_{43}N_4. \tag{C.3}$$

$$\frac{\delta N_4}{\delta t} = R_{14}N_1 - R_{41}N_4 - A_{41}^{R}N_4 - A_{43}N_4. \tag{C.4}$$

Here the symbols R, W, and A correspond to pumping rates, stimulated emission rates, and spontaneous decay rates between related levels; superscript R and NR referrer to radiative and nonradiative emission, respectively. The equations (C.1-C.4) can be simplified similarly to two-level or three-level system, however, the necessary terms highly depend on the active media and host material that is used for propagation. Thus, these simplifications are not presented here. The equations for signal, pump and noise propagation in case of suppressed transitions between levels 31 yield:

$$\frac{dP_s}{dz} = P_s\Gamma_s(\sigma_{se}N_3 - \sigma_{sa}N_2) - \alpha_s P_s, \tag{C.5}$$

$$\frac{dP_{pf}}{dz} = -P_{pf}\Gamma_p(\sigma_{pe}N_4 - \sigma_{pa}N_1) - \alpha_p P_{pf}, \tag{C.6}$$

$$\frac{dP_{pb}}{dz} = P_{pb}\Gamma_p(\sigma_{pe}N_4\sigma_{pa}N_1) + \alpha_p P_{pb}, \tag{C.7}$$

$$\frac{dP_{nf}}{dz} = P_{nf}\Gamma_s(\sigma_{se}N_3 - \sigma_{sa}N_2) + 2\sigma_{se}N_3\Gamma_s h\nu_s\Delta\nu - \alpha_s s_{nf}, \tag{C.8}$$

$$\frac{dP_{nb}}{dz} = -P_{nb}\Gamma_s(\sigma_{se}N_3 - \sigma_{sa}N_2) - 2\sigma_{se}N_3\Gamma_s h\nu_s\Delta\nu + \alpha_s s_{nf}, \tag{C.9}$$

These equations can be solved in the same manners as equations for two-level and three-level systems along with the equations for population densities. This procedure is described in the next Appendix D.

Appendix D

Numerical methods for solving Boundary value problems

In this section numerical methods that are used to solve boundary value problems of radiation propagation in active fibre is considered. These equations are ODEs, and the most convenient and accurate method to solve ODE is 4^{th} order Rhunge-Kutta method. As a first step, the segment of the fibre with length L should be spatially divided into n segments, yielding longitudinal step $h = L/n$. Then the boundary conditions should be appropriately chosen as presented in the Table D.1.

Table D.1 Initial and Boundary Conditions

Initial and Boundary Condition	Explanation
$P_s(0) = P_s$	Initial condition for signal power [W]
$P_{pf}(0) = P_{pf}$	Initial condition for forward pump power [W]
$P_{pb}(L) = P_{pb}$	Boundary condition for backward pump [W]
$P_{nf}(0) = P_{nf}$	Initial condition for forward ASE noise [W]
$P_{nb}(L) = P_{nb}$	Boundary condition for backward ASE noise [W]

The algorithm that advances $P_i(z)$ to $P_i(z+h)$ in a spatial step h, where P_i is any of the signal, pump or noise powers (with i corresponding to the abbreviations "s" for signal, "nf" for noise forward, "nb" for noise backward, "pf" for pump forward, "pb" for pump backward) can be presented as following:

$$k_{1i}(z+h) = hP_i(P_s(z), P_{pf}(z), P_{pb}(z), P_{nf}(z), P_{nb}(z)), \tag{D.1}$$

$$k_{2i}(z+h) = hP_i(P_s(z) + \frac{k_{1s}}{2}, P_{pf}(z) + \frac{k_{1pf}}{2}, P_{pb}(z) + \frac{k_{1pb}}{2}, P_{nf}(z) + \frac{k_{1nf}}{2}, P_{nb}(z) + \frac{k_{1nb}}{2}), \tag{D.2}$$

$$k_{3i}(z+h) = hP_i(P_s(z)+\frac{k_{2s}}{2}, P_{pf}(z)+\frac{k_{2pf}}{2}, P_{pb}(z)+\frac{k_{2pb}}{2}, P_{nf}(z)+\frac{k_{2nf}}{2}, P_{nb}(z)+\frac{k_{2nb}}{2}), \tag{D.3}$$

$$k_4(z+h) = hP(P_s(z)+k_{3s}, P_{pf}(z)+k_{3pf}, P_{pb}(z)+k_{3pb}, P_{nf}(z)+k_{3nf}, P_{nb}(z)+k_{3nb}), \tag{D.4}$$

$$P_i(z+h) = P_i(z)+\frac{k_{1i}}{6}+\frac{k_{2i}}{3}+\frac{k_{3i}}{3}+\frac{k_{4i}}{6}. \tag{D.5}$$

Following equations should be consistently solved for each of signal, pumps and noise propagating in both forward and backward and fibre step along with equations for appropriate level populations (depending on the number of energy levels of the active centres) which also should be solved for every segment of the fibre. However, as the equations should be solved to agree not only with initial but boundary conditions, another numerical technique should used. There are two main methods to solve boundary-value problem: the shooting method and relaxation method. The relaxation method is a trial and error approach, where the unknown boundary is first guessed. At first the interval for the initial guess is determined, and the guess is corrected in each iteration until the desired convergence is obtained. Using the initial guess, the final power based on the guess at $z = L$ is obtained by numerical solution, with P_{num} and the desired power from boundary conditions with P_{goal}. The iteration should be continued until the desired convergence is obtained. In the shooting method, the initial guess is given a certain value, which is based on two or three random guesses. On the other hand, the relaxation method makes iterative adjustment to the solution. In this method, an initial set of boundary value is chosen for the first integration. Then, the system is integrated again, for instance in the reverse direction, using correct boundary values. The relaxation method offers many possibilities for solving the rate equations.

Here the relaxation method was chosen because of versatility and high accuracy. As a first step, the set of equations is simplified to be solve only for the function with determined initial conditions: signal power, forward pump power, and forward noise power. After these equations are consistently solved for each fibre segment, and the solution at the end of the fibre are known,the equations for bi-directional signal, pump and noise propagation can be solved in reverse direction using calculated values of the signal power, the forward pump power, the forward ASE power at the end of the fibre, and boundary conditions of the backward pump power and the backward ASE noise as initial conditions for reverse equations. To write down the reverse equations the right-hand side of each equation should be multiplied by minus one. By doing such a calculation the initial conditions for the backward pump power, the backward ASE noise can be found and, thus, the forward calculation of all 5 equations can be processed.

In order to improve the accuracy, the set of equations is then solved back and forth (i.e from $z = 0$ to $z = L$, and then from $z = L$ to $z = 0$) using the quasi-solution for unknown

initial or boundary conditions. With this algorithm, convergence towards the actual solutions can be achieved, due to a particular property of the rate equations involved. Using this quasi-solutions as a boundary condition for the next iteration from z = 0 to z = L yields a more accurate solution for all functions. Each roundtrip refines the mutual saturation effect and increases the accuracy of the solutions. The iterations of this back and forth routine is halted when the difference between the successive solutions is less than 10^{-7}.